Use Authorization

In presenting this thesis in partial fulfillment of the requirements for an advanced degree at Idaho State University, I agree that the Library shall make it freely available for inspection. I further state that permission to download and/or print my thesis for scholarly purposes may be granted by the Dean of the Graduate School, Dean of my academic division, or by the University Librarian. It is understood that any copying or publication of this thesis for financial gain shall not be allowed without my written permission.

Signature _____

Date _____

EBSD Determined Grain and Grain Boundary Characteristic Correlation with Deposition and Annealing Temperatures of the CVD coated SiC Layer of TRISO Particle Nuclear Fuel

by

Connie Mae Siepker Hill, B.S

A thesis

submitted in partial fulfillment

of the requirements for the degree of

Master of Science in Nuclear Science and Engineering

Idaho State University

August 2014

COMMITTEE APPROVAL

To the Graduate Faculty:

The members of the committee appointed to examine the thesis of CONNIE MAE SIEPKER find it satisfactory and recommend that it be accepted.

_____

Dr. Mary Lou Dunzik-Gougar,

Major Advisor

_____

Dr. Isabella van Rooyen,

Committee Member

_____

Dr. Chad Pope,

Committee Member

_____

Dr. Lisa Goss,

Graduate Faculty Representative

ACKNOWLEDGEMENTS

To all those who have worked to build up the nuclear engineering program at ISU, I give a special thanks. I feel that I have had a rich educational experience. I have learned something valuable from each and every one of the faculty and staff. My academic advisor, Dr. Mary Lou Dunzik-Gougar, was instrumental in opening the doors for my post graduate studies. Without her support, I would have missed out on an incredible opportunity for advanced studies. My mentor, Dr. Isabella van Rooyen, through her hard work and career pursuits opened the door of opportunity to work on a most fascinating nuclear application for which I am most grateful. I am grateful to Dr. Eugene Stuffle, Dr. Jay Kunze, Dr. George Imel, Todd Gansauge, M.S., Warren Gossett, and the late Dr. Michael Lineberry who also took time out of their busy schedules to write letters of recommendation for scholarships. The NRC, ANS, and INPO helped finance my educational journey which is most appreciated. Dr. Lineberry left before I had a chance to properly thank him for going out of his way to encourage me. Dr. Chad Pope has picked up where he left off in more ways than he might know. I appreciate his valuable advice and support as well. A special thanks to all who worked to provide the samples for analysis from the NECSA and NMMU.

My husband, Brett Hill, has taken over several home responsibilities on top of working a full time job to free up my time for focused studies. His support allowed me to succeed in accomplishing some difficult tasks. My children; Jason, Jacob, Jarod, Christi, Ed, Natasha, Bethanie, and Cadence will forever serve as motivation to keep going. My parents, David and Caryl Siepker, as well as my sisters, Donna, Diane, and Cathy have also been supportive. I feel richly blessed. Thank you all so very much!

CONTENTS

FIGURES

TABLES

ACRONYMS

CI	Confidence Index
CSL	Coincidence Site Lattice
CVD	Chemical Vapor Deposition
DOE	Department of Energy
EBSD	Electron Backscatter Diffraction
EBSPs	Electron Backscatter Patterns
FBCVD	Fluidized Bed Chemical Vapor Deposition
FCC	Face Centered Cubic
FEI	Field Emission Inc.
FIB	Focused Ion Beam
GBCD	Grain Boundary Character Distribution
INL	Idaho Nation Laboratories
IPF	Inverse Pole Figure
IPyC	Inner Pyrolytic Carbon
IQ	Image Quality
ISU	Idaho State University
LMIS	Liquid Metal Ion Source
MEMS	Microelectrical Mechanical Systems
NECSA	Nuclear Energy Corporation of South Africa
NGNP	Next Generation Nuclear Plant
NMMU	Nelson Mandela Metropolitan University
OIM	Orientation Imaging Microscopy
OpyC	Outer Pyrolytic Carbon
PBMR	Pebble Bed Modular Reactor
PF	Pole Figure
SEM	Scanning Electron Microscope
SIM	Scanning Ion Microscope
TRISO	Tri-ISOstructural
VTGR	Very High Temperature Gas-cooled Reactor

ABSTRACT

The SiC layer of TRISO particle fuel serves as the primary fission product containment barrier for the high temperature gas cooled reactor. Electron Backscatter Diffraction (EBSD) analysis for 3C- and 6H-SiC phases is performed on samples fabricated at different deposition temperatures, 1410˚C (Batch D) and 1510˚C (Batch E), and annealed at 2000˚C for 30 minutes.

The EBSD analysis showed fairly similar grain boundary character distributions (GBCDs) for non-annealed samples. Results from annealed samples; however, show potential different high temperature behavior with an increase in high angle grain boundary number fraction in batch E (0.1965 to 0.3002) and a decrease in batch D (0.2028 to 0.1245) after annealing, the decrease being favorable regarding fission product migration. No indication of increase in the less desirable hexagonal phase upon annealing was found. Also, a new, state-of-the-art, in situ sample extraction/preparation method utilizing the FEI Quanta 3D FIB/SEM dual beam system is demonstrated.

1. Introduction

1. A The Challenge

The High Temperature Gas-cooled Reactor (HTGR), designed to produce electricity, provide industrial heat, and/or facilitate hydrogen production, was chosen by the U.S. Department of Energy (DOE) for the Next Generation Nuclear Plant (NGNP) project. (Petti, 2010) The proposed design requires specially designed materials to withstand high operating temperatures as well as potential accident conditions. Most importantly, the fuel and fission products must be contained. The fuel is a Tri-ISOstructural (TRISO) coated particle, in which a small spherical fuel kernel is coated with a light buffer layer of pyrolytic carbon, a more dense inner pyrolytic carbon (IPyC) layer, a silicon carbide (SiC) layer, and finally an outer pyrolytic carbon (OPyC) layer. Figure 1.(a) shows a cross section of the TRISO particle and Figure 1.(b) shows the cross section of an irradiated TRISO particle.

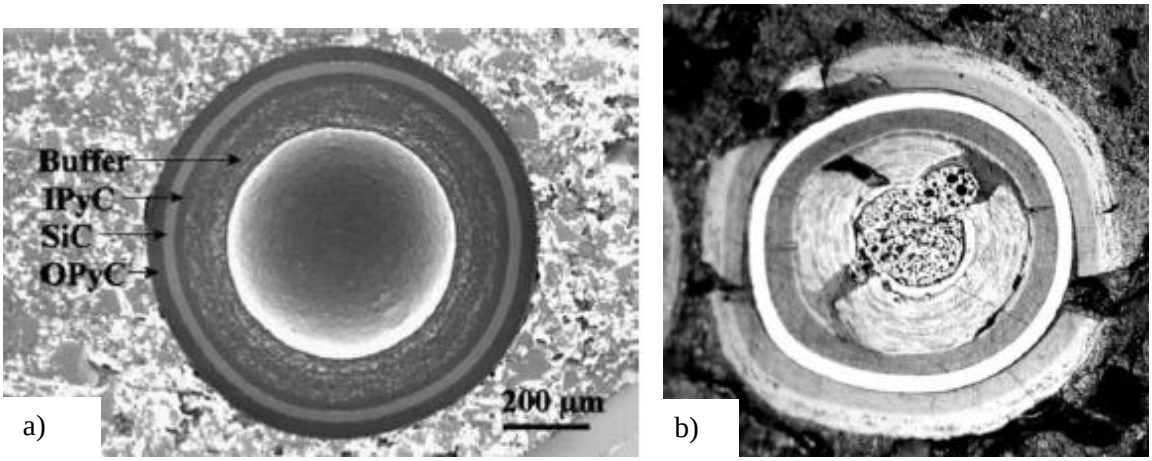

Figure 1. a) TRISO coated particle cross section (Lopez-Honorato, 2009), and b) irradiated TRISO coated fuel particle. (Snead, 2007)

Note the structural damage of the OPyC layer as opposed to the intact white SiC layer after irradiation. The SiC layer serves as the essential structural pressure vessel, as well as the main barrier to fission product migration. Optimal fuel performance hinges on the successful performance of this layer. Minimization of pressure vessel failure, fission product transport, irradiation degradation, and thermal decomposition become the challenge for nuclear materials scientists. (van Rooyen, 2012)

Macroscopic properties such as strength, ductility, toughness, corrosion resistance, thermal conductivity, etc., are inherently dependent on the texture, or microstructure of the material. (Watanabe, 2011) The texture of natural or manufactured materials can, to a significant extent, be enhanced to achieve a desired quality by controlling manufacturing process parameters, and/or subjecting the material to thermo-mechanical treatments. The underlying mechanisms for texture transformations are not fully understood; therefore, it is common practice in materials engineering to evaluate changes in texture given the corresponding process conditions, and then to proceed with desired, empirically validated fabrication processes. (Fuchs, 1990), (Randle, 2000)

Microstructure analysis requires the identification of grain and grain boundary characteristics of a material, and the interpretation of their significance in relation to desired material properties. A grain is the collection of uniformly aligned individual crystal cells within a specimen. Grain boundaries consist of border atoms between grains with differing crystalline structures or grains with differing orientations relative to the orientation of the volumetric specimen. Most materials do not have a random distribution of crystallographic orientations. Because many material properties depend on the

direction in which they are measured, it is important to determine and understand the preferred crystalline orientation of the material. (Fuchs, 1990), (Randle, 2000)

Many other characteristics of grains and grain boundaries are directly related to important properties of the material. For example, it has been determined that the β-SiC poly-type is most resistant to irradiation damage. (Snead, 2007) It would then be beneficial to identify process conditions that favor the production of this single poly-type. Furthermore, the phenomenon of silver, Ag-110m, transport through the SiC layer, that has been perplexing research scientists for decades (van Rooyen 2012), has been shown in recent studies to be strongly influenced by grain boundary diffusion. Lopez-Honorato et al. (2011) have concluded it is of utmost importance to characterize the grain boundary distribution in SiC of different deposition conditions, and study the possibility of improving grain boundary characteristics that reduce fission product diffusion, such as the minimization of high angle random boundaries. Other researchers have called for more data in this matter for statistical verification of previous findings. (Snead, 2007) Data obtained through microstructure analysis of SiC layers fabricated under various process methods will be a significant addition to the body of work of fuel optimization research.

1.1 Objective of Thesis Work

Currently a study is being conducted by research partners, Idaho State University (ISU) and Nelson Mandela Metropolitan University (NMMU), on chemical vapor deposition (CVD) grown SiC layers of TRISO surrogate fuel particles pulled from batches produced in 2007 by PBMR Fuel Development Laboratories at the Nuclear Energy Corporation of South Africa (NECSA). These batches were chosen for their various deposition temperatures and for the variety of possible annealing process conditions to which the particles were subjected. Table 1 lists particle fabrication parameters per batch for the overall study. The principle investigators in this project include Dr. van Rooyen, INL Materials Research Scientist, and Dr. Mary Lou Dunzik-Gougar, Associate Chair of Nuclear Engineering at Idaho State University and INL Research Scientist. Highly accomplished Professors Japie Engelbrecht, and Jan Neethling from NMMU serve as collaborators.

Table 1. Overall study sample set of TRISO fuel particles for analysis with corresponding SiC layer production parameters, and sample responsibility breakdown between NMMU and ISU. (van Rooyen)

		Post-production annealing conditions											
Batch	Conditions	Reference (no annealing	1000 ˚C 1 h	1300 ˚C 1 h	1500 ˚C 1 h	1600 ˚C 1 h	1700 ˚C 1 h	1600 ˚C 100 h	1800˚ C 1 h	1900 ˚C 1 h	1980 ˚C 1 h	2000 ˚C 30 min.	2100 ˚C 10 min.
A	ACF[1] 1510 ˚C	NMMU	NMMU	NMMU	NMMU	NMMU	NMMU	NMMU	NMMU	NMMU	NMMU	NMMU	NMMU
B	RCF[2] 1510 ˚C	NMMU	NMMU			ISU Complete		ISU Complete	ISU			ISU	ISU
C	RCF[2] 1585 ˚C	NMMU	NMMU			ISU		ISU	ISU			ISU	ISU
D	ACF[1] 1450 ˚C	ISU Complete				ISU		ISU	ISU			ISU Complete	
E	ACF[1] 1510 ˚C	ISU Complete				ISU Complete		ISU	ISU			ISU Complete	

1. Advanced Coating Facility at the South African Nuclear Energy Corportation (NECSA), 5 kg capacity, SiC deposition rate 0.23-0.24 µm/min
2. Research Coating Facility at NECSA, 1 kg capacity, SiC deposition rate 0.17 µm/min

The objective of this thesis work is to demonstrate the application of a new, state-of-the-art sample extraction technique used for specialized electron backscatter diffraction (EBSD) surface analysis, and to characterize the microstructure of a subset of these particles to the fullest extent possible using EBSD. Once characterization has been completed, the final objective is to then identify any links between microstructure and corresponding process conditions. Identification of any relationships between grain and grain boundary characteristics with prior strength or hardness test results will also be sought. EBSD analysis will be done on small samples extracted by focused ion beam (FIB) milling from the SiC layer of various particles. This analysis will identify several grain and grain boundary characteristics, which will illuminate the process specified SiC layer microstructure. Grain and grain boundary characteristics to be identified include the following:

- grain size distribution
- average grain size
- grain orientation topography (grain mapping)
- grain boundary topography (boundary mapping)
- grain orientation density (pole figures)
- grain misorientation angle distribution
- boundary rotational angle distribution
- coincidence site lattice boundary distribution
- lattice structure (cubic vs. hexagonal)

These data will serve to inform the material engineering process in order to achieve optimum fuel performance and will be incorporated into the full body of data for the overall project.

1.3 Work Performed

Due to time and budget constraints for sample analysis, the body of this work will comprise analysis, as described in section 1.2, of only four samples. These include one sample extraction each from particles of Batches D and E, both non-annealed, and annealed at 2000˚C for 30 minutes. Both batches were prepared with the same coater at different deposition temperatures and at the same deposition rate. Each sample will herein be referred to as the batch designation coupled with the annealing temperature. For example, D-ref would represent a sample taken from a particle belonging to Batch D with no annealing treatment. E2000 would indicate a sample taken from a particle belonging to Batch E with annealing at 2000˚C.

A new FIB/SEM sample extraction and polishing technique was attempted on B1600 in order to compare with prior results from EBSD analysis on a B-ref sample. The B1600 sample did not successfully generate a clear signal for EBSD analysis, so a change in the original plan was made to rescan D-ref, D2000, E-ref, and E2000 previously prepared samples for a hexagonal phase that might appear in the deposition or annealing processes. EBSD analysis was conducted for the 6H-SiC polytype on all of the samples listed above with the exception of E2000. E2000 was apparently lost due to breakage of the sample platform. Failure of the B1600 sample to generate a quality EBSD signal is not necessarily due to failure of the sample extraction and polishing method, and may be more likely due to the immitigable nature of the material itself. The sample extraction method is outlined for future reference.

2. Literature Review

2.A History and Development of TRISO Particle Nuclear Fuel

2.A.1 An Historical Overview

The desire to generate electricity via nuclear energy with a fail-safe design to protect the public and the environment from potential accidental fission product release ruminated in the minds of nuclear scientists long before the well-known Chernobyl or Fukushima incidents. Professor Rudolf Schulten, a German physicist, is credited with the idea to imbed tiny particles of uranium into graphite spheres the size of a tennis ball. This was to insure the fuel would not melt. Thousands of these spheres were to be placed in a reactor and cooled by helium gas, which was in turn to be used to power turbines for electricity generation. This idea brought life to a pebble bed modular reactor (PBMR) prototype, the Arbietsgemeinshaft Versuch Reaktor (AVR) built in Jülich Germany in 1967 that ran for 21 years. (Schmidt, 2006), (Nicholls, D. R., 2002)

Meanwhile, the British launched their model of a helium gas cooled, graphite moderated 20-MWth reactor called the Dragon. It was the first to use graphite coated fuel particles. The United States took the idea from there, and built a 40-MWe HTGR at Peach Bottom, Pennsylvania which ran from 1967-1974. Fort St. Vrain, Colorado produced a commercially viable 330-MWe reactor in 1979, and closed it in 1989. All three of these reactors were fueled by coated particles pressed into prismatic graphite blocks. Problems were encountered in the process of scaling up to larger power output, and lack of political will to invest in nuclear technologies after the Chernobyl incident led to dormancy of the concept in the United States. (Nicholls, D. R., 2002)

As Germany's nuclear ambitions began to fade, South Africa kept the pebble bed reactor concept alive. In 1993, the largest utility in South Africa, Eskom, bought the rights to the pebble bed design. In 1999 PBMR Ltd. was created and backed by foreign investors to demonstrate the economic and technical feasibility of the concept. (Schmidt, 2006) South Africa built a commercial sized unit and took the lead in the field in PBMR technology. (Nicholls, 2002)

Recently, the Generation IV International Forum has chosen the very high temperature gas-cooled reactor (VTGR) for further research and development as a potential candidate for a future reactor design to provide the best in safe and economical electric power generation. VTGR fuel design is based on the PBMR TRISO coated particle technology. (Sedov, 2011) Research and development has been, and will be carried out on current TRISO fuel particle technologies within the United States. (Petti, 2010), (Kirchhofer, 2013)

2.A.2 The TRISO Particle

The TRISO particle consists of specially prepared kernels of nuclear fuel coated with several layers of pyrolytic carbon, and a layer of SiC in a fluidized bed chemical vapor deposition (FBCVD) coater. This coating process is simply referred to as CVD throughout the literature. The first layer of pyrolytic carbon is the buffer layer. It is approximately 90-100 μm thick, and approximately 50% void. This porous layer was developed to accommodate: swelling of the nuclear fuel kernel, space for gases such as xenon and krypton which emerge as fission products during operation, and absorption of fission product recoil during operation. The second layer of pyrolytic carbon, IPyC, is a

higher density layer, ~35-40μm thick, and serves as: an initial pressure barrier, a structural foundation for deposition of the SiC layer, and a preventative measure regarding chlorine chemical attack on the fuel kernel during deposition of the SiC layer. The SiC layer, ~35μm thick, serves as the main pressure containment vessel, and fission product diffusion barrier. The final layer, OpyC, ~35-40μm thick, serves as protective layer for the SiC layer from further processing and irradiation damage. (Nicholls, 2002), (Snead, 2007), (Kirchhoffer, 2013), (LeFevre, 1977) See Figure 1. (a) for a cross sectioned view of the fabricated particle.

2.A.3 Properties and functions of SiC

Over 200 polytypes of SiC have been identified by distinct Laue patterns formed by x-ray diffraction. The fundamental unit of SiC is the bilayer of connected silicon and carbon atoms as illustrated in Figure 2. Polytypes are formed by various stacking sequences of the SiC bilayer. Stacking can be visualized as starting in the (0001)-plane as depicted in Figure 2. Consecutive bilayers stacked in the c-axis direction may be shifted to the right or left as viewed from the side. Depending upon the sequence, various crystalline structures of SiC are formed. The most common crystalline structures include one cubic, designated β-SiC, and several hexagonal and rhombohedral structures all designated α-SiC.

A polytype is designated by the number of times the bilayers shift in a stacking sequence before repeating the pattern, and by the first letter of the resulting crystalline structure. For example, 3C-SiC would be the polytype consisting of three shifts of the SiC bilayer before the pattern repeats, resulting in a cubic structure. 6H-SiC would be the

polytype consisting of six shifts of the SiC bilayer before the pattern repeats, resulting in a hexagonal crystalline structure. (Pensl, 2005), (Snead, 2007)

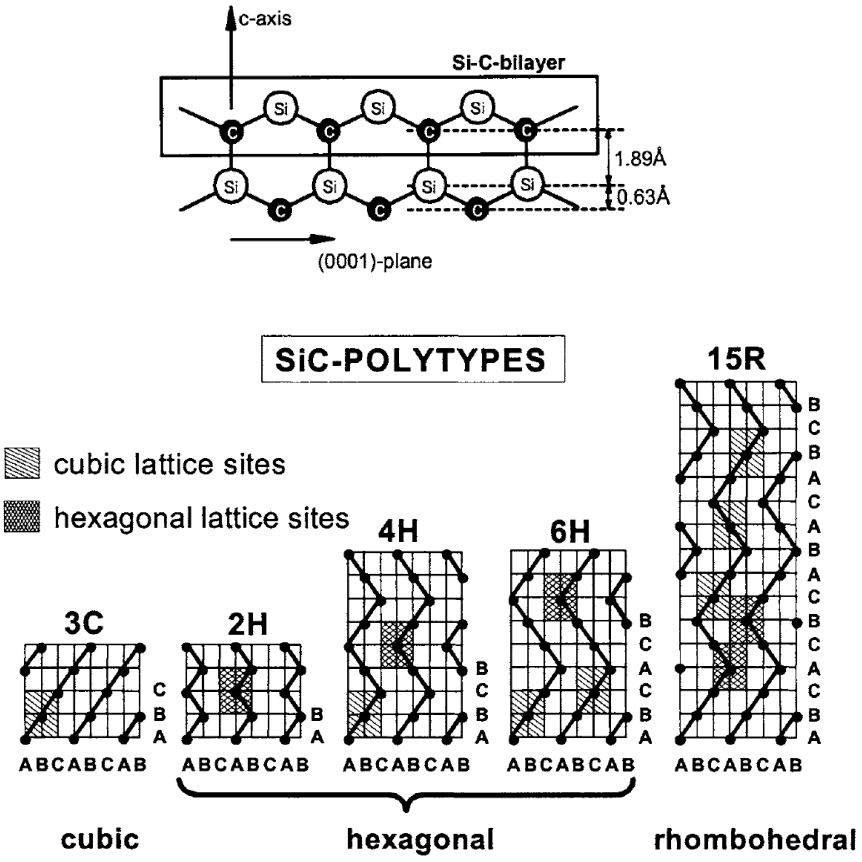

Figure 2. Top: SiC bilayer, the basic component for the formation of polytypes. Bottom: Illustration of stacking patterns for a few common SiC polytypes. (Adapted from Pensl, 2005)

SiC is a synthesized ceramic fabricated by a variety of methods such as: sintering, direct conversion, gas phase reaction, or polymer pyrolysis. The most stable and desirable polytype because of its cubic structure, 3C-SiC, also known as β-SiC, has been most successfully fabricated with a 1:1 silicon to carbon stoichiometric ratio by a gas phase reaction method known as chemical vapor deposition (CVD). (Snead, 2007) 3C-SiC is known to be face centered cubic (FCC). (Tan, 2008) The carbon atom is connected to four silicon atoms in a tetrahedron, and vice versa. The resulting chemical structure is

more specifically two FCC structures, one of carbon, one of silicon rotated one quarter the diagonal length of a cubic cell with respect to each other forming a structure known as zinc blende. (van Rooyen, 2011)

SiC is endowed with exceptional material properties that make it a well sought out material for a variety of applications including; the use in high performance electronic and optical devices, biomedical devices, space exploration and defense systems, and in nuclear fuel fission product containment. Table 2 lists the general properties of CVD grown β-SiC.

Table 2. General Properties of Transparent Chemical Vapor Deposited SiC. (Adapted from Goela, 1994)

Property	Typical Value
Color	Yellow
Phase	Beta (cubic)
Crystal Structure	FCC polycrystalline highly oriented <111>
Average Grain Size	5-10
Transmittance, 0.6-5.6 µm (0.5 mm thick)	>40%
Attenuation Coefficient (cm^{-1})	6.9
at 0.6328 µm	
at 3 µm	2.2
Density (g/cm^3)	3.21
Vickers Hardness (1-kg load)	2700
Fracture Toughness, K_{ic} ($MN\ m^{-1.5}$)	2.2
Trace Element Impurities (ppmw)	3.2
Coefficient of Thermal Expansion ($10^{-5}\ K^{-1}$) at 293 K	2.2
Thermal Conductivity (W m-1 K-1) at 27˚C	214
Electrical Resistivity (Ω cm)	4.5×10^4
n or p type	n type
Dielectric Constant (35-50 GHz)	136
Dielectric Loss (35-50 GHz)	75
Elastic Modulus, GPa	4.66

Researchers report a high chemical stability in hostile environments, high thermal conductivity, high mechanical strength, high resistance to oxidation, and high resistance to radiation and thermal degradation. (Sahu, 2012), (Goela, 1994), (van Rooyen, 2011)

2 .A.4 Fluidized Bed Chemical Vapor Deposition (FBCVD)

The coating of particle fuels is a sophisticated process carried out in a high temperature furnace in the presence of the thermal decomposition of a gas containing the coating material. All four outer layers of the TRISO particle are usually formed by chemical vapor deposition. The fuel particles are fluidized by a flow gas such as H_2 containing measured portions of a hydrocarbon gas for the deposition of pyrolyzed carbon forming the buffer, IPyC, and OPyC layers. The gas injected through a nozzle forms a circulation pattern for both gas and particles within a bed of contained particles. A diagram of the general process is depicted in Figure 3.

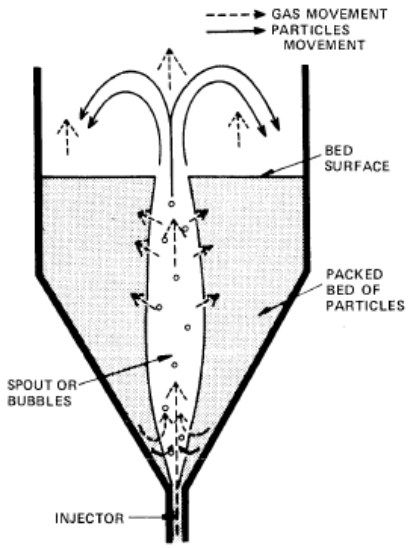

Figure 3. Simplified geometry of a spouted fluidized bed coater.
(Lefevre and Price, 1977)

The colliding particles develop small cracks that become nucleation sites. The pyrolyzed carbon nuclei collide, combine and grow, and eventually bind to the particle nucleation sites. Similarly, the SiC layer is formed by the thermal decomposition of methyltrichlorosilane (CH_3SiCl_3) vapor carried into the furnace by the flow gas H_2. The chemical reaction:

$$CH_3SiCl_3 \rightarrow SiC + 3HCl \qquad (1)$$

provides the coating material. The method has a tendency to result in layers containing grains that increase in size in the radial direction. An inert diluent gas may be introduced to enhance the process. (Lefevre, 1977) Studies have shown that the introduction of argon gas into the flow gas does indeed work to both reduce the grain size, and provide a more uniform consistency across the thickness of the deposited layer. (Lopez-Honorato, 2009), (Kirchhofer, 2013) A multiple spout method has also been tried with favorable results toward achieving a more uniform grain size along the SiC layer radial direction. (Lopez-Honorato, 2009) Optimum temperatures for coating have been empirically determined in order to produce a stoichiometric SiC without excess Si, as well as smaller grain sizes, and the desired β-SiC poly-type. (Lefevre, 1977)

2.B. EBSD Analysis

2.B.1 The Fundamentals

It has been common practice in the investigation of crystalline materials to focus a beam of particles, usually electrons or neutrons, or a beam of x-rays onto a specimen and observe the resulting diffraction pattern. The use of electron beams in microstructure analysis is favorable due to the achievable short monochromatic wavelength, the ability to raster the charged beam if necessary, and more importantly, the lower depth of penetration into the specimen which allows for evaluation of single top layer grains. (Randle, 2000)

Bragg's law is fundamental in the evaluation of crystallographic planes within a grain, and their orientation with respect to the specimen. Figure 4 illustrates the phenomenon. Electrons are initially diffusely scattered when entering a crystalline solid. Some of these scattered electrons will arrive at crystalline planes at the Bragg angle, backscatter, and constructively interfere to form what can be observed as maxima termed Kikuchi lines. The diffracted wave three dimensionally forms a wide mouth conical surface with axis normal to the interacting plane. All interactions considered, the source of the diffracting wave can be taken to be in the center of two adjacent planes, cones forming on both sides of the source. These cones are designated Kossel cones. A Phosphor screen is used in automated EBSD equipment to capture the pattern created by the intersection of the Kossel-cones with the plane of the screen. Kikuchi lines emerge on the screen forming bands the width of 2θ. Figure 5 illustrates this concept by a directional diagram along with a sample Kikuchi pattern obtained in EBSD analysis. Note how

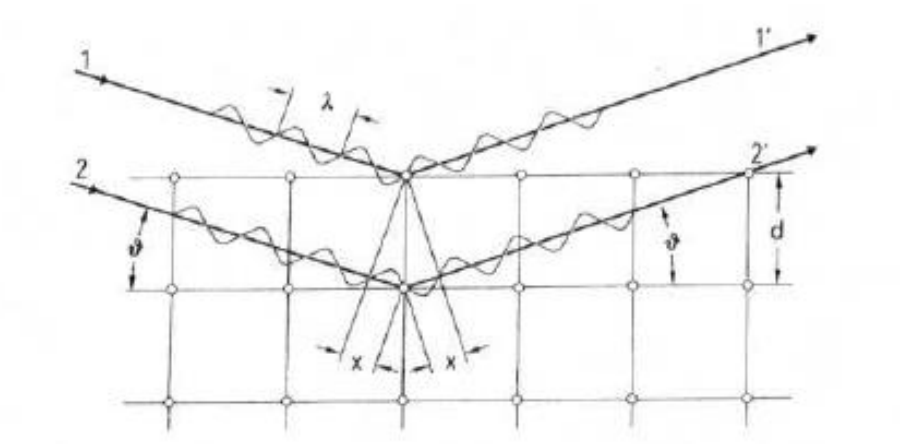

Figure 4. Diffraction at the crystalline lattice: the two incident waves 1 and 2 are initially in phase. After scattering at the atoms of the lattice, the waves 1' and 2'are of equal phase and lead to an intensity maximum only when the path difference 2 x between them is equal to, or an integral multiple n of the wavelength λ. From this follows, with $x = d\sin\theta$, $n\lambda = 2d\sin\theta$, known as Bragg's law. (Fuchs, 1990)

several of these bands intersect in some instances creating a star-like pattern. These intersections indicate low index zone axes of the crystal. The Kikuchi band pattern gives all the information necessary to determine the crystalline structure, phase, and orientation with respect to the sample axes. The topography, as well as grain boundary information of a polycrystalline material can also be determined by collecting electron backscattered diffraction patterns (EBSPs) in spatially specific increments.

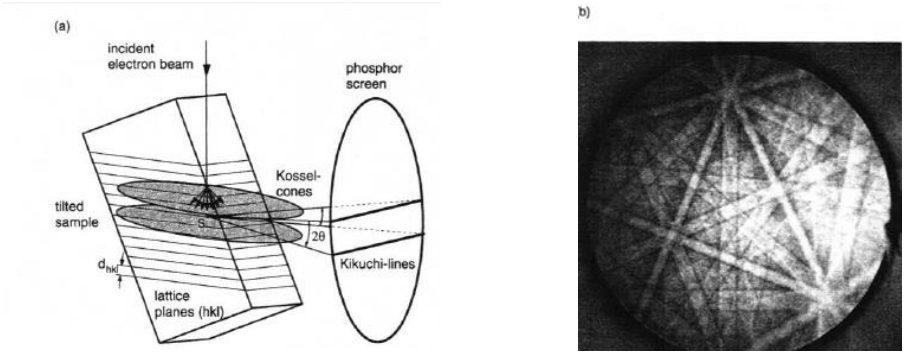

Figure 5. a) Origin of Kikuchi lines from the EBSD (i.e. tilted specimen) perspective, and b) EBSD pattern from nickel (accelerating voltage 20kV). (Randle, 2000)

A statistically significant large number of these measurements can easily be made in automated EBSD systems to allow for a wealth of extractible microstructural information per sample. (Field, 1997), (Randle, 2000), (Dingley, 2009)

2.B.2 Sample Preparation: Focused Ion Beam (FIB) Milling

Advances in focused ion beam (FIB) technology in the last few decades have led to the development of an extraordinary, powerful tool used in: structure and failure analysis of microelectrical mechanical systems (MEMS) (Ishitani, 2007), the production of high resolution structures, integrated circuit repair, and sample extraction for further analysis of a variety of materials for research purposes. (Orloff, 1993) The main capabilities of the FIB technique include scanning ion beam imaging, localized milling on a sub-micron level, and mask free deposition of both metals and insulating materials. (Chen, 2010), (Orloff, 1993) The main components of a FIB apparatus are the ion optical column used to generate, focus, and direct the ion beam, the vacuum system used to reduce contamination of the sample and remove sputtered material, the sample working stage that can be moved in the x, y, and z directions, as well as rotationally, or into a tilted position, and the computerized user interface. (Chen, 2010), (Giannuzzi, 2005)

High precision milling, or micromachining, of materials on a micron/sub-micron level is possible due in large part to the development of the liquid metal ion source (LMIS) as a byproduct of electrostatic rocket engine research. (Orloff, 1993) Adaptation to focused beam work proved beneficial in providing a steady, high in brightness, small in radius beam of current for relatively long periods of time. (Chen, 2010) An ultra-fine diameter beam is achieved first by wetting a substrate, usually made of tungsten, in the shape of a blunt needle with end diameter approximately 2-5μm, with a LMIS in the

presence of an electric field to form what is called a Taylor Cone. An electric field of approximately 10^{10} V/m is achieved by applying a potential difference of approximately 100- 1000 kV to the needle with respect to an extractor electrode. A balance between electrostatic and surface tension forces leads the liquid to form a cone around the needle tip with an apex of approximately 5 nm in radius. See Figure 6 for illustration. The high electric field at the small apex of the cone causes ions to be formed through field evaporation and field ionization of metal atoms. (Orloff, 1993), (Giannuzzi, 2005), (Chen, 2010)

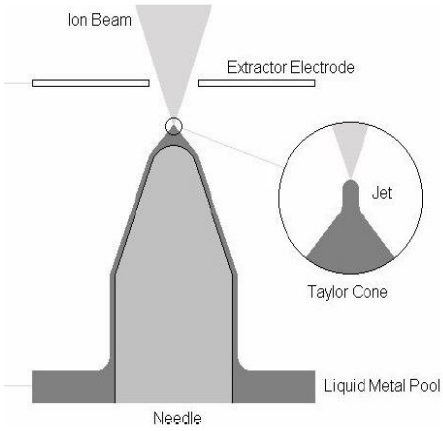

Figure 6. LMIS illustration. (Retrieved from http://www.advanced-materials.at/images/Bilder SPA liquid metal ion source.jpg)

Several metals have been successfully used; however, gallium is used in most commercial FIB systems (Chen, 2010) for its properties that are conducive to a longer lasting stable beam. (Giannuzzi, 2005)

The FIB optical column serves to accelerate the ions away from the surface of

formation and focus them into a high density beam, adjust to the desired current, shift between modes of operation if necessary, and direct the beam path in scanning procedures. Ion optics is a special field in physics that includes the calculation of electric and magnetic fields created with respect to the geometry of various combinations of electrodes and pole pieces. These fields are referred to as lenses as they direct the trajectory of the charged particles (Orloff, 1993), similar to the operating function of different shapes and combinations of glass lenses on the path of light waves. Figure 7

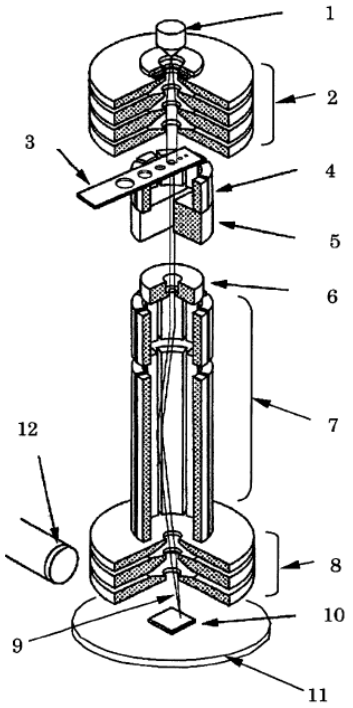

Part No:	***Description***
1	*LMIS*
2	*Condenser Lens*
3	*Beam Limiting Aperture*
4	*Aligner/Stigmator*
5	*Blanker*
6	*Blanker Plate*
7	*Electrostatic Deflector*
8	*Objective Lens*
9	*Beam Current*
10	*Specimen*
11	*Specimen Stage*
12	*Charged Particle Detector*

Figure 7. Schematic configuration diagram of an ion optical system included in an FIB apparatus. (Adapted from U.S. Patent No: 7,235,792 B2)

displays a general schematic of an FIB system. The top of the apparatus houses the LMIS where a steady voltage is applied to warm a reservoir of gallium metal to a liquid. When the ions are successfully extracted, the condenser lens works to form a dense beam probe. The beam limiting aperture is then used to provide a range of beam currents from pA to

20-30 mA. The aligner/stigmator is used to fine tune the beam. (Giannuzzi, 2005) The blanker is used to redirect the beam in order to keep it from reaching the specimen when not being used. The blanker plate captures the beam that is continuously on during operation, but not needed during segments of specimen work. (Fuchs, 1990) The electrostatic deflector serves to raster the beam for scanning operations, and the objective lens is used to focus the beam on the specimen. (Giannuzzi, 2005) The charged particle detector detects secondary charged particles emitted from the specimen due to ion beam interactions with the specimen. (Ishitani, 2007)

The FIB tool can operate in high current density beam mode for milling, and in fine beam mode for image observation, in essence, as a scanning ion microscope (SIM). (Ishitani, 2007) It has been advantageous to combine FIB and scanning electron microscope (SEM) systems into a dual FIB/SEM instrument in order to conduct operations on a specimen using the FIB, and to observe such operations using the SEM. (Young, 2004) This reduces operation time and the probability of undesirable effects associated with surface damage or gallium ion implantation into the specimen by the FIB probe. (Sakata, 1999)

One of the most beneficial aspects of the FIB technique is that applied to the cross sectioning of fabricated structures with drastic differences in component material hardness. Mechanical methods may lead to round off at interfaces when softer surfaces polish faster than harder surfaces, delamination of surface layers, or destruction of the structure. (Giannuzzi, 2005) FIB technique allows for the precise targeting on an area of interest leaving the surrounding areas free of damaging forces. When the high energy ion beam irradiates a surface area the ions penetrate the material and trigger a collision

cascade or collide directly with the surface atom. Kinetic energy is transferred to surrounding atoms. If energy greater than the surface binding energy is transferred to a surface atom then it is sputtered away from the material. The beam dwell time can be programmed into the user interface. Surface damage, to various degrees, by this technique at the atomic level is present. The extent to which it is significant depends upon the analysis being conducted. Such damage can be reduced by careful beam direction placement. (Fuchs, 1990)

2.B.3 Automatic Orientation Imaging Microscopy (OIM)

Automatic Orientation Imaging Microscopy (OIM) allows for the evaluation of EBSPs for a large number of data points, within a fairly reasonable amount of time, providing statistically reliable information regarding the microstructure of a material. Fully automated analysis of EBSPs was developed in the early 1990s. (Lassen, 1998) Automatic OIM is a SEM based tool, (Randle, 2006), a general schematic of which is shown in Figure 8. A prepared sample, one with a smooth flat surface, is placed on the sample stage to be inserted into the vacuum chamber of the SEM system. The normal of the surface is tilted 70˚ with respect to the electron beam. This is done to minimize the depth of the electron probe to enhance the probability that scattered electrons will emerge from the specimen for detection. (Randle, 2000)

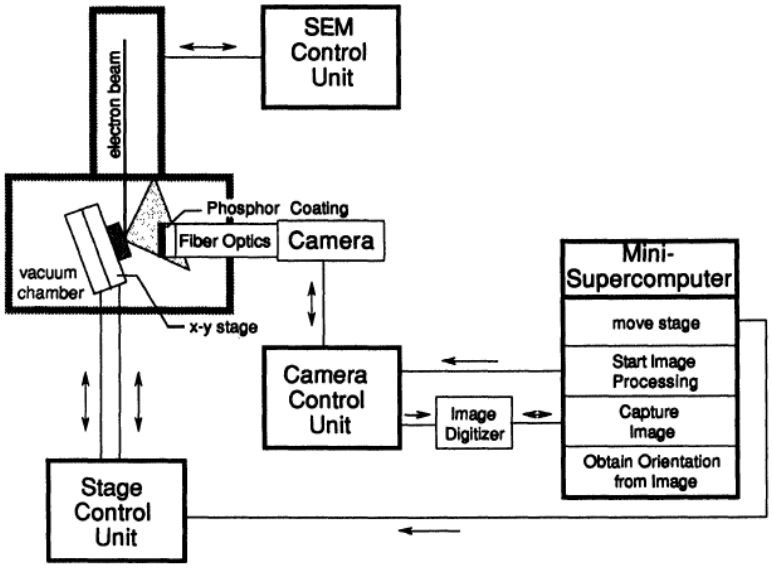

Figure 8. Schematic of automatic single orientation measurement system. (Kunze, 1993)

EBSD resolution is in large part dependent on the SEM electron probe current delivery into the smallest region of focus. (Field, 1997) The electron beam scans the specimen to facilitate evaluation of EBSPs at points a step length distance apart along a hexagonal grid superimposed upon the sample specimen. Step length and evaluation points, not necessarily in a hexagonal grid, may be programmed into the automated system. The chosen step size depends on the material of evaluation, and is limited by SEM capabilities.

The backscattered electron image is projected onto a phosphor screen. The projection has a crystalline symmetry gnomic type distortion which is accounted for and easily adjusted by the image processing program. (Dingley, 2009) The activated phosphor generates a light signal which is captured by a high gain fiber optics video camera. (Lassen, 1998), (Kunze, 1993) The captured image is then processed by the camera control unit. Several frames are averaged, and a background signal subtracted to

produce a final image that is digitized in preparation for implementation of band recognition techniques. (Kunze, 1993)

The detection of true Kikuchi bands is essential for reliable data collection. When a fully automated OIM system was first introduced, the Burns algorithm was implemented with a very high degree of accurate band detection. Since then, band detection has been improved by the development of the Hough transform, which is more robust to noise, and is used in most applications today. (Lassen, 1998) Once the bands are detected, inter-band angles are measured, typically to a precision of 0.5°, and a gnomonic transform is used to correct for distortions in the projected image. Lattice parameters, *hkl* indices, are assigned to the crystal at the evaluation point by comparing the measured angles to all known inter-planar angles of the phase of the given material previously calculated using identified high intensity planes in prior experiments. A triplet of Kikuchi bands will generally provide a unique *hkl* indices assignment if one other point in the pattern, such as the pattern center is known. (Field, 1997) Crystalline orientation is then calculated by comparing the assigned indices to the reference axes of the fixed sample. (Dingley, 2009), (Field, 1997)

Comparison of inter-planar angles for a triplet of Kikuchi bands in some instances, given a non-zero tolerance angle, will identify more than one solution. When this happens, the program will assign a 'vote' for each possible solution for a particular triplet of bands, and will do this for all triplets within the pattern. The number of votes, V_2, for the solution obtaining the second highest number of votes, is subtracted from the number of votes, V_1 obtained by the solution acquiring the highest number of votes, and this quantity is then divided by the total number of identified possible solutions, S_{TOT}.

The program will assign indices in harmony with the solution acquiring the most votes, and a factor called the confidence index (CI), $(V_1 - V_2)/S_{TOT}$, is given as an indicator of confidence in the final solution. (Field, 1997)

What the CI means in automated OIM is very well illustrated in David P. Field's (1997) article, *Recent Advances in the Application of Orientation Imaging.* He discusses the results of an experiment conducted on a poor EBSD image quality FCC single crystal material, wherein at least 6 Kikuchi bands are identified. Analysis was conducted 100 times each for the crystal at 5 different orientations. The results from the study were compiled to give a relationship between CI and the number of EBSPs correctly identified as shown in Figure 9. Note that for CI equal to zero, the fraction correct is still about 40%. More than one solution may likely be present because the two or more theoretical

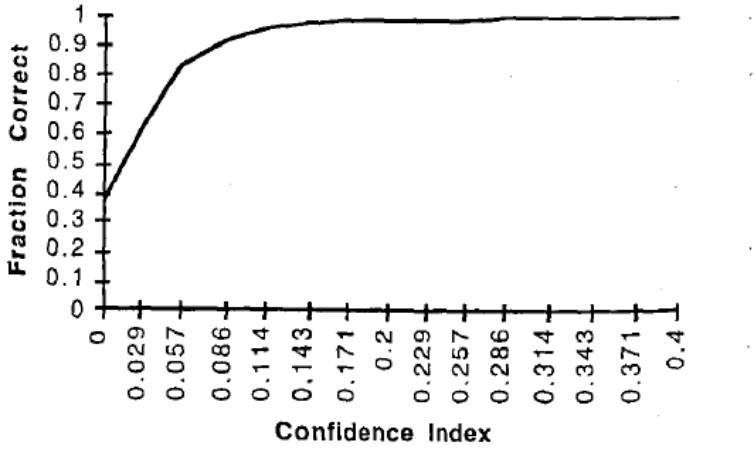

Figure 9. Confidence index (CI) versus fraction of correct solutions for poor quality FCC materials assuming at least 6 Kikuchi bands are identified. (Field, 1997)

solutions fall within the angular tolerance level. If the two with the highest number of votes have an equal number of votes, the CI will be zero; however, the solution with the least deviation from the theoretical value will be chosen, and is often the correct solution. Note that at a low CI of 0.114 about 95% of the images are correctly indexed.

2. B.5 Limitations

While automated OIM analysis of many metal materials is nearly 100% accurate (Field, 1997), ceramics have proven to be more challenging. It is more difficult to achieve a smooth surface, which leads to weak Kickuchi patterns. Rough surfaces tend to trap incident electrons causing charging effects. (Shih, 2007) (Field, 1997) This effect can be minimized by attaching a conducting material, such as copper to the sample surface. (Field, 1997) SiC also has constituent atoms with lower Z numbers than that of metal elements, leaving them less likely to have scattering interactions, thus producing a significantly weaker maxima signal. (Fuchs, 1990) (Field, 1997) (Loretto, 1984) Resolution of grain sizes is limited to the resolution of the electron beam, and electron beam drift becomes a problem for small step sizes in the sub-micrometer range causing vertical black wavy lines in the resulting image. Minor disruptions in lab environment conditions can trigger beam drift; however, statistical reliability of the data is not usually affected by slight drift. (Field, 1997) Gallium ion implantation can distort the lattice and hinder the trajectory of emerging electrons by coulomb forces. This FIB sample preparation effect can be minimized by using a low beam accelerating voltage during polishing, and by carefully choosing the direction of the beam during milling to avoid implantation on the surface of interest. (Giazzunni, 2005), (Steckl, 1998), (Sakata, 1999)

2. C Grain and Grain Boundary Characteristics

2. C.1 Grain Size

Grain size for CVD coated SiC has been reported to be between 0.5μm (Tan, 2007) to 5μm in diameter, and up to 20 μm in length for columnar grains. (Lopez-Honorato, 2009) The OIM program reports the average diameter as a function of the grain area:

$$D_{avg} = (1/N)\Sigma\ [2*(A_n/\pi)^{1/2}] = (1/N)*\ \Sigma\ [2*(f_a M_n/\pi)^{1/2}] \quad (1)$$

Where D_{avg} is the average grain diameter, N is the number of points, An is the area of the nth grain determined by the number of points, Mn, in the nth grain, and f_a is a factor dependent on the step size, and whether or not the evaluation grid is square or hexagonal. ASTM values may also be calculated by the program, and many charts regarding grain size such as grain area vs. area or number fraction can be plotted to visualize the composition of the material. (TexSEM Laboratories, Inc. , 2007). It is likely that grain size affects macroscopic properties of the material; however, increases in porosity and concentrations of impurities are recognized as more significant in some instances. (Snead, 2007) Spherical CVD coated particle grains tend to increase in size along the outward radial direction. (Field, 1993), (Kirchhofer, 2013) The addition of an inert fluent gas, such as argon, in the CVD coating process has demonstrated the result of more uniformity of grain size across the radius. (Lopez-Honorato, 2009), (Kirchhofer, 2013) Size is considered to be extremely relevant regarding the structure of the resulting grain boundaries. Finer, more uniform in size grains, tend to increase grain boundary density, minimizing fission product transport (Helary, 2006), and palladium attack which has been shown to be a significant source of SiC degradation. (Lopez-Honorato, 2010)

2. C.2 Orientation Topography

EBSD can reveal the spatial layout, or the orientation tomography, also known as microtexture, of polycrystalline materials through orientation mapping. Several different types of maps can be generated, such as: the pole figure, the inverse pole figure, along with image quality (IQ) and grain maps. The pole figure (PF) is a two dimensional projection of the intersection of a vector normal to a crystal surface with a unit sphere aligned with the sample geometry conceptually enclosing the crystal. The accumulation of these points for a particular crystal surface is represented by iso-density contours. This is a quick visualization of the polycrystalline microtexture. The inverse pole figure (IPF) represents the projection of the sample coordinate system into the crystal coordinate system. See Sections 4.A.1 and 4.A2 for examples of the IPF map. The IQ map is a representation of the comparative sharpness of individual patterns. The sharpness of an image can be influenced by lattice defects, the quality of the sample surface, and internal stresses. The resulting degree of sharpness can be achieved by a variety of factors, therefore the information obtained from this type of map is only qualitative. Grain maps display differing grains and their relative sizes in their spatial proximity. (Randle 2000) These maps, and many others including those displaying special grain boundary information are automatically generated in OIM packages.

One of the main advantages of the EBSD technique is the ability to characterize grain boundaries if proper cleaning methods are applied. (Gourgues-Lorenzon, 2008) The desire to collect spatially specific orientation data for statistical grain boundary studies was the primary motivation for the development of the EBSD technique. (Wright, 2006) Automated OIM is capable of identifying crystalline orientation relationships at

boundaries, and a common measurement is the magnitude of the angle between grains of differing orientations known as misorientation. (Randle, 2000), (Wright, 2006).

2.C.3. The Coincidence Site Lattice (CSL)

The coincidence site lattice (CSL) model used for the identification of a subset of special boundaries is an extension of the misorientation measurement. These boundaries are of interest because they often have special properties that are thought to enhance the performance of polycrystalline materials. Σ3 boundaries associated with annealing twins in particular are strongly associated with special properties. Table 3 lists potential properties of special grain boundaries in general.

Table 3. Properties of Special Grain Boundaries. (King, 2006)

General Special Grain Boundary Properties
low interfacial energy
highly anisotropic interfacial energy
low susceptibility to segregation
low mobility, or conversely very high mobility
low susceptibility to grain boundary corrosion
low susceptibility to stress-corrosion cracking
low solute diffusivity
low propensity for heterogeneous nucleation of second phases
low point-defect sink strength
low electrical resistivity

CSLs have a structure resulting from the construct of two crystals with differing orientation sharing the same volume that also happen to share atoms periodically throughout the shared boundary volume. These coincident site atoms form the CSL. CSLs are designated by what is known as a Σ value. This value represents the reciprocal frequency of coincident, or shared atoms, occurring in the merging crystal lattices. For example Σ3 would indicate that every third atom within a CSL boundary atom plane is

coincident. CSL categorization is commonly used for materials in EBSD analysis because the information obtained in a scan is easily processed to determine such orientation relationships. Construction of certain CSL structures can be described by a specified angle of rotation about an identified crystal axis. For example, a Σ3 boundary is formed by a 60˚ rotation about a < 1 1 1> crystal vector. There are numerous angle/axis pair combinations that will result in Σ3 in the cubic system. EBSD defaults to the angle/axis pair combination with the lowest rotation angle. (Randle, 2006) (TexSEM Laboratories, Inc., 2007) See Appendix 1 for rotation angle/axis pairs associated with other low values of Σ. Dislocation arrays that might be present are accommodated by allowing a slight variation in angle rotation from the exact expected rotation. The maximum change in angle allowed is determined by the commonly accepted Brandon criteria:

$$\Delta\theta_{max} = 15^{\circ}/\Sigma^{1/2} \qquad (2)$$

where θ=15˚ is considered to be the angle of differentiation between low angle boundaries, and random high angle boundaries. (Randle 2000), (King, 2006),

2. C.4 Phase

The most prevalent polytypes commonly identified in SiC are 3C, 4H, 6H, and 15R, where C indicates a cubic structure, H a hexagonal structure, and R a rhombohedral crystalline structure. The FBCVD method of fabricating SiC has been successful, within a certain deposition temperature range, in developing a more pure 3C-SiC believed to be more stable than other polytypes with differing crystal structures, especially in the realm of irradiation damage resistance. (Snead, 2007), (Tan, 2008). (Kirchhofer, 2013) Complete microstructure analysis for the TRISO particle SiC layer requires an investigation into the constituent phases of the material. EBSD is capable of easily

distinguishing between the cubic and hexagonal structure, provided the pattern quality is sufficient to identify at least five Kikuchi bands, and the amount of a phase present exceeds resolution limits. Information extracted from the precise, within 2-5˚, measurement of intersecting band angles provides what is necessary to differentiate between the cubic and hexagonal phases as their structures widely differ. (Dingley, 2009)

3. Experimental Procedure

3. A Experimental Equipment

3. A. 1 Sample Description

Small sample sets of TRISO coated surrogate fuel particles, containing a ZrO_2 kernel instead of UO_2, were pulled from various batches of those produced at the NECSA's Advanced Coating Facility (ACF) and Research Coating Facility (RCF). The surrogate fuel particles are designed for materials research in order to analyze the effect of process methods on the SiC layer material in the spherical geometric configuration of the actual fuel particle. Individual layers of the TRISO particles as described in Section 2.A.2 were deposited using the FBCVD method discussed in Section 2.A.4. Batch B was produced at the RCF with a SiC layer deposition temperature of 1510 ºC and deposition rate of 0.17 µm/min. Batches D and E were produced at the ACF with SiC layer deposition temperatures of 1450 ºC and 1510 ºC, respectively. The corresponding deposition rate for the ACF coater is 0.23-0.25µm/min.

The completed coated particles were suspended in an epoxy resin, and mechanically thinned to a hemisphere using a Buehler-Beta grinder polisher, exposing the various layers of coating, and finally polished using a 0.05µm colloidal silica suspension. (van Rooyen, 2011) The samples were further mounted in an epoxy resin as shown in Figure 10 for transport to Idaho State University. The mouse and edge of a standard sized computer keyboard in the background illustrate the relative size of the particles that look like black dots within the cylindrical resin mount. The mount in the figure is upside down to better visualize the particles. Analysis and sample extraction are necessarily conducted through the thickness of the resin as the exposed layers in the

sectioned particles are facing upward while the particles themselves are positioned at the bottom of the mount. An attempt to cut off the excess resin did not achieve desirable results.

Figure 10. Surrogate TRISO cross sectioned fuel particles for analysis mounted in epoxy resin.

Figure 11(a) and Figure 11(b) show magnified SEM views of the exposed cross sectioned face(s) of the coated particles. The particles produced are not perfectly spherical; however, these particles visually display a high degree of symmetry.

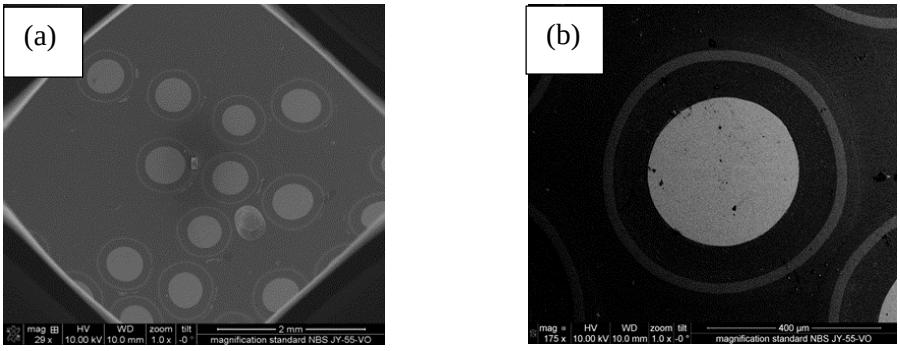

Figure 11. a**)** SEM (29x) image of surrogate TRISO particles, and b) SEM (175x) image of one centered TRISO particle.

The apparent variation in diameter of the particles in Figure 11(a) is in large part due to the fact that not all of the particles were suspended at a uniform level in the epoxy. Consequently, not all particles were cut exactly in half.

3. A.2 FEI Quanta 3D

The samples for this project have all been prepared and analyzed in the FEI Quanta 3D housed in the Microscopy and Characterization Suite (MaCS) at the Center for Advanced Energy Studies (CAES) located in Idaho Falls, Idaho, near the ISU Idaho Falls campus. The FEI Quanta 3D features a duel beam FIB/SEM system used for high resolution imaging and milling of specimens. It is also equipped with a Gas Injection System (GIS) for deposition of various materials such as platinum for specimen marking and probe welding and an OMNI Probe for in situ lift out of samples from a given specimen. See Figures 12(a)-(c) for images of the instrument.

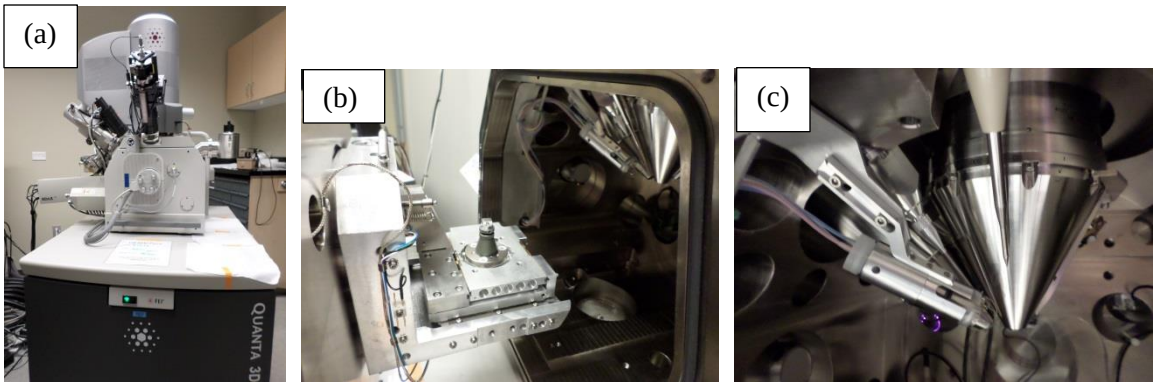

Figure 12. The FEI Quanta 3D with a) SEM at center top and EDAX EBSD fiber optic camera extended to left attached to cables, b) open vacuum chamber with computer controlled automated stage at center, and c) close-up look at system equipment inside vacuum chamber.

It also comes equipped with an automated EBSD EDAX OIM analysis system that can evaluate approximately 900 orientations per hour, and process tens of thousands of orientation images without operator interference. (TexSEM Laboratories, Inc., 2007).

3. B Development of a FIB/SEM sample extraction and polishing technique for EBSD analysis

3.B.1. Method Description

Reliable EBSD analysis of a polycrystalline material requires a smooth surface. (Shih, 2007). Typically, sample preparation methods for analysis of the Sic layer consist of the mechanical grinding of a sample TRISO coated particle embedded in epoxy resin, down to a hemisphere cross section, and subsequently fine polishing by various methods. (Tan, 2008), (van Rooyen, 2011), (Helary, 2006), (Kirchhofer, 2013) Tan et al.(2008) used diamond paste, alpha alumina, and colloidal silica solutions in given order with successful results. Nevertheless, in many instances, difficulties have been encountered by TRISO particle researchers with mechanical and chemical grinding and polishing of sample surfaces. Kirchhofer et al. (2013) report a similar process resulting in poor edge retention at the SiC/IPyC interface, which was unacceptable, and a FIB/SEM sample extraction was used instead.

Another difficulty that arises is the handling of very small objects. Mounting and proper alignment are difficult without the aid of a high powered microscope. Helary et al. (2006) report an awkward ex situ transfer of the cross sectioned particle from the epoxy to the SEM sample stage wherein alignment of the cross sectioned face needs to be exactly parallel to the sample stage.

A FIB/SEM in situ sample extraction method and polishing technique was developed for TRISO particle EBSD analysis by Dr. Isabella van Rooyen (Nuclear Materials Scientist at INL), Jatu Burns (Instrument Lead at CAES), Jim Madden (INL), and Tammy Trowbridge (INL) in an effort to address the problems of interface damage between materials of different hardness, and the difficulties of tiny specimen alignment

outside the SEM tool. FIB milling can sputter materials of differing hardness in a highly localized manner with a beam probe approximately 5 nm in diameter. Consequently, FIB cross-sectioning through materials of differing hardness has a much better outcome than that from mechanical methods. (Chen. 2010)

The sample extraction method starts with a mounted cross-sectioned hemispherical fuel particle placed in the FIB/SEM system. The GIS system is used to deposit a platinum marker about a random portion of the exposed SiC ring. This marker is used as a guide to mill the surrounding material away in order to expose a segment surface of the SiC layer between the IPyC and the OPyC layers that was not exposed to the potential grinding damage in the original cross section preparation. For an illustration of the relative location of the layer see Figure 13.

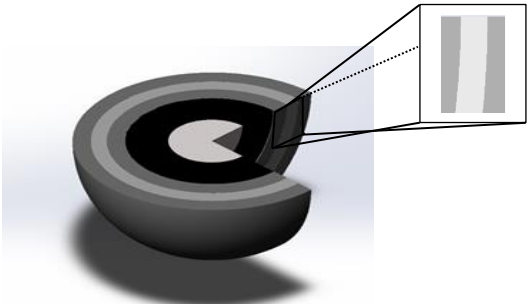

Figure 13. Illustration denoting surface location for EBSD analysis.

Two segments on the top and bottom of the marker are milled in the form of a wedge while the stage is tilted 52˚. This is done in order to make room for the FIB to cut the bottom sample surface on both sides at a 52˚ angle while the sample is in the upright position. The OMNI Probe is welded onto the sample for in situ lift out. The sample stage is cleared, and a small, pre-tilted, clamped grid containing sample platforms proportional to the micron scale of the extracted sample is secured to the stage. The

sample is then brought to the grid platform with the OMNI Probe in order to weld the sample onto the platform for further polishing. Alignment is aided by the platform geometry and SEM imaging. The polishing then proceeds at a low potential of 5 KeV in order to avoid gallium ion implantation. The current is adjusted to differing values between surface scans to fine polish the surface of interest. Sample extraction, polishing, and EBSD scanning are all done in one chamber. A more detailed description of the entire process is given in the following section.

3.B.2 Step-by-Step Implementation

Install Specimen: The vacuum chamber of the dual beam instrument first must be vented. The specimen is then placed in a hole in the stage, and a small screw is used to secure the specimen in place. The system is equipped with a height gauge to check for adequate clearance (~10mm) between the specimen and the SEM probe forming lens. The chamber door of the system is then closed, and the vacuum system controlled by the system software is turned on to remove free particles from the chamber.

Microscope Set-Up: In the dual beam system, the electron beam is commonly referred to as the E-beam, and the ion beam as the I-beam. When the vacuum system is ready, both beams are started. The E-beam is used first to set up the microscope. An acceleration voltage and current or aperture size is selected. Acceleration voltages in the range of 2 – 30 KeV are generally used. (Fuchs, 1990) An acceleration voltage of 10keV and a current of 0.33 mA were used for this specimen. Different currents can be tested to find the best resolution for the material of investigation. A working position is established by magnification of the E-beam image to 2000X, or greater, and centering on a distinct characteristic of the material as the Z coordinate of the specimen is gradually adjusted to

the desired working distance of 10 mm. If a good image cannot be obtained, which is common for ceramic materials, a coating of Au-Pt can be added to the sample to give the surface conductive properties. A coating of Au-Pt was added to sample B1600 in this study to generate a discernable image.

Eucentric Height Adjustment: Set magnification to 3500X and center the area of interest. Tilt sample 5-10 degrees. Bring area of interest to center using *z*-control only and repeat until sample is brought to center while tilted 52 degrees.

Ion Beam Set-Up: Select "zero beam shift" under Beam Control. Under I-beam menu select the 10-30 nA setting. Obtain a focused I-beam image, and use the X-Y beam shifts to center image at 3500X.

Platinum Deposition: Change I-beam setting to 2-6 pA/pm^2 and adjust brightness and contrast to refocus the image. Turn on Pt-Gas heater, and insert GIS needle when the program indicates it is warm enough for operation. Use the patterning tools to draw a rectangle around the area of interest. Figure 14 shows the rectangle drawn around a segment of the silicon ring between two layers of pyrocarbon. A thin platinum layer is deposited to serve as a marker for ion beam bulk milling.

Bulk Mill: The segment of interest is the bottom face of the drawn rectangle extending into the page shown in Figure 14. It is desired to achieve at least a 35μm depth extended from the top open face of the cross sectioned particle. In order to reach this length, wedge shaped trenches are dug into the material just above and below the platinum marker. The volume to be milled is programmed into the system as a box. If a depth of 35μm is desired, the upper box surface rectangle would need to be drawn with

sufficient dimensions to compensate for the redeposition of milled material that is not carried away in the vacuum system.

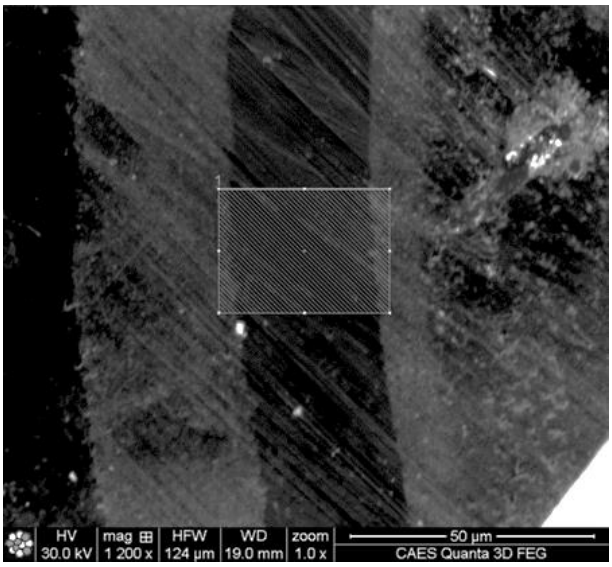

Figure 14. SEM image (1200x) of the dimension settings for GIS deposited platinum marker used in preparation for ion beam milling segment extraction of the sample B1600 SiC layer.

Debris build up is a common occurrence in deep trenches. The *x*-dimension of the trench is set by visual inspection. The *y*-dimension in this instance was given dimension value of one and a half times the desired depth. Figure 15(b) illustrates the milled trenches for B1600 sample extraction. When the dimensions of the upper rectangular layer of the trench are established using patterning tools, the ion beam is ready to raster across the chosen rectangle, sputtering material as it goes.

Figure 15(a) is an image taken at the beginning stage of milling the first trench. Note the difference in texture between the surrounding pyro-carbon layers and the SiC layer.

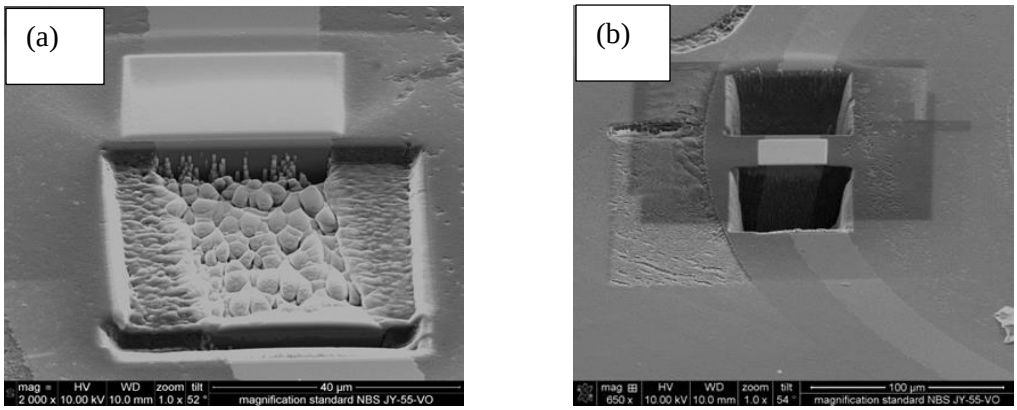

Figure 15. SEM images a) **(**2000x) at the beginning stage of ion beam bulk milling for sample extraction from sample B1600, and b) (650x) at completion of bulk milled trenches above and below platinum marker.

The texture as displayed by the SEM at 2000X magnification (Fig. 15(a)) gives the appearance that the SiC layer grains have a more spherical shape as opposed to the long columnar grains along the radial direction typical of the CVD coating process. Also, the SiC grains do not appear to increase in size from the IPyC layer to the OPyC layer. It is not certain that this image indicates the actual material grain characteristics; however, it does illustrate the problematic rough surface common to ceramic materials for EBSD analysis.

Figure 16(a) shows the resulting debris formation in the bulk milled trench and the redeposition of material onto the surface of interest. The specimen platform is tilted to 52˚ in order to achieve a 90˚ angle between ion beam and specimen surface during bulk milling. To clean the debris off of the face of interest, the platform is tilted an additional 2˚ to 54˚. A small rectangle is drawn by the patterning tool near the edge of the platinum marker, and the ion beam is employed to sputter material to the required depth within the chosen area. This procedure exposes the SiC layer. See Figure 16(b). Another trench is milled in similar manner on the opposite side of the platinum marker.

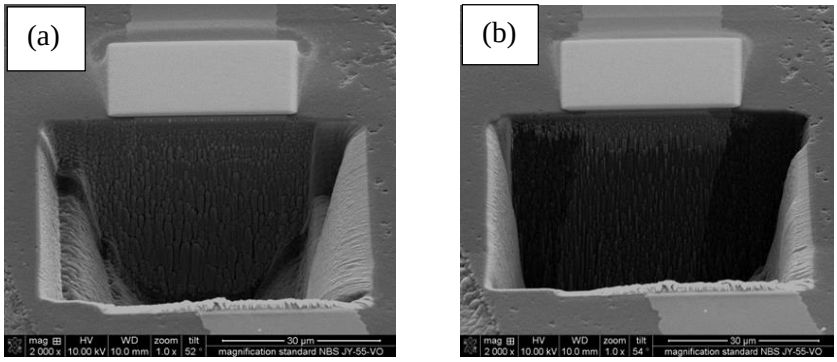

Figure 16. SEM images (2000x) of a) a completed bulk milled trench, and b) the same trench after debris removal by tilting specimen to 54˚ and using the ion beam to sputter debris away from surface of interest.

The material immediately to the left and right sides of the platinum marker are then sputtered away using a similar method; however, a large trench is not necessary. See Figure 17. A rectangle is drawn on each side of the marker for the rastering pattern of the ion beam, and subsequently the material within the chosen area at the desired depth is removed by the ion beam.

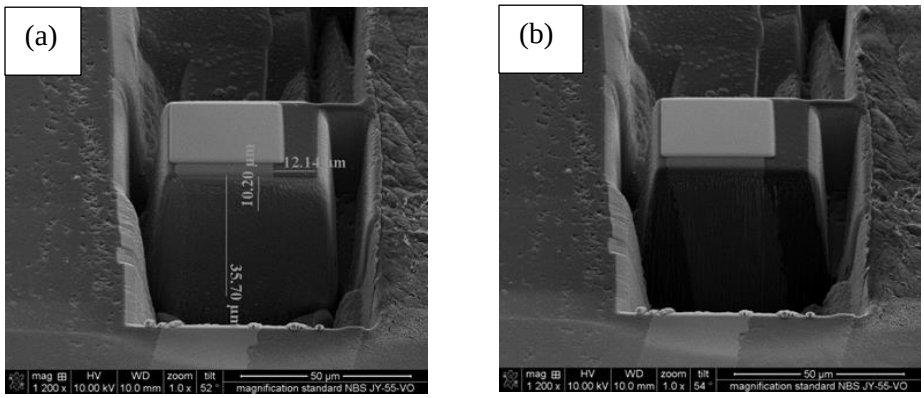

Figure 17. SEM images (1200x) of sample B1600 a) after bulk-milled trench and side cuts, and b) after milling debris curtain from surface of interest at a specimen tilt angle of 54˚ from the vertical.

As shown in Figure 17, a small arm of material is left on one side in order to stabilize the specimen during cutting of the bottom portion for final sample separation from the specimen.

The stage is tilted back to the upright position. This will allow the I-beam which is at an angle of 52˚ with respect to the vertical to slice segments in the bottom of the sample in preparation for removal. See Figure 18 for a sketch illustrating the step. The I-beam consecutively passes unhindered through each milled wedge shaped trench, to form a V shaped cut on the bottom of the sample when viewed from the side.

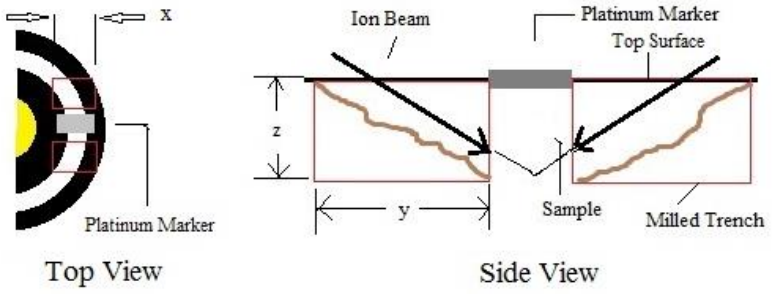

Figure 18. FIB sample extraction step sketch.

The arm on one side continues to hold the sample in place while a probe needle used for lift out is welded to the sample using the platinum deposition feature. See Figures 19(a)-(d).

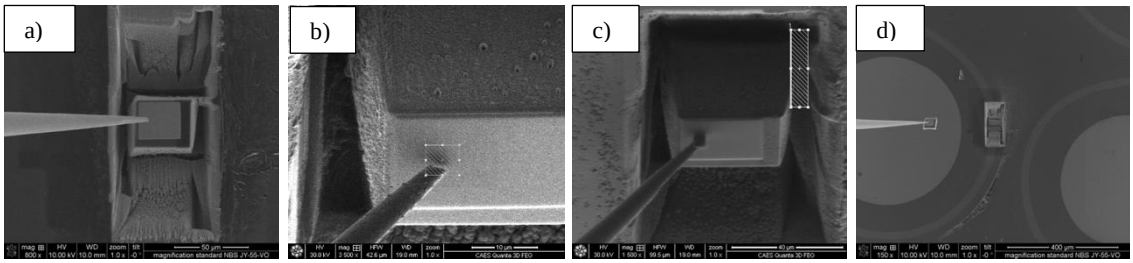

Figure 19. a) SEM image (800x), insertion of probe needle in preparation for sample lift out, b) FIB image (3500x) of white square box indicating position marked for platinum weld of needle to sample, c) FIB image (1500x) of white rectangle marking for FIB milling of side arm, and d) SEM image (150x) of the sample successfully lifted out of specimen.

EBSD analysis requires that the normal to the surface of evaluation be tilted 70˚ with respect to the vertical. The stage control will not tilt the full 70˚. This limitation is

accommodated by attaching the sample to a grid that is clamped into place by a 45˚pre-tilted mount as shown in Figures 20(a) and 20(b). The next step is to weld the extracted sample onto the sample grid for further processing. The grid appears to be a copper shaving, yet contains special platforms at sample scale useful for alignment purposes.

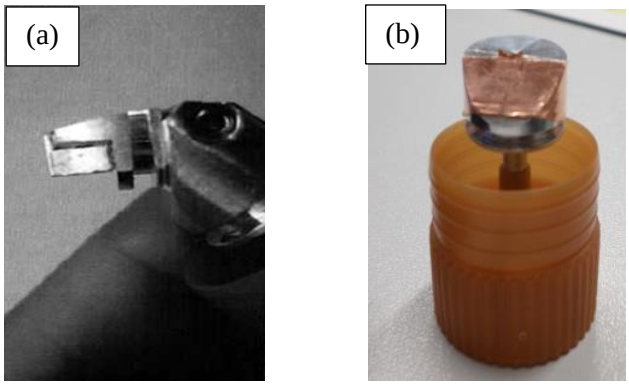

Figure 20. a) 45˚ pre-tilted mount used for sample B1600, and b) 45˚ pre-tilted mount used for 6H phase scan of batches D and E samples.

Figures 21(a)-(e) show FIB and SEM views of the sample mounting process.

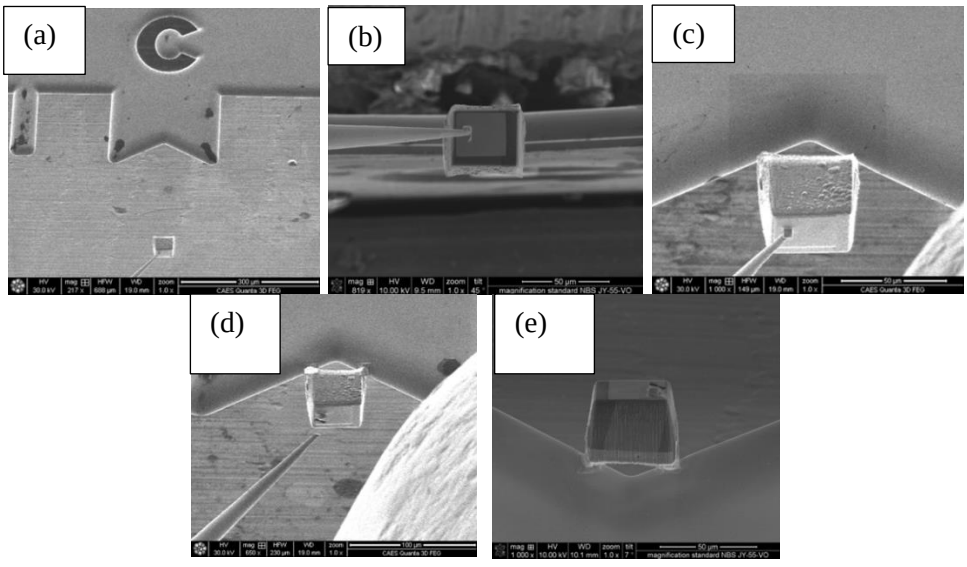

Figure 21. a) FIB scan (217x) view of probe being maneuvered in place for sample mounting, b) SEM view (819x) of centered sample, c) FIB view (1000x) of positioned sample, d) FIB view (600x) of sample welded to platform and removal of needle, and e) SEM view (1000x) of successfully mounted sample at 52˚ tilt

FIB views appear to be upside down. The pre-tilted mount is placed on the stage and the chamber restored to vacuum pressure. The sample still attached to the probe needle is then brought close to the grid and welded using the platinum GIS feature. When the sample is welded securely, the needle is lifted leaving a broken segment of the needle welded on top of the sample. The stage is then tilted 7˚ degrees. This adjustment plus the pre-tilt of 45˚ puts the sample in position for FIB polishing of the sample surface. A series of gradually descending currents (30nA, 15 nA, 7 nA, 1 nA, 0.3nA, 0.1nA, and 48pA at 5keV) were used in an attempt to achieve a gradual reduction in hills and valleys on the sample surface for a smooth finish. The changes in the surface redeposition curtain for these scans are shown Figure 22.

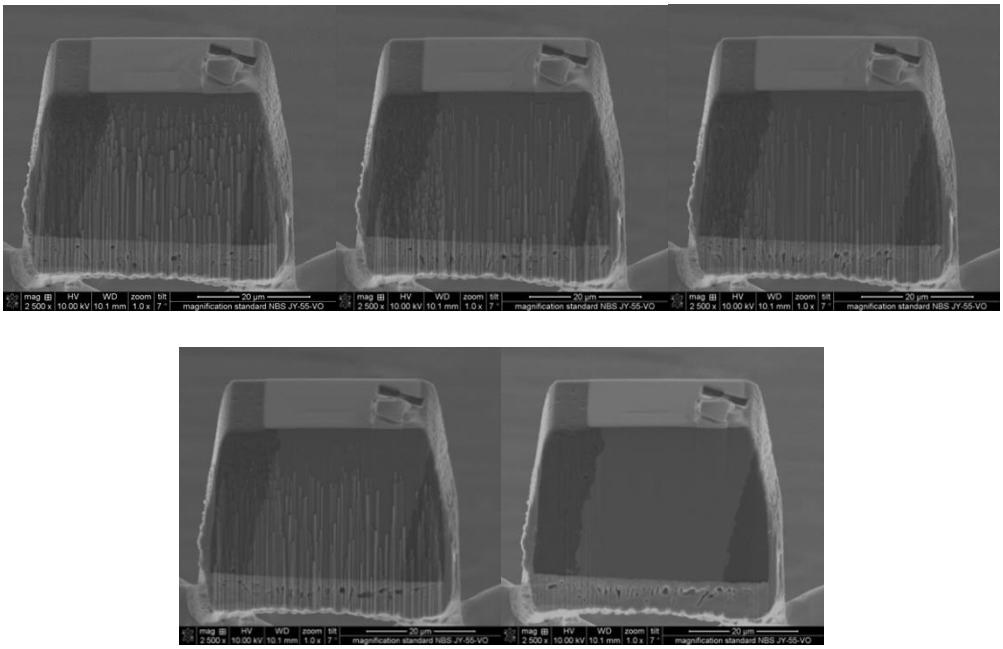

Figure 22. SEM images (2500x) of sample surfaces resulting from FIB polishing, beginning from top left, proceeding left to right, then to bottom left, proceeding left to right with samples becoming progressively smoother with smoothest surface shown bottom right.

3.B.2 Discussion of Results

Figures 23(a)-(d) illustrate the resulting images of EBSD analysis insufficient for microstructure characterization. Ceramics, in general, pose difficulties in providing a sharp signal for EBSP recognition as discussed in section 2.B.5.

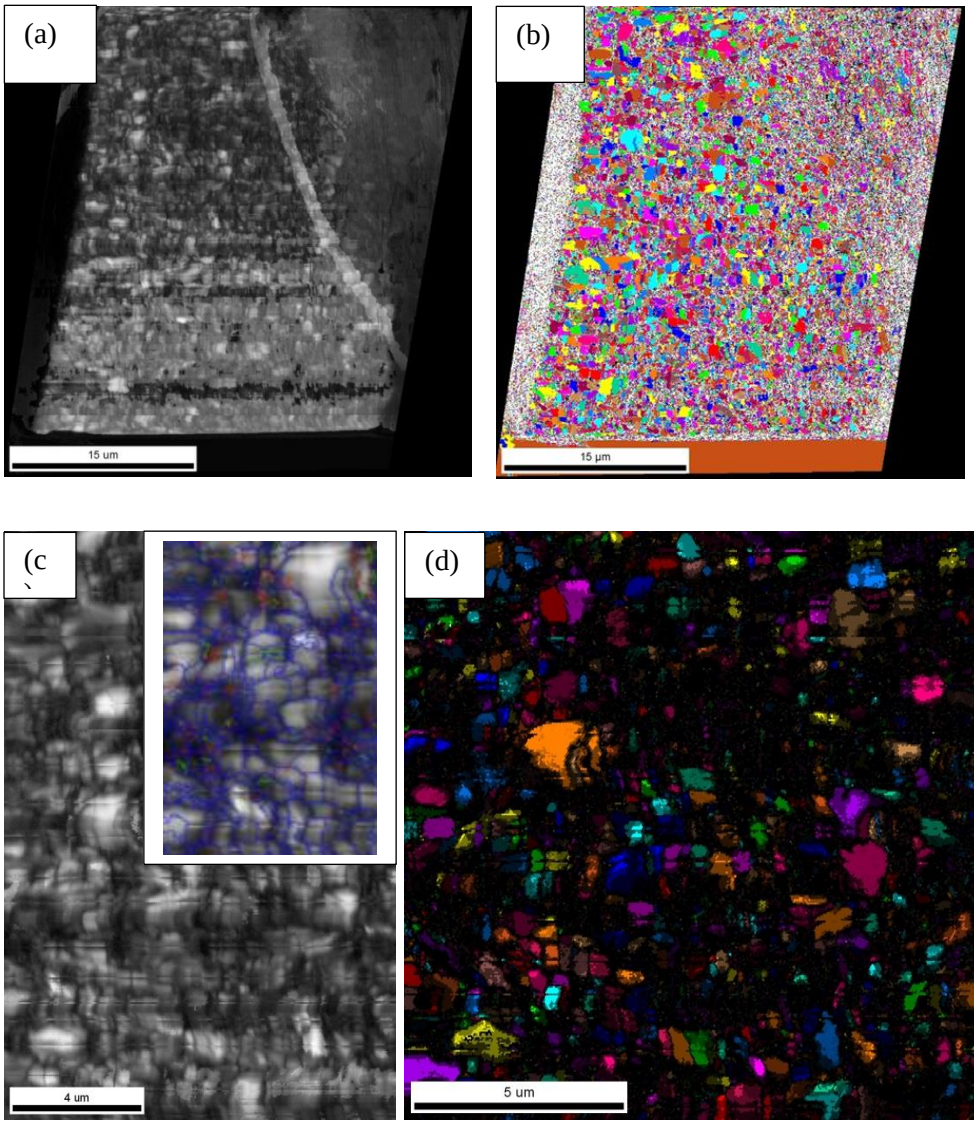

Figure 23. EBSD images from a) SiC-3C IQ scan for B1600, b) Auto IPF for B1600, c) cropped segment of IQ scan for B1600 with grain boundary map window, and d) Auto grain map for B1600.

Yet, these challenges in many instances have been mitigated successfully and researchers have obtained EBSD scans for CVD coated TRISO particle SiC layers that provide reliable information. (Tan, 2008), (Kirchhofer, 2013), (Shih, 2007), (Helary, 2006), (Lopez-Honorato, 2009), (van Rooyen, 2011) Several possibilities remain to explain the cause of signal distortions that render sample B1600 unsuitable for EBSD microstructure characterization. First, a focus on the material itself may provide answers. Figure 24 shows the characteristic strength of samples fabricated under various process conditions. (van Rooyen, 2010)

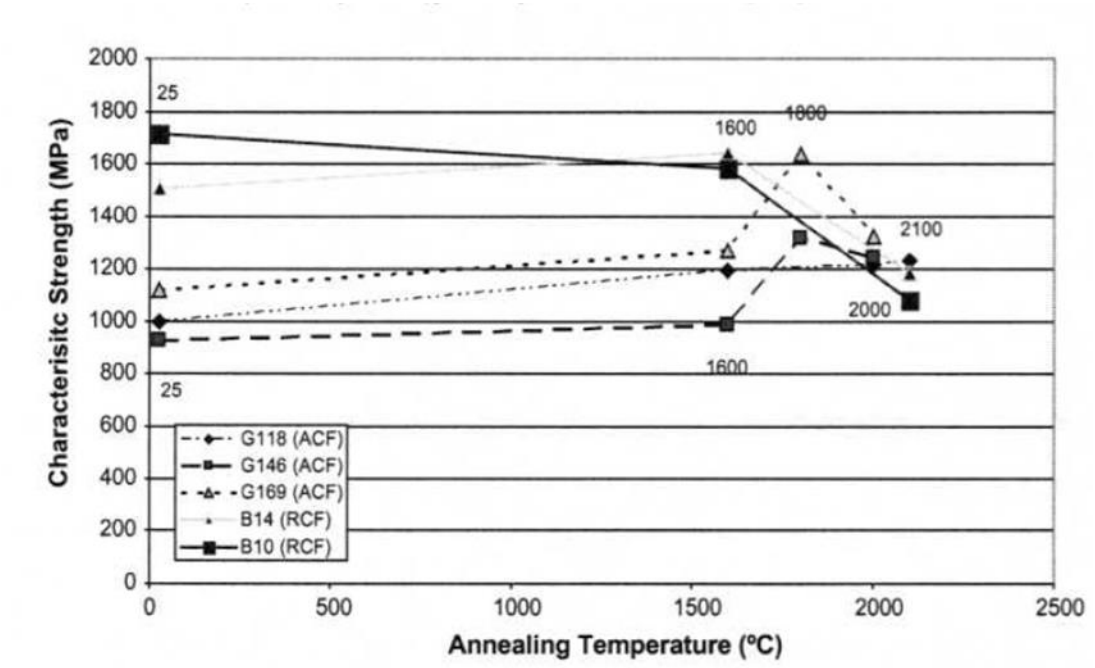

Figure 24. Influence of annealing on characteristic strength of particles fabricated under different process conditions. (van Rooyen, 2010)

Note the B10 sample, processed under similar conditions to those of B1600, is much greater than most of the other particles. Without annealing it has significantly higher characteristic strength than all of the other particles. This difference might indicate stronger chemical bonds that may, in turn, translate to curvature of the lattice and/or

greater difficulty in adequate surface polishing. Combined with the low Z number of Si and C atoms, both conditions could easily lead to the failure of generating sharp Kikuchi bands. It may be that the grains are on average too small, below limits of EBSD resolution.

Next, a focus on the extraction method might provide a possible answer. Direct FIB milling, ion beam perpendicular to the surface at 30kV, has been known to cause a surface layer of amorphous damage several nanometers thick to side walls of milled trenches in materials such as Si. This damage is thought to occur through back sputtered Ga ion implantation and an ion beam induced collision cascade energy transfer throughout adjacent material. (Giannuzzi, 2005) Bask sputtering may be more likely for the stronger SiC material. Figure 23(d) may be a classic illustration of amorphization damage due to FIB milling. If this is the case, then milling away the damaged thickness with a high energy beam at an angle so that the Ga ions do not have a chance to back sputter, and subsequently fine polishing at low energies might correct the problem.

Note the white curve on the surface in Figure 23(a). This indicates a crack in the material that most likely started on the hemispherical cross sectioned surface and propagated down the surface of EBSD analysis during sample extraction. Apparently, backscattered SEM electrons damaged the surface on the upper right side of the crack, see Figure 23(b), enough to nullify any signal significant for EBSD analysis. Figures 23(c)-(d) are cropped from the center of the surface under the crack.

3.C. Sample Extraction Method for Batches D and E.

Sample extraction steps for Batch D and E samples followed a similar sequence as that described in the previous section for B1600, the main differences being the size of the trenches above and below the platinum marker, and the surface plane of examination. The trench size for B1600 was (55 x 60 x 40)µm while the trench size for a Batch D sample was documented as (60 x 25x 10)µm. The surface of examination was the same as the surface of platinum deposit. The platinum was shaved off and the surface polished by FIB at low energy beam. See Figures 25(a) and 25(b) for an illustration of a process step and the final prepped surface.

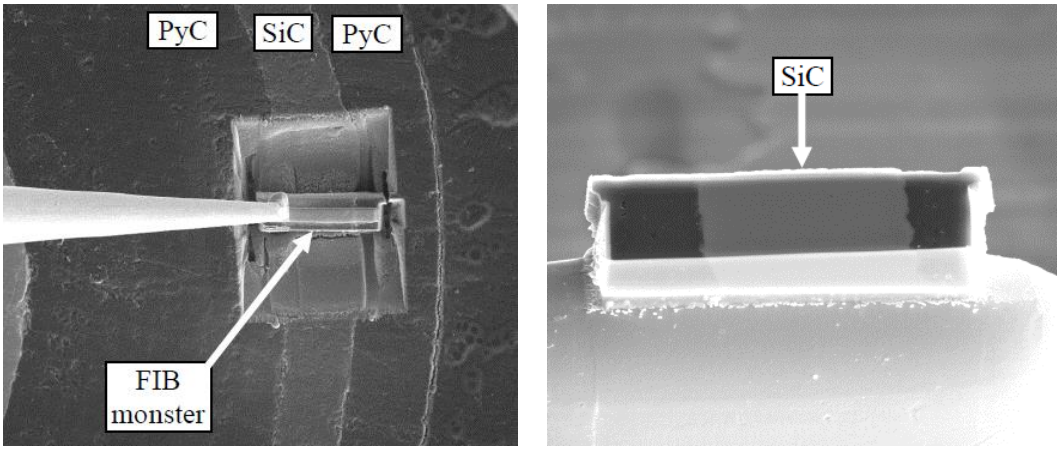

Figure 25. a) Sample prior to lift out from machined wedge, and b) polished sample surface.(van Rooyen, 2012)

3.D OIM Data Collection Methods

EBSD scanning on the SiC layer in TRISO particles is typically done over an area that includes the SiC layer and a portion of the IPyC and OPyC layers in order to retain information about border grains within the SiC layer. Information obtained from the pyrolytic carbon layers would skew the SiC results; however, various methods are designed into the EBSD OIM analysis program to subsequently eliminate the unnecessary data while keeping boundary grain data intact.

It is beneficial to view first the IQ map of the scanned surface. Portions of the scan may be severely distorted, or of very poor quality, while other portions appear to be normal. The program allows for cropping in order to preserve the good quality portion of the image if necessary. Placing the cursor upon the image will give statistics at the bottom of the users screen depicting the IQ value and CI value among other characteristics of the point at the cursor head. This information is helpful in determining a cut-off value for points falling below a certain quality image rating. It is useful to pick an IQ value slightly lower than the grain boundaries near the edges of the SiC layer. Setting up a partition of points for evaluation above this value is helpful in eliminating the unwanted pyrolytic carbon layer data.

Rough surface topography can cause indexing problems in the automated system. Extraneous points at grain boundaries, those not clearly identified as one grain or the other, can cause erroneous peaks in the misorientation distribution. (Wright, 2006) An example of such a phenomenon is shown for a copper scan in Figure 26. To mitigate this type of error, the OIM neighbor orientation correlation clean up method was used on the 3C-SiC scanned samples. The program will identifies a point with three or more

neighbors having the same orientation, and changes that point to the orientation of its neighbors. This procedure is done iteratively.

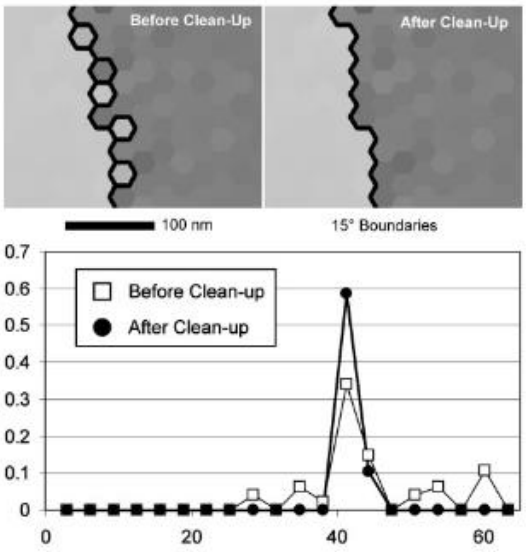

Figure 26. OIM maps and misorientation angle distribution showing impact of data clean-up. (Adapted from Wright, 2006)

The CI standardization clean up feature was then used to assign all the points within the grain the CI rating of the point with the highest CI value. If several points in close proximity are indexed with the same orientation, it is not unreasonable to give the entire group the highest CI rating found among the members of the group since the probability of correct indexing is greater when several neighbors have been assigned the same orientation. This process takes into account the possibility of some areas having a lower IQ and reduces the chance of discarding useful information in a CI level cut off partition. A fit standardization was similarly done as well. See Figure 27 for an illustration of clean up steps.

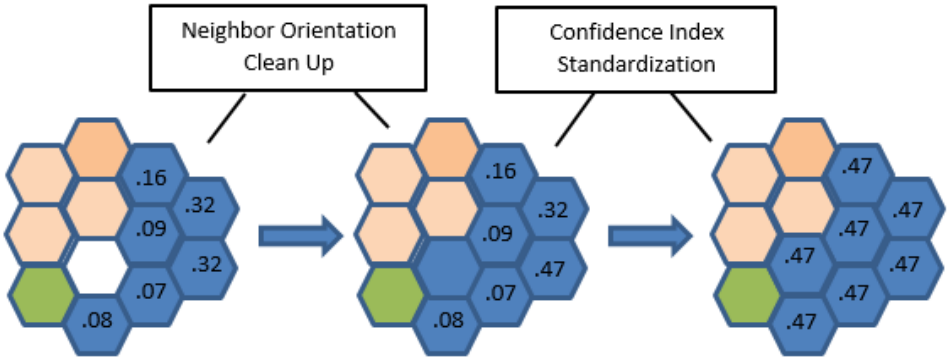

Figure 27. Illustration of OIM data clean-up steps.

A partition of data was conducted to improve the statistical confidence in the data. The partition was performed by eliminating points under a certain IQ value and those indexed points under the CI value of 0.10, for the 3C-SiC scan. The chosen CI value is expected to provide data points correctly indexed well over 90% of the time as demonstrated in Section 2.B.3. It is expected that the 6H-SiC phase, if present, is scattered throughout the matrix. As such, the neighbor correlation and CI standardization methods were not used as clean-up procedures; however, to remain consistent, a partition in the 6H-SiC scan is set up using IQ and CI limits. IQ will be dependent upon the quality of the individual scan and CI is left at 0.10 in harmony with the 3C-SiC scan. It is expected that 6H-SiC will fall into similar indexing accuracy regarding differentiation between the two phases because of the significant difference in crystal structure. True orientation for the hexagonal phase may be more problematic; however, it is expected to be in such small amounts that the hexagonal orientation is not important. Grain boundary analysis will not be conducted on the 6H-SiC scans.

3.D.1 Dref

The 6H-SiC scan was conducted with half the step size, 50 nm, as that of 3C-SiC. Scan time was approximately the same for both samples, leaving the 6H-SiC resulting image about half the size as that of 3C-SiC. Figures 28(a) and 28(b) serve as verification that the same sample was scanned for both phase settings and has nothing at all to do with the abundance of either phase.

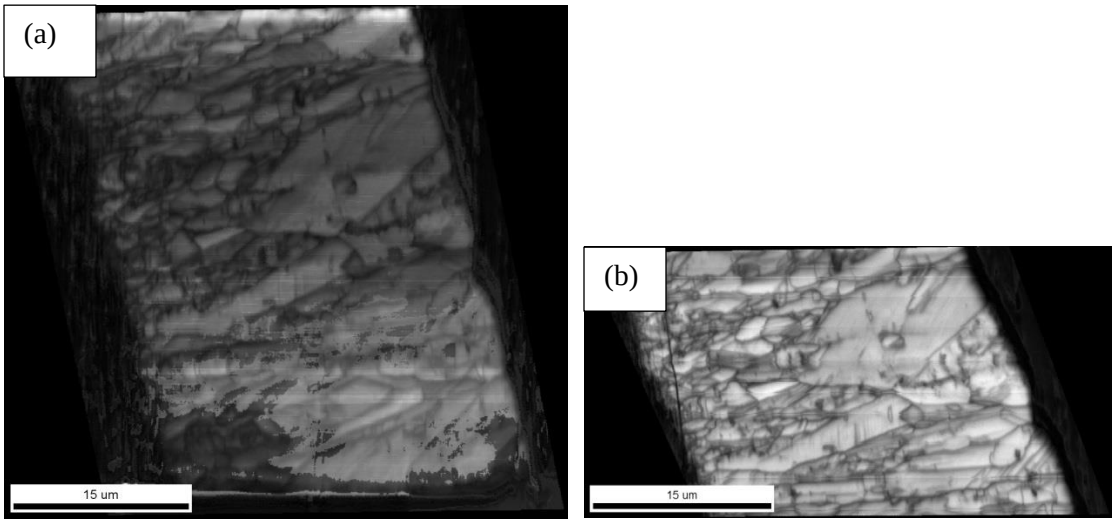

Figure 28. EBSD Generated images of raw data IQ maps for a) 3C-SiC scan D-ref, and b) SiC-6H scan of Dref.

During deposition, SiC tends to get somewhat absorbed into the IPyC layer due to the porosity of the IPyC layer. The OPyC layer is not likely to penetrate into the SiC layer due to its relative hardness. It is typical to see a few conglomerates of SiC disbursed in the IPyC layer near the interface, and a more crisp edge between the SiC and OpyC layers. What appears to be SiC material expanding into the pyrolytic carbon layers in these initial scans is an artifact of the scan, a pattern echo. When the cursor is placed over the echo portion of the scan, a CI value for that point is shown to be zero, or very low. A partition is set up to eliminate both pyrolytic carbon layer points, and these echo

points, as well as points that may likely be incorrectly indexed. Partition parameters such as those discussed in section 3.C, and resulting data statistics are detailed in Section 4.A.1.

3.D.2 D2000

Figures 29(a) and 29(b) display the IQ maps of the D2000 3C-SiC-and 6H-SiC scans. Data partitioning parameters are outlined in Section 4.A.1.

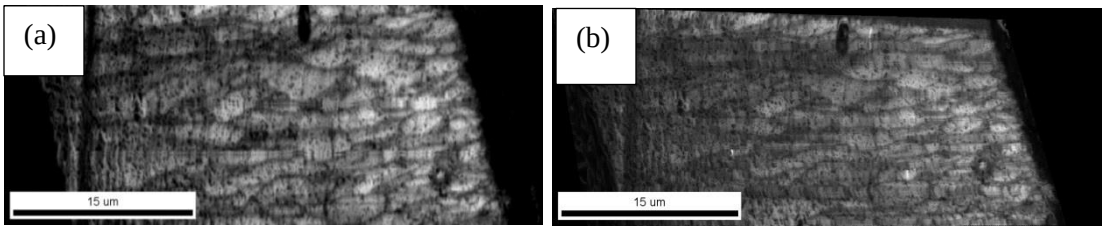

Figure 29. EBSD image IQ map of D-ref 2000 for a) cropped raw data 3C-SiC scan, and b) raw data 6H-SiC scan

The material appears to have small black spots across the surface. This could be due to charging artifacts, or the material surface has been somewhat damaged by several SEM scans. The thick vertical line appears to be a surface crevice, yet it is most likely to be a charging artifact like the spot towards the top middle. This is a small area compared to the total number of points and should not detrimentally affect the analysis.

3.D.3 E-ref

A few thin wavy vertical lines displayed in Figure 30, typical of electron beam drift for small step sizes, are not expected to have detrimental effect on data analysis.

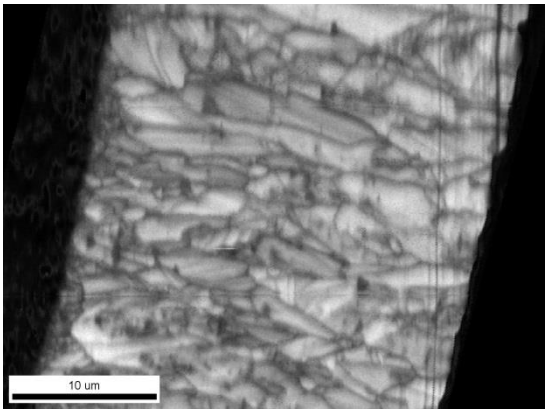

Figure 30. EBSD 3C-SiC scan cropped image of sample Eref.

An example of severe electron beam drift is shown in Figure 31(a) for the 6H-SiC- phase scan. Lab conditions at the CAES were disrupted by road and building construction in the surrounding area. A subsequent scan, Figure 31(b) showed a difference in image quality in the upper portion of the material. Further investigation into the extent of damage is displayed in Figure 29(c). The IPF scan shows a blur of spots where grains are expected. The image was cropped, see Figure 29(d), to discard the damaged data. It is not desirable to lose so much surface area, however, the remaining image still produces tens of thousands of data points of statistical worth in further analysis. Further partitioning of the data is depicted in Table 7 in Section 4.A.2.

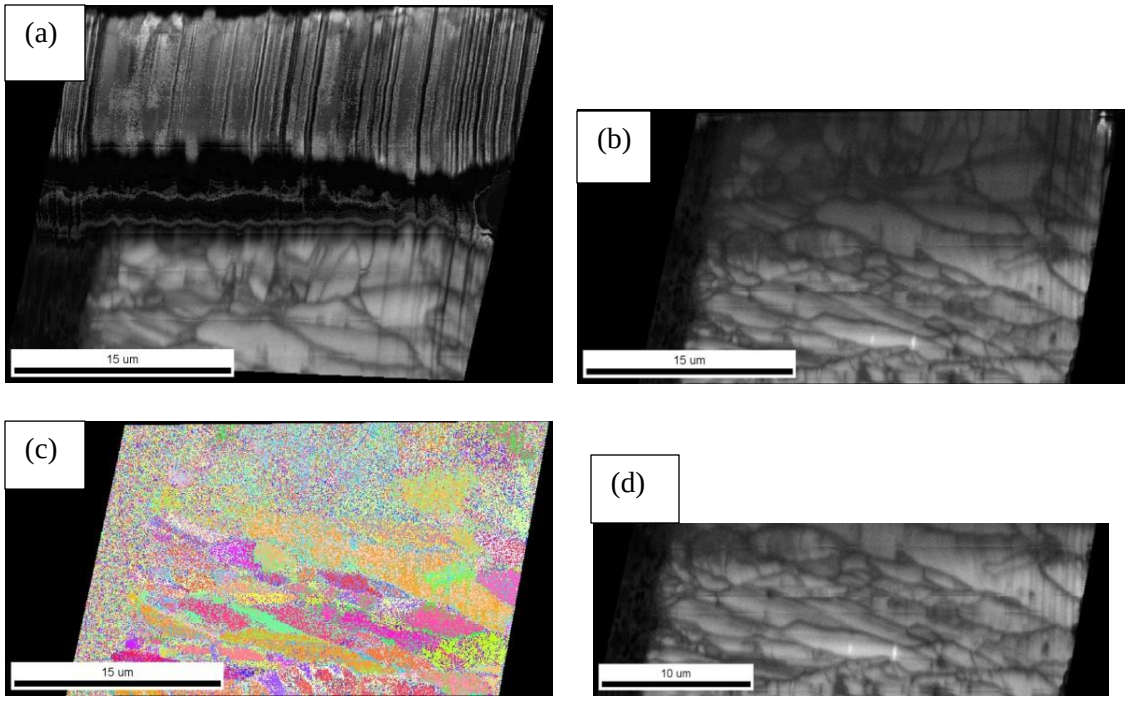

Figure 31. a) E-ref 6H-SiC scan displaying severe electron beam drift during the first part of scan, b) subsequent E-ref 6H-SiC scan, c) IPF showing distortion of data, and d) cropped E-ref image.

3.D.4 E2000

Figure 32 displays 3C-SiC scan images for E2000. The top and bottom edges were necessarily cropped. A 6H-SiC scan could not be done on this sample as it was lost. The platform holding the sample appeared to have broken off the holder. See Section 4.A.2 for further data extraction partition details.

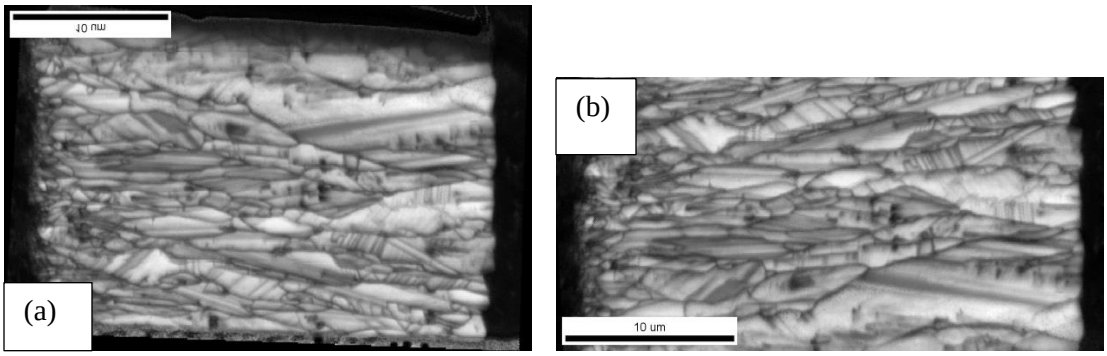

Figure 32. Sample E-2000 3C-SiC scan displaying a) raw data, and b) cropped image.

Chapter 4.0 Analysis of Results

4. A Microstructure Comparison of EBSD Evaluated Samples, Prior and Post Annealing

4.A.1 Batch D: No annealing vs. Annealing at 2000˚C for 30 minutes.

Figure 33 illustrates the random grain orientation via the IPF color coding, and the underlying IQ pattern, a manifestation of EBSD signal sharpness which can be influenced by general roughness, lattice structure dislocations, and irregularities throughout the polycrystalline surface as discussed in Section 2.C.2.

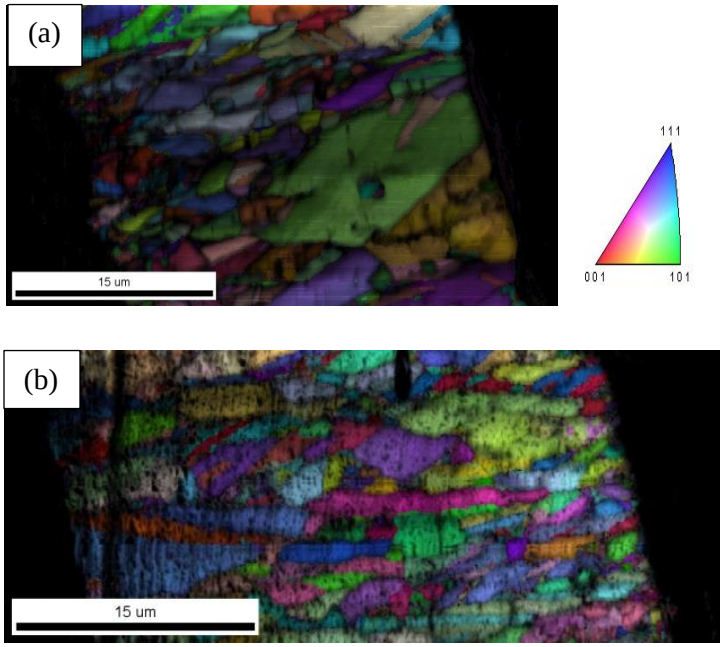

Figure 33. 3C-SiC grain orientation maps, IPF overlaid on IQ, for a) Dref, and b) D2000.

The IQ pattern is unique to the particular surface of examination. The black spot and left side line on D2000 is an artifact of the EBSD evaluation system. What appears to be an unusually large grain in D-ref is not uncommon to CVD coated SiC spherical

particles. A small number of larger grains have been found to be sparsely scattered throughout the material within a range of many smaller sized grains.

Both samples appear to have a random distribution of grain orientations. The grains in the annealed sample appear to be longer and thinner. Sample D2000 appears to be a compressed version of the reference sample.

The pole figures in Figure 34 indicate a weak texture of the material, meaning that the grain orientations as indicated by the randomly dispersed colored clusters do not show an orientation preference or special pattern. The annealing-induced increase in number of clusters with red coloring on the D2000 PF compared to the Dref PF indicates that more grains are contributing to the higher maximum density fields. More grains contributing to higher density area clusters, along with a significant decrease in the high maximum density value, would indicate a trend towards more uniformity in grain size with annealing. The maximum intensity values before and after annealing are 8.365 and 4.739, respectively. Such a difference indicates that the larger grains contributing to a higher intensity value have been diminished in size. Although in this scenario, such a distinct gap in values is most likely due to the one large grain caught in a randomly extracted sample, while the other randomly extracted sample had no outstanding, visually identifiable, larger grains.

One of the most significant differences between samples Dref and D2000 is the misorientation angle distribution as shown in Figure 35. The low angle boundary number fraction appears to increase a little over 20% with annealing while the high rotational angle boundary associated with CSL Σ3 appears to decrease about 10%.

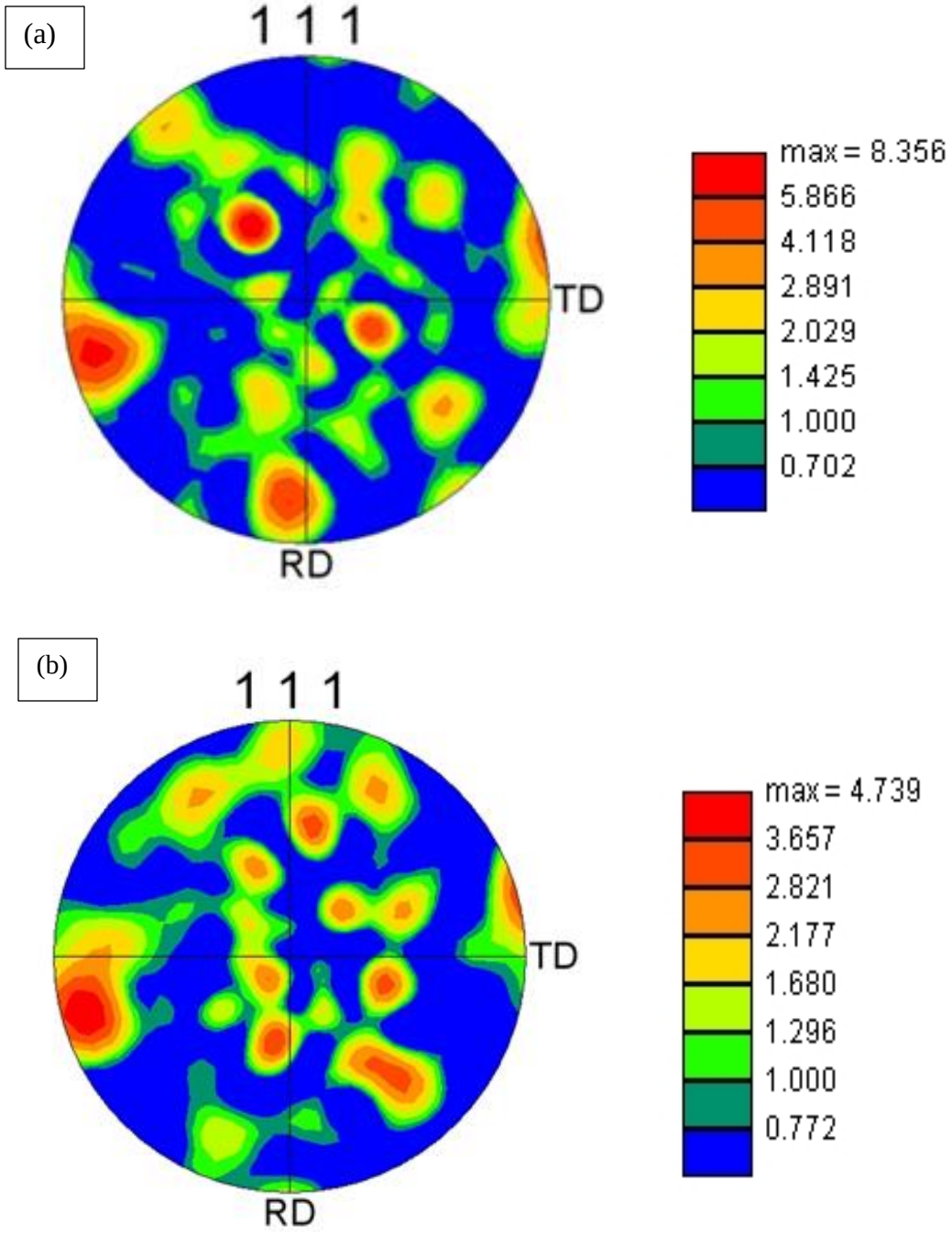

Figure 34. 3C-SiC pole figures for a) D-ref, and b) D2000, with corresponding legends.

Number fractions of other misorientation angles in D2000 are slightly lower than those of D-ref. The combination of these reductions in number fractions would account for the

higher increase in low angle boundaries compared to the lesser reduction in Σ3 boundaries.

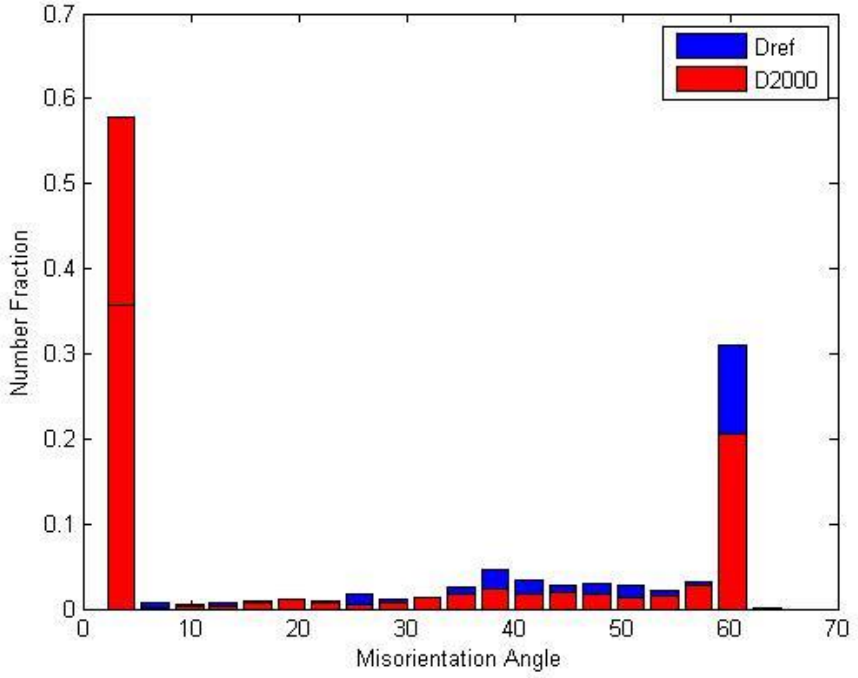

Figure 35. 3C-SiC Misorientation angle distribution comparison for samples D-ref and D2000.

The spatial layout of grain boundaries is of interest as it gives information regarding potential fission product migration pathways. Also, the visual display of grain boundary connectivity may be helpful in identifying links between microstructure and macroscopic properties of the material. Connectivity and GBCD, as defined in the last paragraph of section 2.C.2., play a dominant role in grain boundary engineering for the purpose of controlling bulk macroscopic properties. (Watanabe, 2011) Figure 36 displays the random rotational angle boundaries as well as the CSL boundaries for D-ref. Figure 37 provides a similar visual characterization of boundaries for D2000. The dark spots in Figures 36 and 37 indicate reduction of data within the partition as discussed in Section

3.D. The darkened areas most likely mark the location of 3C-SiC grains; however, it is highly probable the orientations of these points that did not make the CI> 0.10 cut off were indexed incorrectly. These points were rejected in order to get a more accurate boundary characterization.

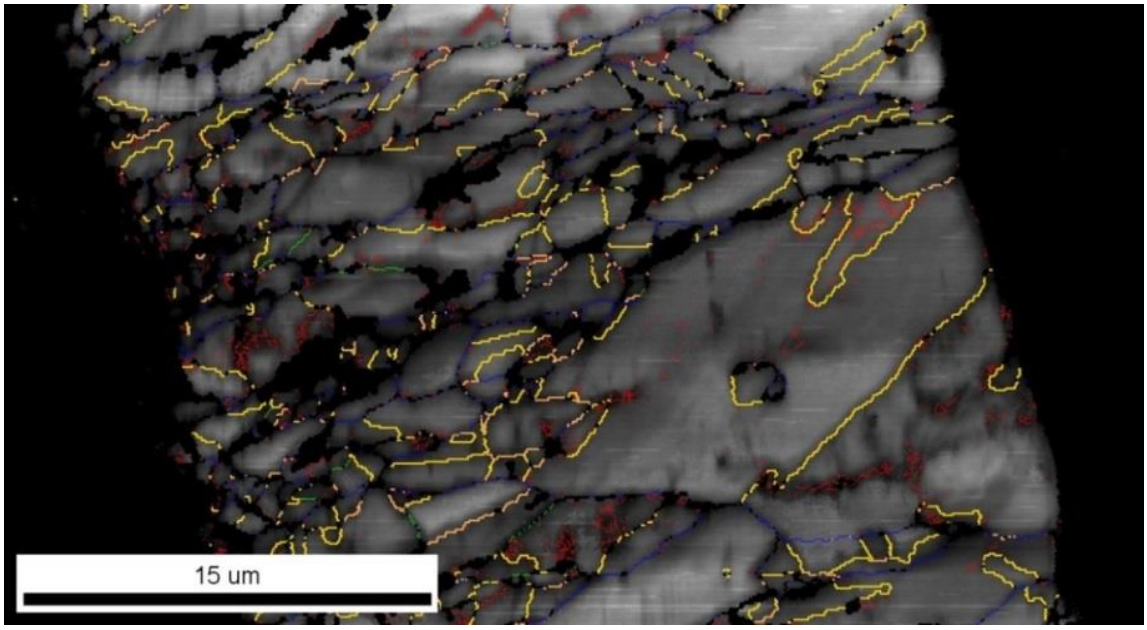

Boundaries: Rotation Angle

Min	Max	Fraction	Number	Length
2°	5°	0.356	4502	259.92 microns
5°	15°	0.020	253	14.61 microns
15°	180°	0.624	7883	455.13 microns

Boundaries: CSL

Sigma	Tolerance	Fraction	Volume	MDF Value	Number	Length
3	8.66	0.330	0.0176	18.79	4171	240.813 microns

Figure 36. 3C-SiC grain boundary rotational angle map with CSL boundaries for Dref.

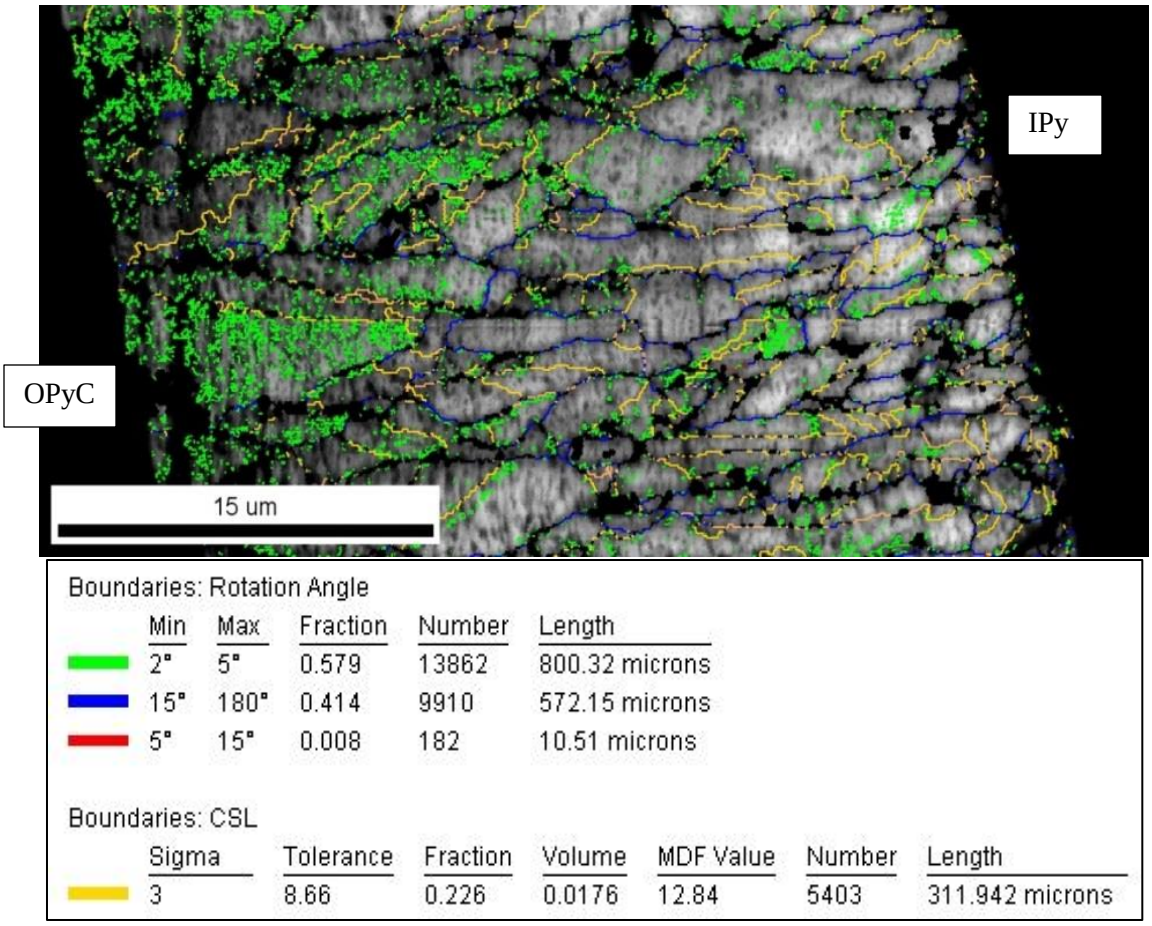

Figure 37. 3C-SiC grain boundary rotational angle map with CSL boundaries for D2000.

Note how several low angle boundaries are clustered near the OPyC layer in D2000. This unusually dense collection of low angle boundaries located in a specific region of the material does not appear to be the result of simply a rough surface due to inadequate polishing methods or SEM beam damage, which would leave a more uniformly distributed artifact across the entirety of the surface of analysis. It is possible that extreme annealing temperatures created internal forces that enhanced grain alignment, due to the spherical geometry of the coated material as well as size and shape of deposited grains, reducing the size of rotational angles between adjacent grains in the larger radii outer region of the SiC layer. If low angle boundaries slow the progress of

fission product migration, as some researchers have proposed (Lopez-Honorato, 2011), then the annealing process on Batch D particles is worth further investigation as it appears to have potential for the creation of a fission product migration bottleneck or seal. Although D2000 displays several higher angle boundary radial pathways between IPyC and OPyC compared to D-ref, it is not clear that these radial pathways are continuous near the OPyC boundary.

The default OIM grain boundary map categorizes grain boundaries into three rotational angle boundary subsets; 2-5 degrees (Σ1 boundaries), 5-15 degrees (low angle random rotational), and 15-180 degrees (high angle random rotational). Since CSL boundaries are thought to have special properties, it is of interest to see where they are connected. The CSL boundaries are highlighted in gold in the grain boundary maps of Figures 34 and 35. These boundaries are a subcategory of the high rotational angle boundaries, the remaining of which are marked in blue. Grain boundaries are colored by category according to the legend displayed below the maps in Figures 36 and 37.

CSL boundaries seem to be randomly distributed throughout the both samples. About 1/3 of the high rotational angle boundaries of D-ref can be classified as Σ3. A little less than ¼ of the high rotational angle boundaries of D2000 can be classified as Σ3. The significant difference in quantity of these special boundaries would suggest that the annealing process is not favorable with respect to preserving the desired CSL structure for Batch D.

The difference in grain boundary categorization is shown in the comparison of GBCD histograms for D-ref and D2000 in Figure 38. The default GBCD chart generated by

OIM has two separate categories for random angle boundaries, high and low, and one category for CSL boundaries as shown in the horizontal axis label in Figure 38.

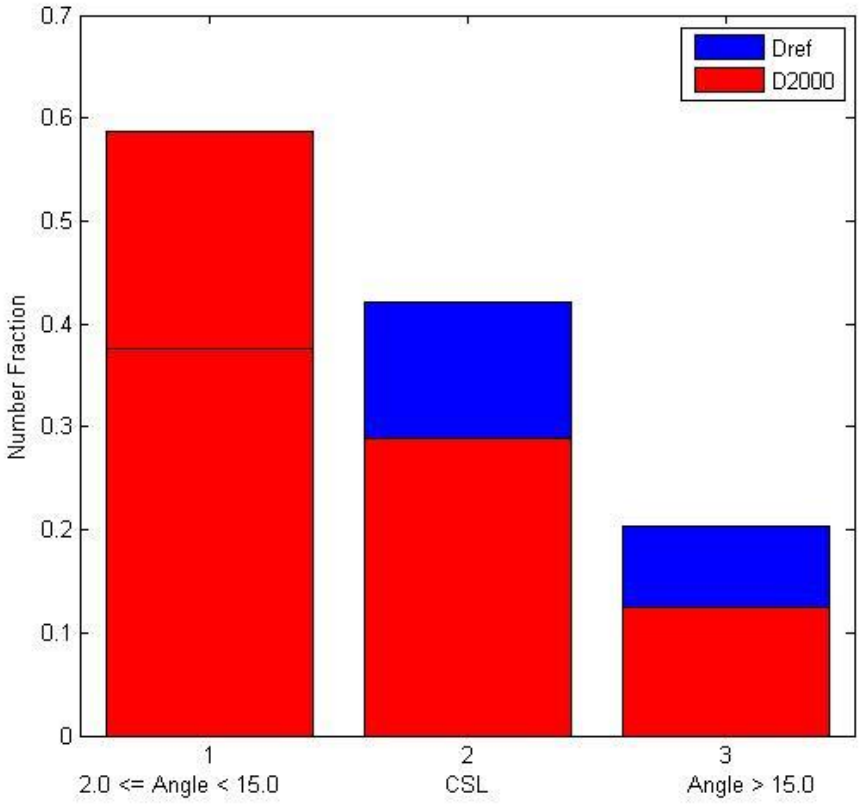

Figure 38. 3C-SiC grain boundary character distribution comparison for D-ref and D2000.

The apparent annealing-induced increase in low angle boundaries seems to come at a significant cost to CSL boundaries, but favorable reduction in the random high rotational angle boundaries believed to better facilitate fission product transport would likely be beneficial.

Figure 39 charts grain size categories and their respective area fraction occupancies for the given samples. Both D-ref and D2000 samples have a larger single grain category that stands apart, and a cluster of smaller grains of various sizes within a similar range. D2000 appears to be a compacted version of D-ref in Figure 39. The

smallest grain size category seems to diminish with annealing which would be another indication of a trend towards grain size uniformity.

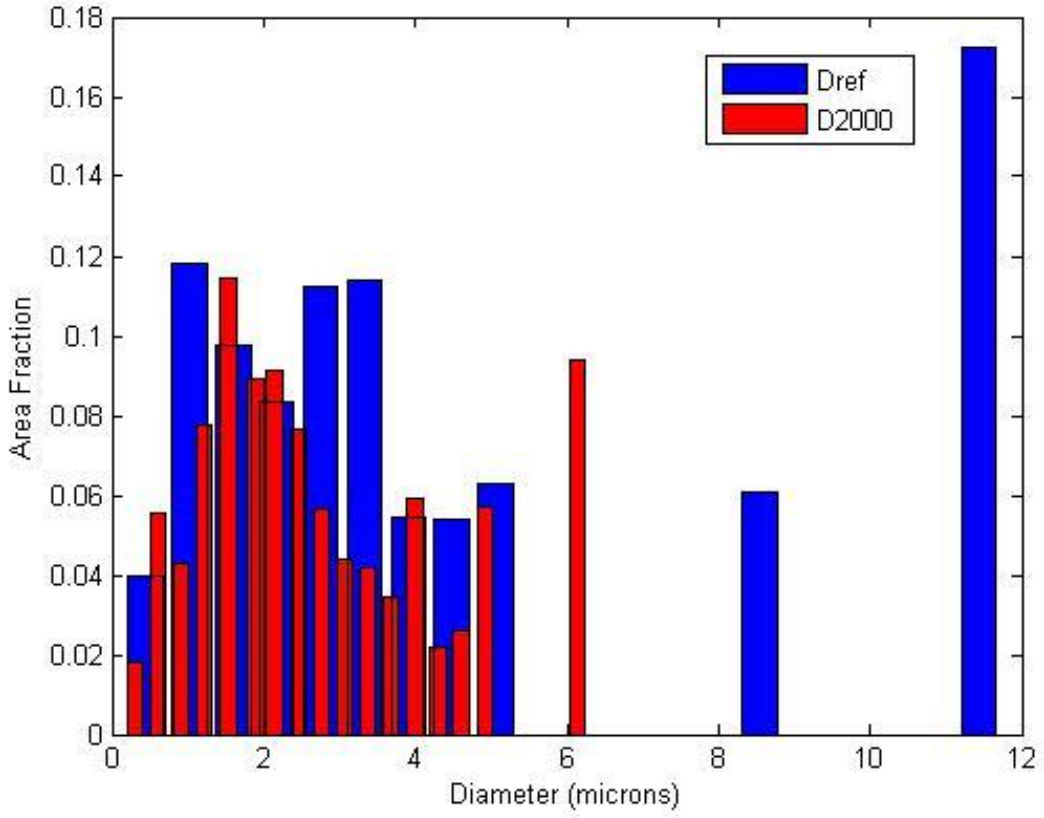

Figure 39. 3C-SiC grain size distribution comparison, grain diameter vs. area fraction, of D-ref and D2000.

Figure 40 shows a diameter vs. number fraction comparison between the two Batch D particles. D-ref and D2000 grain size average diameters were found to be 1.03μm and 0.95μm, respectively. The D-ref derived grain size is within close range, within one standard deviation, of the average grain size of 1.158μm found for a D-ref sample in a prior EBSD study (van Rooyen, 2010), giving supportive evidence that the EBSD analysis conducted in this study is reliable and that randomly extracted samples

are representative of the whole material fabricated under specified conditions. See Table 10 in section 4.B for grain diameter statistics for all samples in this study.

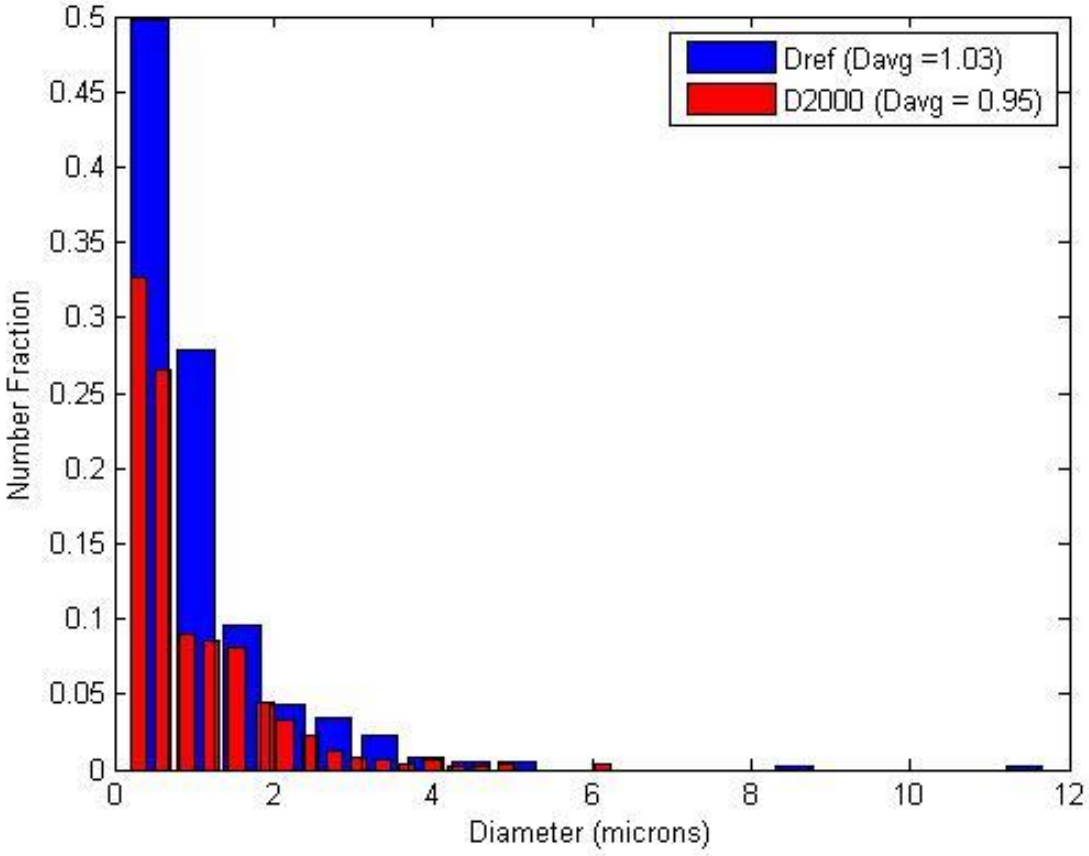

Figure 40. 3C-SiC grain size distribution comparison, grain diameter vs. number fraction, of D-ref and D2000.

Figure 41 illustrates the difference in CSL Σ3 boundaries between the two Batch D samples. This difference is in harmony with the change in misorientation angles as shown in Figure 35.

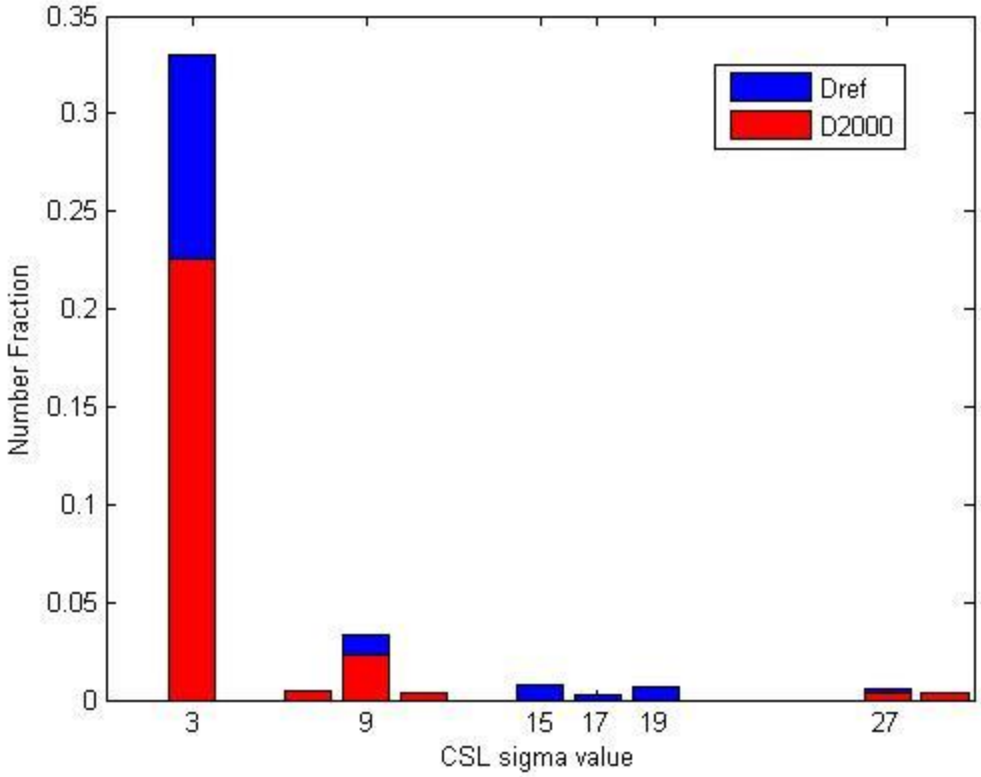

Figure 41. 3C-SiC CSL Comparison between D-ref and D2000.

In previous studies conducted by van Rooyen et al. (2012), a correlation identified between the grain sizes of Batch D and E samples and their corresponding hardness or characteristic strength was identified as shown in Figures 40 and 41, respectively. A much larger average grain size is reported in these figures from the previous study compared to the average grain sizes found in this study. This difference is due to resolution limitations of the human eye in relation to the Heyns Lineal Intercept Method used by van Rooyen et al., compared to resolution limits in relation to EBSD used in this study to find the average grain size. (van Rooyen, 2012) Relative increases and decreases are sufficient for comparison. Note how an annealing-induced decrease in grain size trends towards increased hardness. The annealing treatment for a Batch D sample in this study led to both a decrease in grain size and an increase in

Σ1 boundaries. The abundance of Σ1 boundaries may account for Batch D's elevated hardness above that measured for Batch E samples as shown in Figure 40.

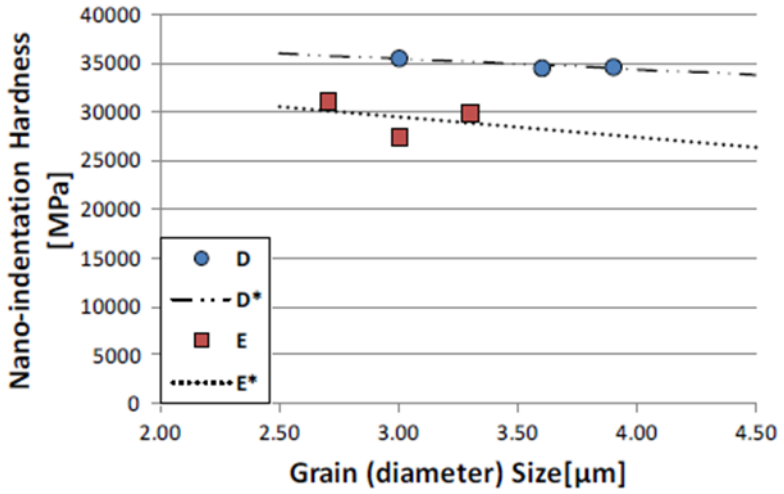

Figure 42. 3C-SiC prior study hardness comparison between Batches D and E. (van Rooyen, 2012)

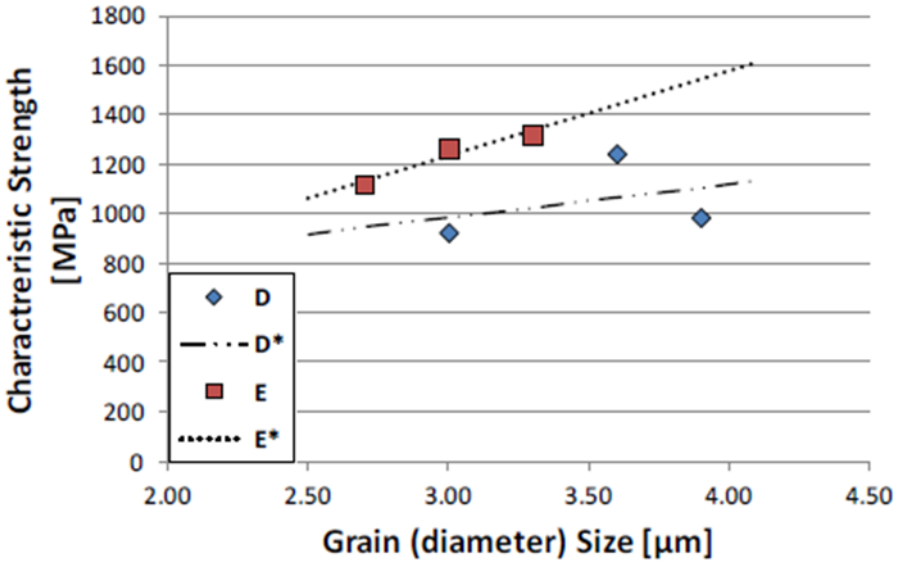

Figure 43. 3C-SiC Prior study characteristic strength comparison between Batches D and E. (van Rooyen, 2012)

The characteristic strength of samples from Batches D and E appears to decrease with decreasing grain size in Figure 41. Likewise, Σ3 CSL boundaries appear to decrease along with

the decrease in average grain size in this study. A correlation may exist between the characteristic strength of the SiC TRISO layer, and the abundance of Σ3 CSL boundaries.

Table 4 summarizes data for comparison of these samples. Grain orientation data is pulled from PF maps. The number of max regions refers to the PF contour plots containing dark orange or red coloring. Grain boundary character data lists the number fractions associated with the chart bars displayed in Figure 36. Note the apparent increase in grain boundary length with annealing at 2000˚C. This increase serves as another indication that the average grain size decreases due to annealing.

Table 4. 3C-SiC Grain and Grain Boundary Data Comparison Chart for Batch D samples.

Characteristic	Dref			D2000		
Grain Size Distribution	Range		Average	Range		Average
	Min.	Max.	Diameter	Min.	Max.	Diameter
	(µm)	(µm)	(µm)	(µm)	(µm)	(µm)
	0.497093	11.4321	1.03	0.302214	6.1432	0.95
Grain Orientation	Density	Number		Density	Number	
	Maximum	Max. Regions		Maximum	Max. Regions	
	8.356	6		4.739	11	
Misorientation	Low Angle	60 ˚ Angle		Low Angle	60 ˚ Angle	
	# Fraction	# Fraction		# Fraction	# Fraction	
	0.356227	0.309701		0.578734	0.205895	
CSL	Σ3	Total		Σ3	Total	
	# Fraction	# Fraction		# Fraction	# Fraction	
	0.33	0.421		0.23	0.289	
Grain Boundary Character	Low (2˚-15˚)	CSL	High (15˚-180˚)	Low (2˚-15˚)	CSL	High (15˚-180˚)
	0.376246	0.420953	0.202801	0.58629	0.289221	0.124489
Total Length /Sample Points	0.01008 µm / point			0.018527 µm / point		

It is desirable to obtain a high concentration of β-SiC for irradiation applications. (Kirchhofer, 2013) Therefore, it is of interest to determine the relative presence of α-SiC which consists of all polytypes except 3C-SiC. 6H-SiC is one of the more abundant polytypes found in CVD coated SiC although usually as a result of higher deposition temperatures than those used for fabrication of the SiC layer in the TRISO particle. (Snead, 2007) Trace amounts of 6H-SiC have been reported found by transmission

electron microscopy (TEM) in a CVD coated SiC TRISO layer under study by Helary et al.; however, the grains were too small to be detected by EBSD. (Tan, 2008) EBSD can readily distinguish between the cubic and hexagonal phases, if the image quality is sufficiently sharp. The difficulty encountered is the correct indexing of orientation. (Dingley, 2009) Scan results, nevertheless, give some indication of over indexing of the 6H-SiC phase. Figures 44 and 45 show IPF maps for the 6H-SiC D-ref scan and the 6H-SiC D2000 scan, respectively. The indexed points shown in color would seem to indicate a substantial abundance of the polytype which is inconsistent with prior studies. Several dots cover the map, yet they are scattered to the extent that they do not form solid, filled in shapes representing grains as is the case in the 3C-SiC scans. Indexed point patterns shown in Figures 44 and 45 are similar to IPF map indexed point patterns found in the pyrolytic carbon layer regions of prior unfiltered scans for the 3C-SiC phase. No SiC was expected in those regions. Similarly, the scattered index points found in the 6H-SiC maps may be merely the result of a low quality ceramic image. The larger clusters of similarly oriented points within designated grain regions identified by the IQ maps remaining after data filtering are evidence to support the possibility of some 6H-SiC presence scattered within the matrix. Further testing would be necessary to confirm the presence or absence of α-SiC and to determine the quantity within the sample.

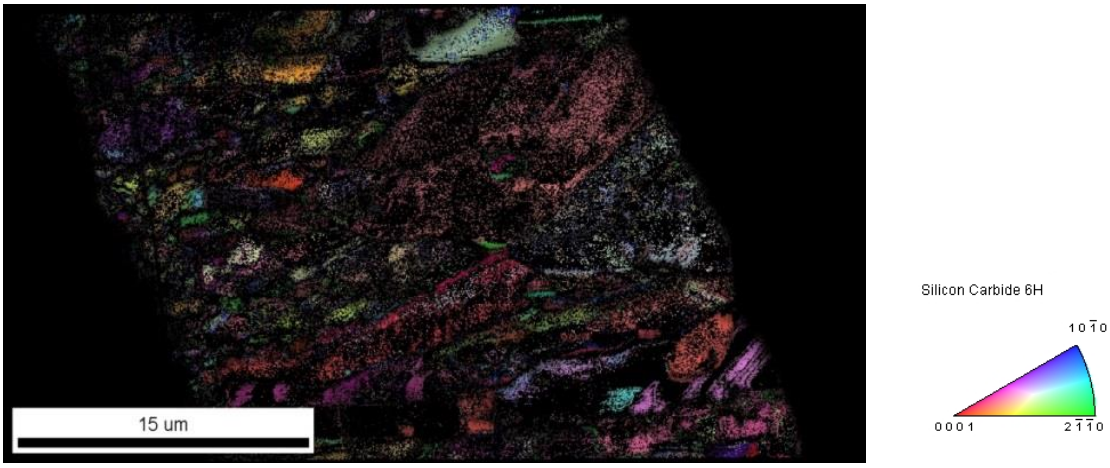

Figure 44. Inverse pole figure map for 6H-SiC scan of D-ref.

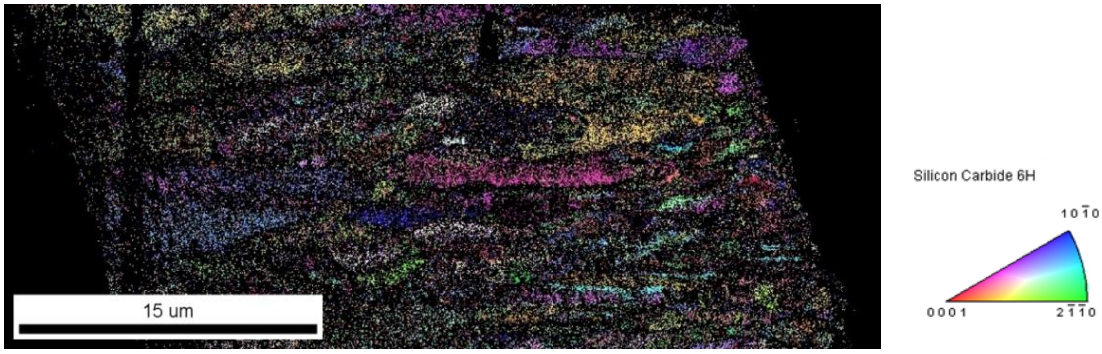

Figure 45. Inverse pole figure map for 6H-SiC scan for D2000

Data have been gathered for the 6H-SiC scan in a similar fashion to that of 3C-SiC as discussed in Section 3.D. Figures 44 and 45 display the results of a data partition consistent with the CI value limit in 3C-SiC scans, and is not intended to indicate proof of abundant α-SiC. In addition, 6H-SiC is expected to be scattered throughout the matrix; therefore, boundary analysis is meaningless.

The D-ref pole figure displayed in Figure 46(a) indicates a preferred orientation perpendicular to the sample surface, yet a random presence is observed in the lower intensity density scale. The D2000 pole figure displayed in Figure 46(b) seems to indicate

that heat treatment reduces the size of any 6H-SiC grains present, and that they become more random in their orientation. The maximum density category appears to drop nearly to half the pre-annealing value, which gives the indication that grains are smaller. The dark orange-red clusters are no longer near the center in Figure 44(b), indicating a more random orientation.

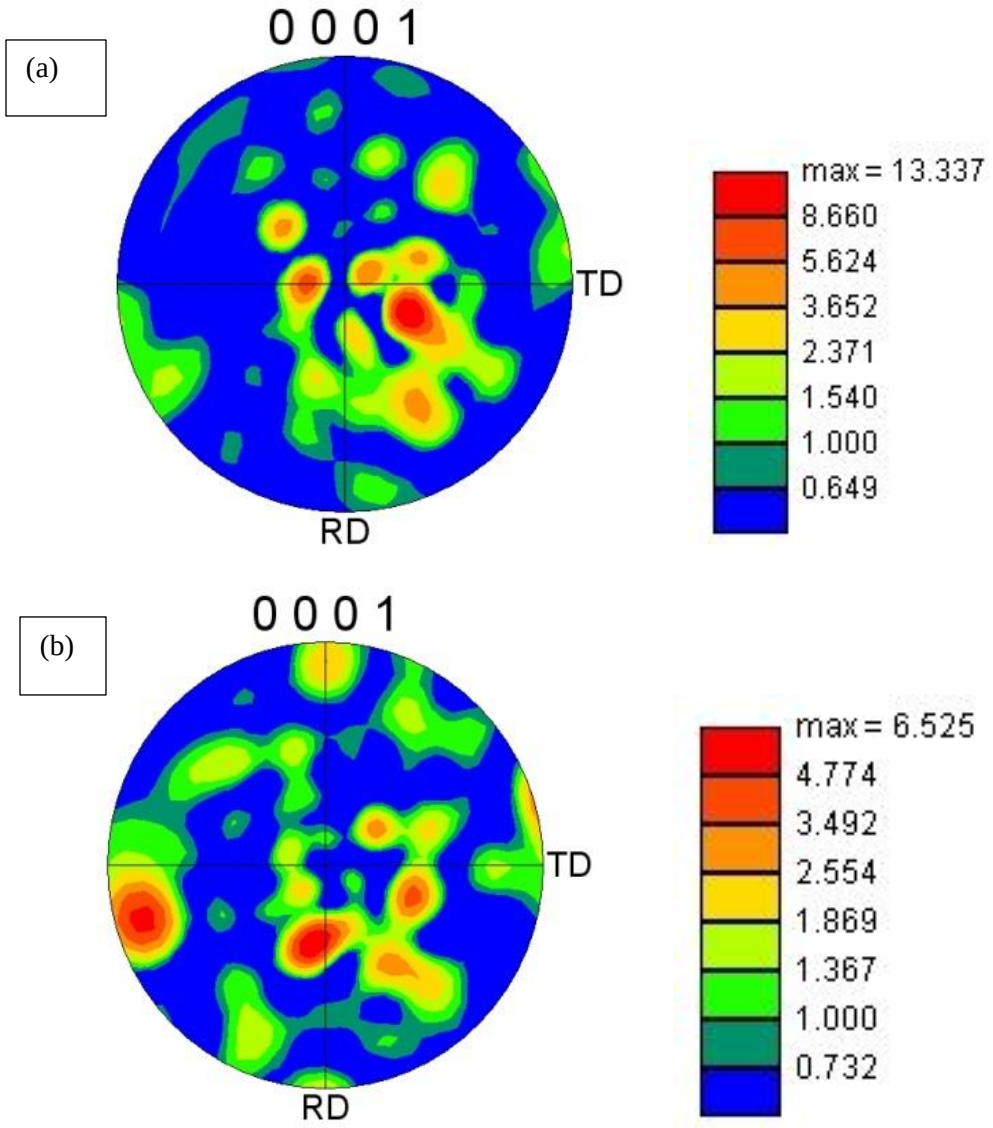

Figure 46. Pole figures for a) D-ref 6H-SiC scan, and b) D2000 6H-SiC scan.

Figure 47 provides a comparison of grain size and area fraction of the scanned surfaces. The similar distribution pattern of the pre- and post-annealing samples would indicate that analysis on similar materials has been conducted. The difference in grain diameter categories, wherein the smallest category is higher for the annealed sample while all other categories are smaller, would indicate that heat treatment reduces the sizes of less desirable 6H-SiC grains.

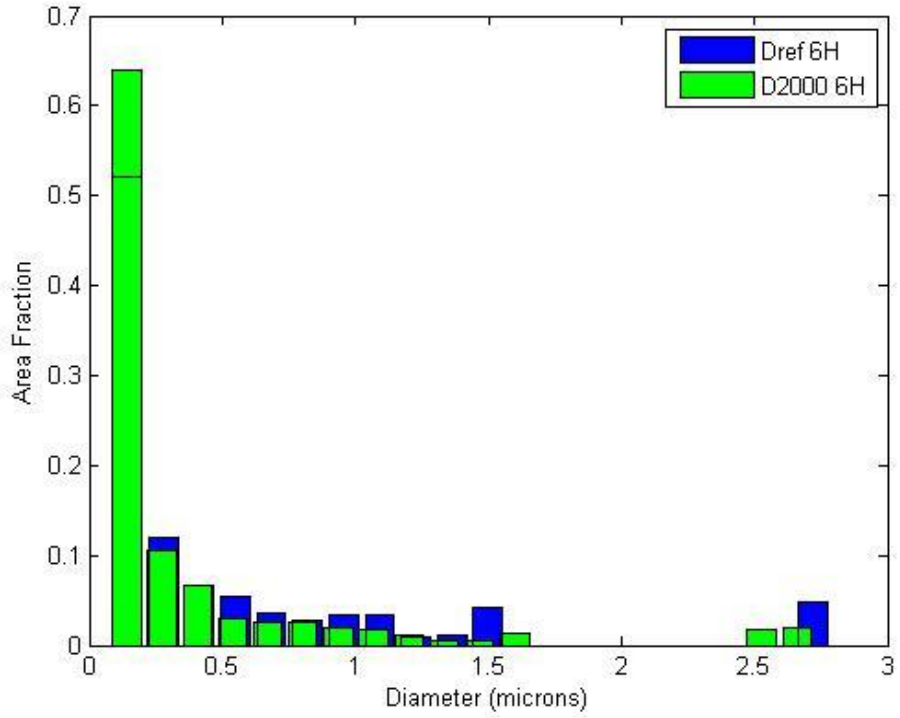

Figure 47. EBSD 6H-SiC scan grain diameter vs. area fraction comparison between D-ref and D2000 samples.

Tables 5 and 5 indicate partition parameters used to filter unwanted data. Partition parameters were chosen for reasons discussed in Sec. 3D. Points of an IQ < 500 and CI < 0.10 were filtered out for D-ref 3C-SiC and 6H-SiC scans. This filtering led to a partition wherein all points analyzed were good, or rather, indexed points.

Table 5. D-ref 3C-SiC and 6H-SiC Scan Data Collection Statistics

Sample	Step Size (nm)	Clean Up Methods	Partition Parameters		Total Points	Good Points	Point Fraction	Averages		
			IQ	CI				IQ	CI	Fit
Dref (3C-SiC)	100	Raw Data	*	*	278240	200688	1	3337.91	0.11	1.78
Dref (3C-SiC)	100	Neighbor Orientation Correlation Grain CI Standardization Grain Fit Standardization (cropped)	*	*	110748	103223	1	1127.73	0.4	1.24
Dref (3C-SiC)	100	Neighbor Orientation Correlation Grain CI Standardization Grain Fit Standardization (cropped)	> 500	*	88368	88247	0.798	1261.71	0.46	1.12
Dref (3C-SiC)	100	Neighbor Orientation Correlation Grain CI Standardization Grain Fit Standardization (cropped)	> 500	> 0.10	72394	72394	0.654	1350.59	0.56	0.94
Dref(6H-SiC)	50	Raw Data	*	*	469128	362494	1	1480.87	0.08	1.21
Dref(6H-SiC)	50	cropped	> 500	> 0.10	82986	82986	0.228	1647.56	0.23	1.09

Table 6. D2000 3C-SiC and 6H-SiC Scan Data Collection Statistics

Sample	Step Size (nm)	Clean Up Methods	Partition Parameters		Total Points	Good Points	Point Fraction	Averages		
			IQ	CI				IQ	CI	Fit
D2000(3C-SiC)	100	Raw Data	*	*	164625	135328	1	961.87	0.39	1.79
D2000 (3C-SiC)	100	Neighbor Orientation Correlation								
		Grain CI Standardization	> 400	*	75985	75797	0.792	1139.95	0.45	1.18
		Grain Fit Standardization (cropped)								
D2000 (3C-SiC)		Neighbor Orientation Correlation								
		Grain CI Standardization	> 400	> 0.10	74647	74647	0.69	1190.71	0.53	1.05
		Grain Fit Standardization (cropped)								
D2000 (6H-SiC)	50	Raw Data	*	*	397245	326561	1	642.07	0.07	1.52
D2000 (6H-SiC)	50	cropped	>350	>0.1	57115	57115	0.181	749.78	0.23	1.32

The average IQ, CI, and Fit values all increased for the data partition. It is interesting to note that for both D-ref and D2000, the fraction of points in the partition for the two phases are within reasonable bounds of separation, meaning that the fraction of points remaining after the partition is applied for each phase sums to less than 100% of the total points evaluated. For example, the D-ref 3C-SiC point fraction within the partition is 65.4% and the D-ref 6H-SiC remaining point fraction is 22.8%. These values sum to 88.2%, leaving a buffer of approximately 12% for the surrounding pyrolytic carbon layers, low image quality boundary points, and discarded 3C-SiC low image quality points. D2000 data (in Table 6) indicate a 69% 3C-SiC good point fraction, and an 18% good point fraction for 6H-SiC, leaving a 13% buffer. Such a separation of quantities gives some indication that OIM can distinguish between the two phases.

Uncertainties in the actual quantities present, based on the inherent difficulties encountered in an attempt to obtain high quality or sharp images from ceramic samples, lead to a focus on differences in data acquired through a consistently applied analysis method. It may not be clear how much 6H-SiC is present, or if it is present at all, yet differences between what has been labeled 6H-SiC in each sample is of interest. Consistency in applied partitioning resulted in a notable difference of about 4% in 6H-SiC good point remaining fractions in samples D-ref and D2000. It appears that the annealing process may reduce the presence of α-SiC.

4. A.2 Batch E: No Annealing vs. Annealing at 2000 ˚C for 30 minutes

Similar to D-ref and D2000 data comparison, an OIM data partition was created for E-ref and E2000 with parameters thought to best enhance the quality of the data being analyzed without sacrifice of much useful information. The reason for choosing these

particular parameters is discussed in Section 3.D. Tables 7 and 8 list the chosen IQ and CI parameters along with the percentage of remaining points and partition IQ, CI, and Fit averages. These average values become more favorable upon application of the data partition.

Table 7. E-ref 3C-SiC and 6H–SiC Scan Data Collection Statistics

Sample	Step Size (nm)	Clean Up Methods	Partition Parameters		Total Points	Good Points	Point Fraction	Averages		
			IQ	CI				IQ	CI	Fit
Eref (3C-SiC)	100	Raw Data	*	*	168311	167156	1	1768.95	0.17	1.67
Eref (3C-SiC)	100	Neighbor Orientation Correlation	*	*	121662	108974	1	1880.33	0.51	1.08
		Grain Ci Standardization								
		Grain Fit Standardization (cropped)								
Eref (3C-SiC)	100	Neighbor Orientation Correlation	>500	> 0.10	84815	84815	0.697	2208.57	0.65	0.79
		Grain Ci Standardization								
		Grain Fit Standardization (cropped)								
Eref (6H-SiC)	75	Raw Data	*	*	204626	167005	1	827.44	0.06	1.54
Eref (6H-SiC)	75	Cropped	>350	> 0.10	17893	17893	0.24	1065.04	0.23	1.21

Table 8. E2000 3C-SiC Scan Data Collection Statistics

Sample	Step Size (nm)	Clean Up Methods	Partition Parameters		Total Points	Good Points	Point Fraction	Averages		
			IQ	CI				IQ	CI	Fit
E2000 (3C-SiC)	100	Raw Data	*	*	87509	81693	1	1509.64	0.19	1.65
E2000 (3C-SiC)	100	Neighbor Orientation Correlation Grain Ci Standardization Grain Fit Standardization (cropped)	*	*	59613	59190	1	1716.58	0.6	1.08
E2000 (3C-SiC)	100	Neighbor Orientation Correlation Grain Ci Standardization Grain Fit Standardization (cropped)	>450	> 0.10	50917	50917	0.854	1861.8	0.69	0.93

Figures 48 and 49 display the surface grains with their variety of orientations depicted by their IPF color coding overlaid on the sample IQ pattern. The overall image quality of these samples is better than those for the Batch D samples. E-ref and E2000 scans provide clear patterns for the easy identification of the IPyC interface side (left) and the OPyC interface side (right) of the SiC layers. The grains are progressively larger in the radially outward direction, and the OPyC layer has a crisper edge.

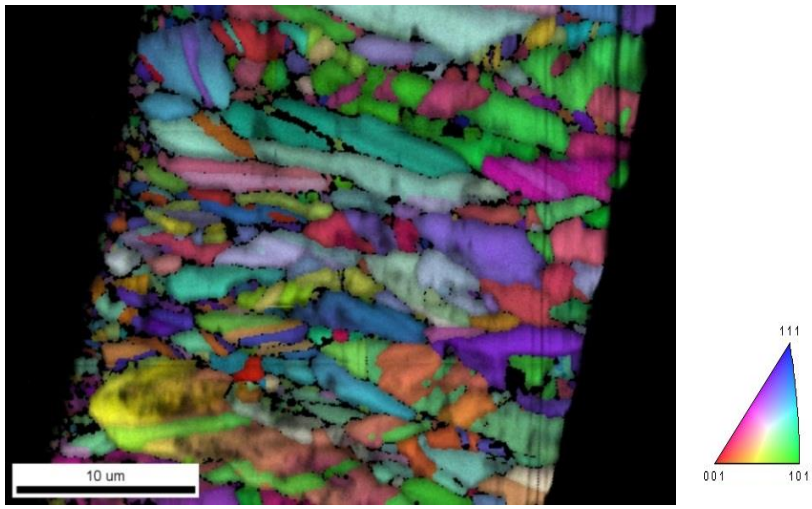

Figure 48. Inverse pole figure overlaid on IQ pattern for 3C-SiC scan of E-ref.

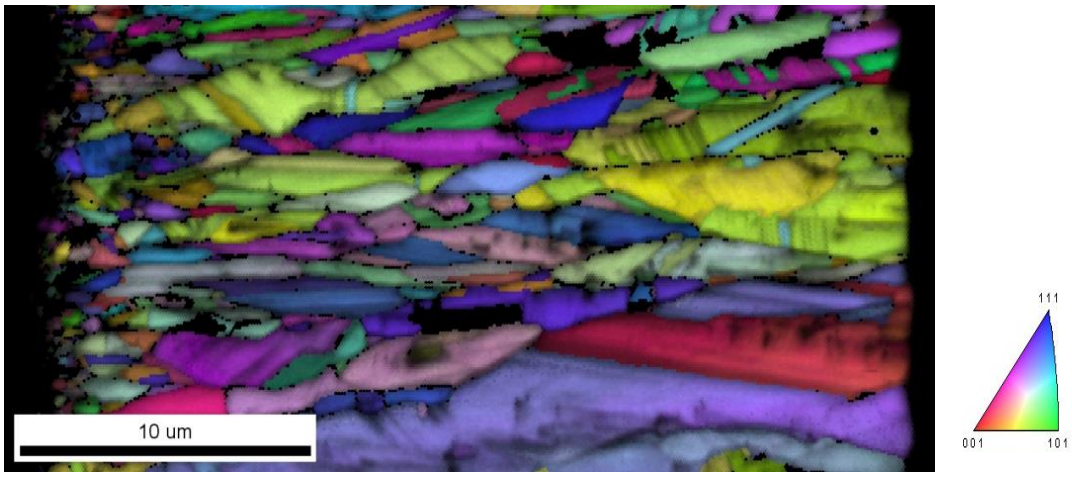

Figure 49. Inverse pole figure overlaid on IQ pattern for 3C-SiC scan of E2000.

Grain orientations seem to be fairly random and the annealed sample appears to have more compact grains.

The pole figures shown in Figure 50 both illustrate a weak texture. In contrast to the pole figures representing samples from the Batch D, the annealed Batch E sample has a higher maximum density than E-ref. In this case the annealed sample extraction caught grains in the larger size category; whereas, the E-ref extraction did not.

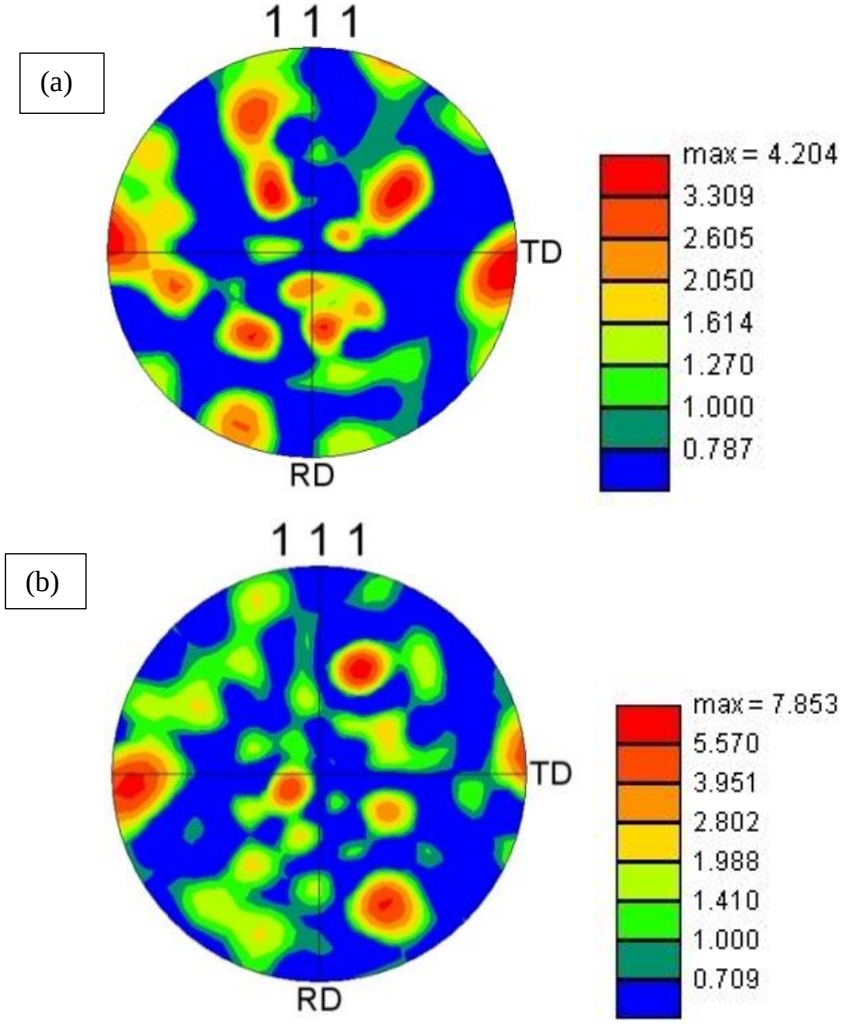

Figure 50. 3C- SiC pole figures for a) E-ref, and b) E2000.

Sample extractions for Batch D resulted in the opposite phenomenon. The maximum intensities for Batch E samples differ significantly, with the value for the annealed sample at almost double that of the reference sample.

Figure 51 displays the comparison of misorientation angle distributions for E-ref and E2000. It appears that both the low angle misorientation and the sixty degree angle misorientation categories decrease in number fraction due to annealing, while almost all other angle category number fractions increase. Annealing in this case does not appear to be favorable regarding the structure of grain boundaries.

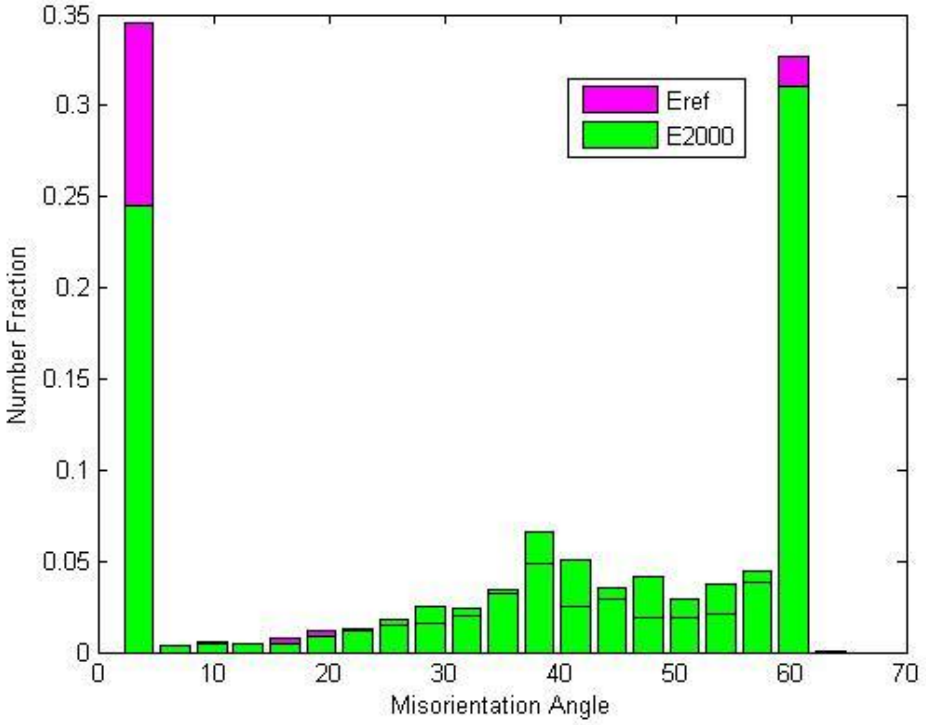

Figure 51. 3C- SiC misorientation angle comparison of samples E-ref and E2000

Figures 52 and 53 display the connectivity of grain boundaries as well as their color coded rotation angle categorization for E-ref and E2000, respectively. CSL

boundaries highlighted in gold appear to be randomly distributed throughout the E-ref and E2000 material. The CSL boundaries are desirable; however, high angle random rotational boundaries clearly marked blue form several radial pathways between the IPyC and OPyC layers that are expected to facilitate fission product migration. The abundance of CSL boundaries that do appear may serve to maintain the material characteristic strength during exposure to extreme high temperatures and at a level above that of Batch D samples as shown in Figure 41 in the previous section.

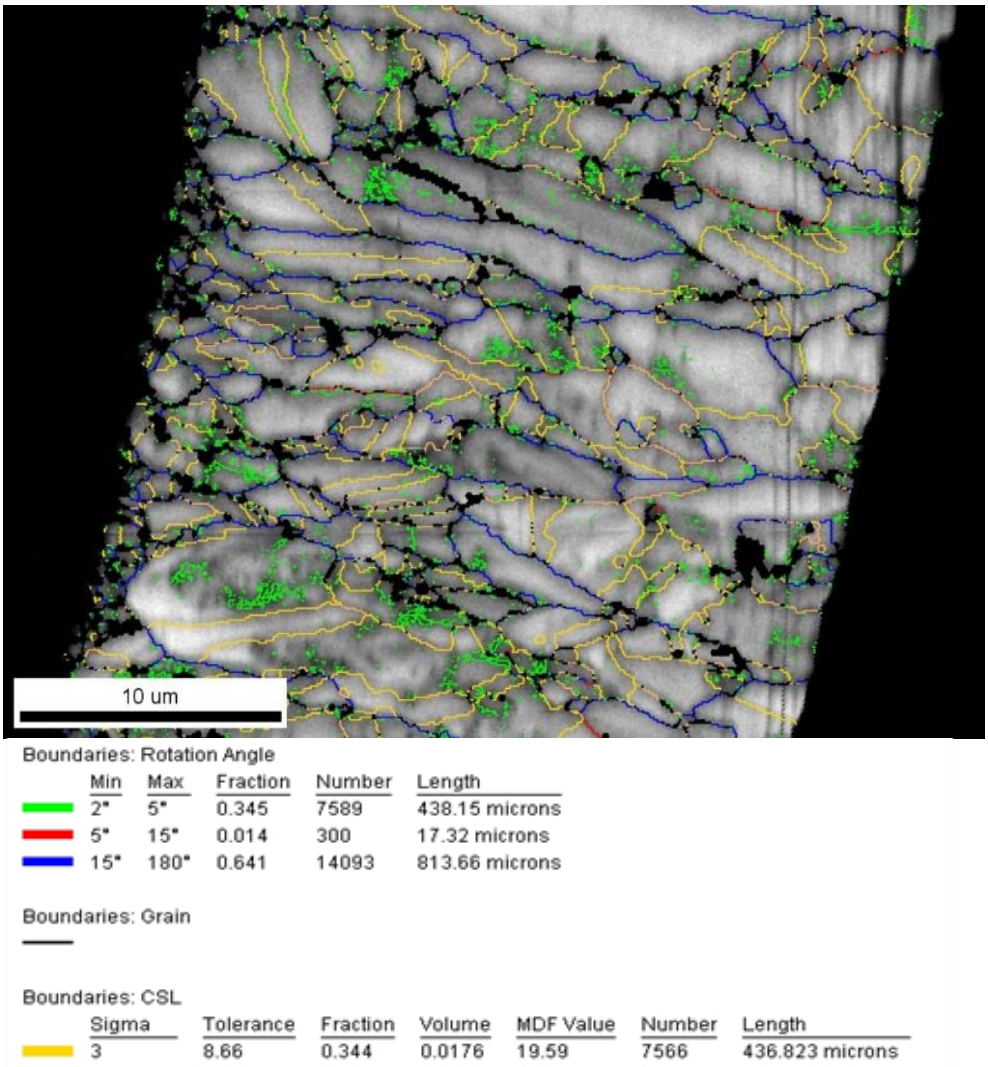

Figure 52. 3C-SiC rotational angle boundary map including CSL boundaries for E-ref

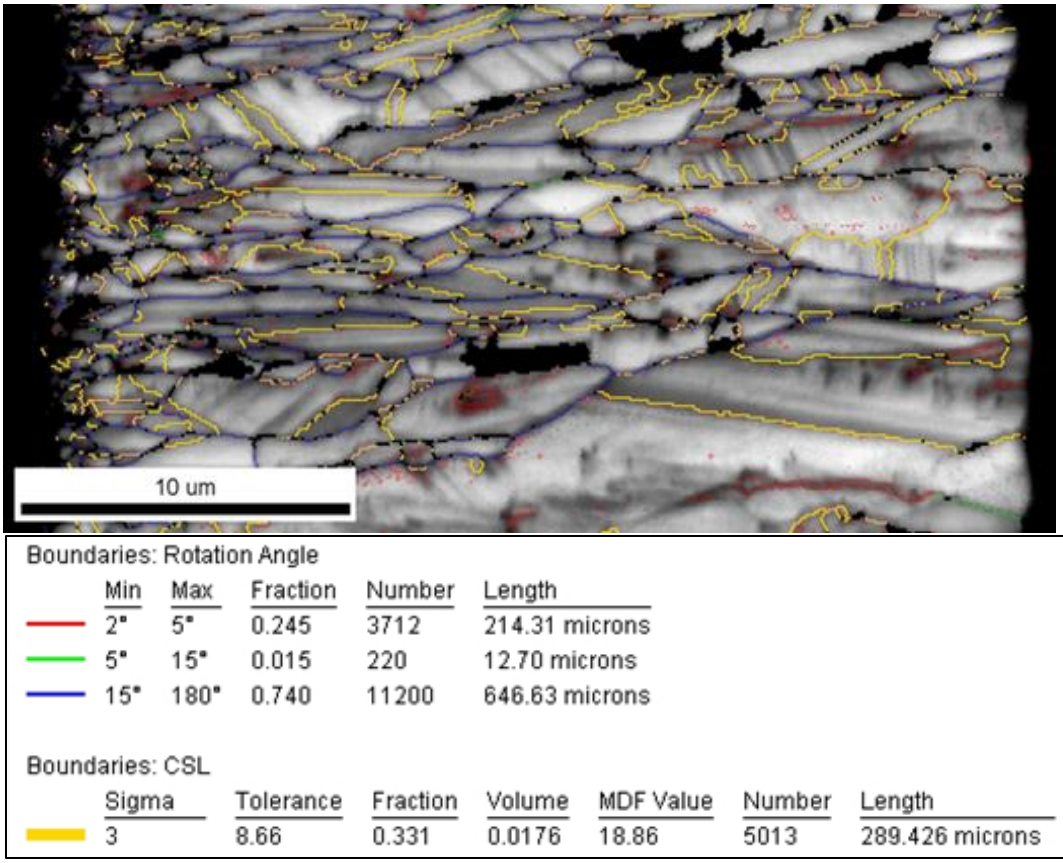

Figure 53. 3C-SiC rotational angle boundary map including CSL boundaries for E2000

The SiC grains appear to be more tightly packed and elongated after annealing, leaving a higher concentration of radial pathways between pyrolytic carbon layers. This directional abundance along with elongated columnar grains may be the reason for apparent reduction in characteristic strength with decreasing grain size as also shown in Figure 41. Such a structure might be more susceptable to a form of buckling when compressive forces are applied than it would be if it were a more net-like grain boundary structure such as that displayed for the B1600 sample observed to have greater material strength (van Rooyen, 2012) than most of the other batches in the overall study. The apparently tighter packing, indicating an increase of material density, may explain the increase in hardness in relation to decreasing grain size as shown in Figure 40 of the

previous section.

Figure 54 shows the differences in grain boundary character distribution between the reference and the annealed sample.

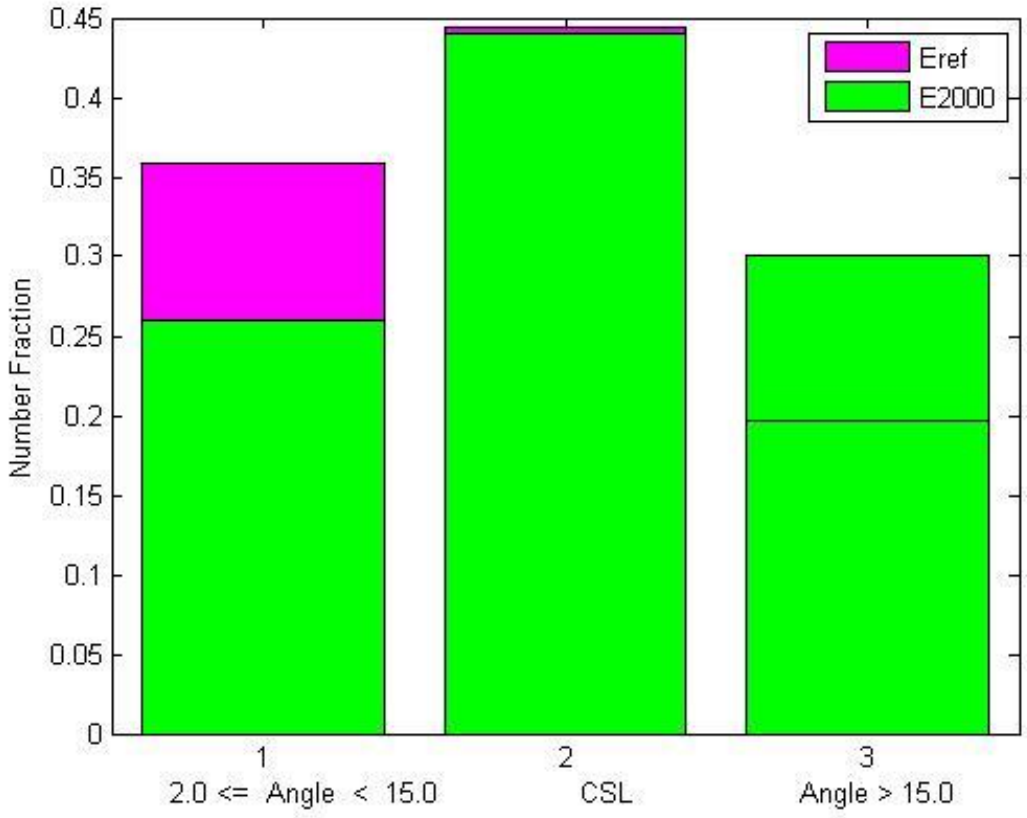

Figure 54. 3C- SiC grain boundary character distribution comparison of E-ref and E2000.

The data collected from these samples would indicate a trend towards a significant reduction in low angle boundaries with annealing and not much change in CSL boundaries. Low angle boundary number fraction decrease with higher angle boundary number fraction increase is opposite to the results obtained for Batch D samples. It was postulated in the prior section that the combination of spherical layer

geometry, grain shape, and size given in the D-ref batch might facilitate internal forces sufficient to force grains in the outer regions of the SiC layer to move towards alignment when exposed to extremely high temperatures. Perhaps grains with higher concentrations of CSL boundaries are more resistant to such a process or movement. The higher percentage of CSL boundaries in E-ref combined with initially smaller grains might instead create an environment wherein previously low rotational angles increase enough to be categorized in the high rotational angle bin upon exposure to extreme heat.

The higher deposition temperature of the SiC layer for Batch E particles may account for the smaller difference in CSL boundary number fractions between E-ref and E2000 compared to that of Batch D samples as the difference between deposition and annealing temperature is much less for Batch E particles. Batch E samples appear to maintain an elevated characteristic strength compared to Batch D samples as shown in the previous section in Figure 41. This may be due to the higher percentage of CSL boundaries in Batch E samples. Likewise, the reference Batch D sample has a larger percentage of low angle boundaries than the Batch E reference sample. Coincidentally, Figure 40 shows Batch D samples having a hardness consistently larger than that of Batch E samples. A correlation could exist between the hardness of a material and the number fraction of low angle boundaries.

From the grain size distribution vs. area fraction chart displayed in Figure 55 it appears that grain size categories shift from a single, more continuous spread of grain sizes to a wide gap between larger and smaller grain sizes upon annealing; however, it is also possible that the E2000 extracted sample contained a grain from a larger grain size category sparsely populating the SiC material while the E-ref extracted sample did not.

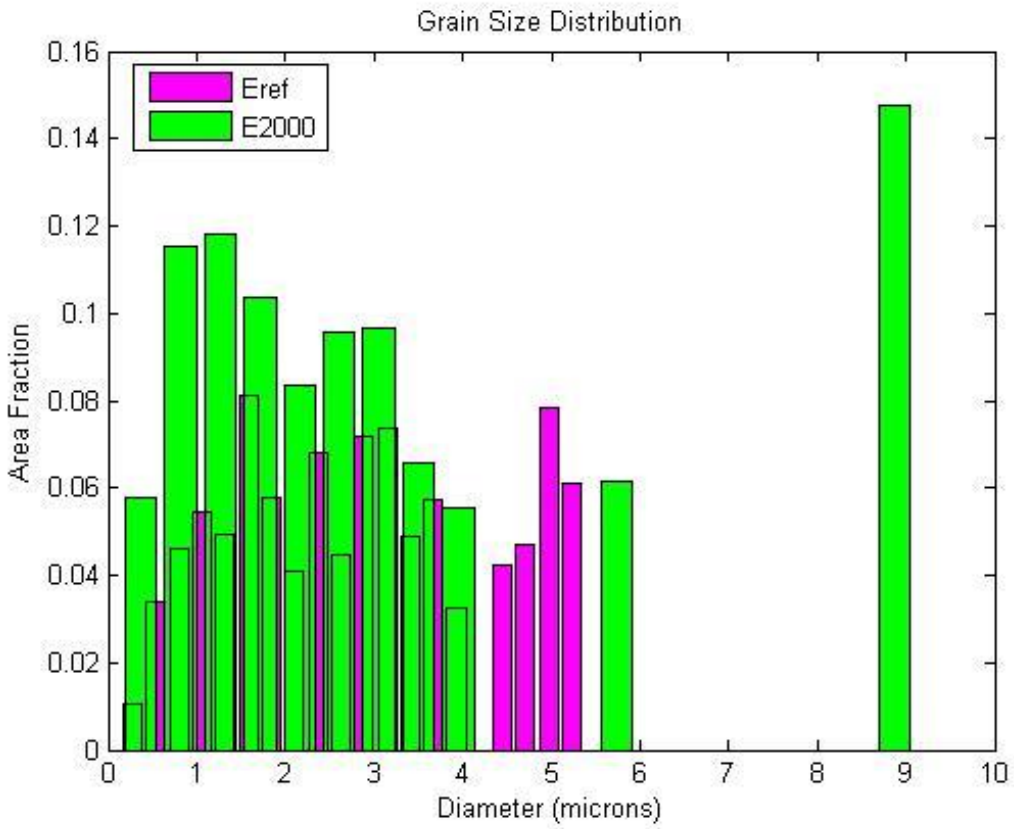

Figure 55. 3C-SiC grain size, diameter vs. area fraction, comparison of E-ref and E2000

Further inspection of the grain boundary maps in Figures 52 and 53 verify that the latter is the case. Figure 56 displays the associated grain size vs. number fraction distribution for Batch E samples wherein most of the smaller grain size categories appear to significantly increase with annealing.

Figure 57 shows the difference in number fractions for prominent CSL categories. Both Batch E samples have similar distributions. The largest difference is in the ∑3 boundaries. The annealing process appears to reduce the number fraction of these special boundaries; yet, the reduction is relatively small, about 2% by comparison for these samples.

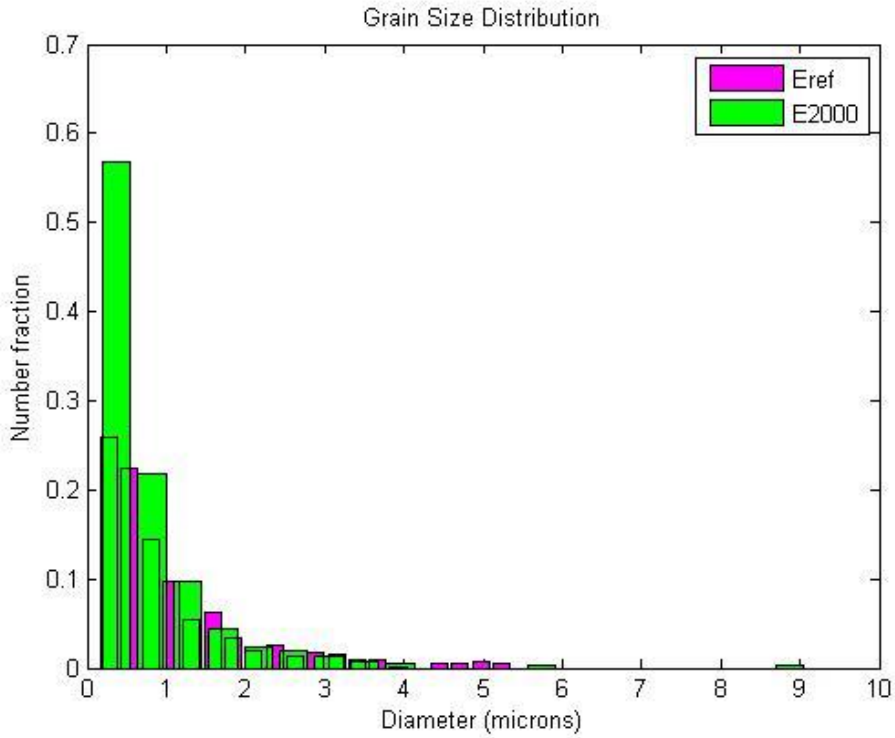

Figure 56. 3C-SiC grain diameter vs. number fraction comparison of Eref and E2000.

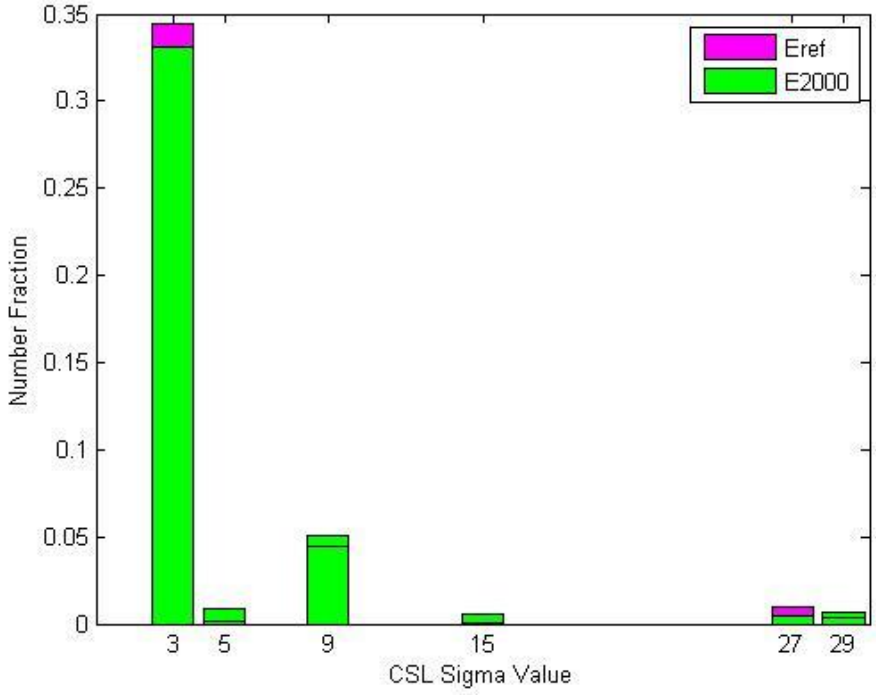

Figure 57. 3C-SiC comparison of CSL boundaries of samples Eref and E2000.

Grain and Grain boundary data collected for Batch E samples are summarized in Table 9 in a format similar as that used for Batch D samples in the previous section. Batch E sample data show a steeper drop in average diameter with annealing than that for Batch D samples. This larger difference would not be expected based on the nature of the specific samples extracted and anlayzed because grains in the larger category would more likely favor a smaller difference. The difference between measured boundary lengths (2.2nm/point) for Batch E samples is about 75% less than that for the Batch D samples. This difference is most likely due to the higher deposition temperature for Batch E samples, which would result in smaller grains and a larger percentage of grain boundaries initially present.

Table 9. 3C- SiC Grain and Grain Boundary Data Comparison Chart for Batch E Samples.

Characteristic	Eref			E2000		
Grain Size Distribution	Range		Average	Range		Average
	Min.	Max.	Diameter	Min.	Max.	Diameter
	(µm)	(µm)	(µm)	(µm)	(µm)	(µm)
	0.278855	5.23223	1.02	0.372154	8.87087	0.788
Grain Orientation	Density	Number		Density	Number	
	Maximum	Max. Regions		Maximum	Max. Regions	
	4.204	13		7.853	6	
Misorientation	Low Angle	60 ° Angle		Low Angle	60 ° Angle	
	# Fraction	# Fraction		# Fraction	# Fraction	
	0.345373	0.326722		0.245308	0.310798	
CSL	Σ3	Total		Σ3	Total	
	number fraction	number fraction		number fraction	number fraction	
	0.344	0.445		0.331	0.44	
Grain Boundary Character	Low (2°-15°)	CSL	High (15°-180°)	Low (2°-15°)	CSL	High (15°-180°)
	0.358885	0.444637	0.196479	0.259847	0.439929	0.300225
Total Length /Sample Points	0.014964 µm/point			0.017158 µm/point		

4.B. Comparison of EBSD Evaluated Microstructure for Batch D and E Samples Produced with Differing Deposition Temperatures

The previous two sections focused on differences in SiC material layers fabricated in the same batch before and after annealing. This section focuses on SiC material layers fabricated at different deposition temperatures. Figure 58 displays the IPF map overlayed on the corresponding IQ map for batches D and E reference samples side by side.

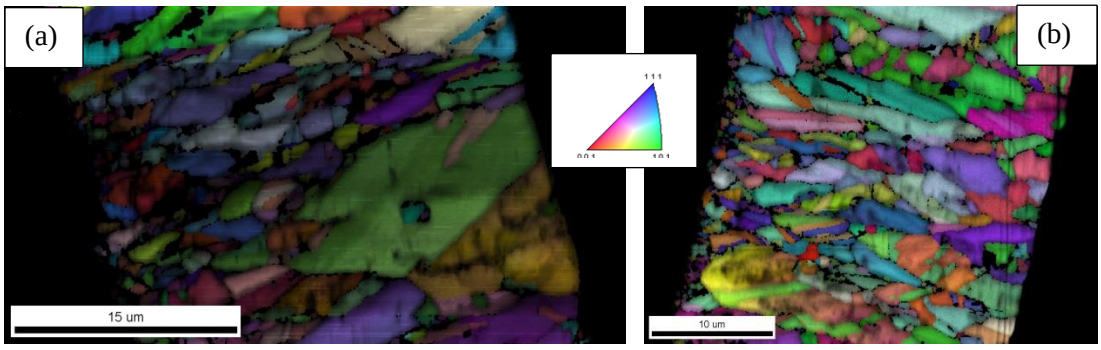

Figure 58. 3C- SiC inverse pole figures overlaid on IQ pattern for a) Dref, and b) Eref.

Both Dref and Eref have a set of random grain orientations on the sample suface. Eref grain sizes have a smaller range than those for Dref. Pole figures shown in Figure 59 indicate a random distribution of grain orientations. More maximum density areas with less intensity observed for the Eref sample confirm a greater uniformity in distribution of grain sizes.

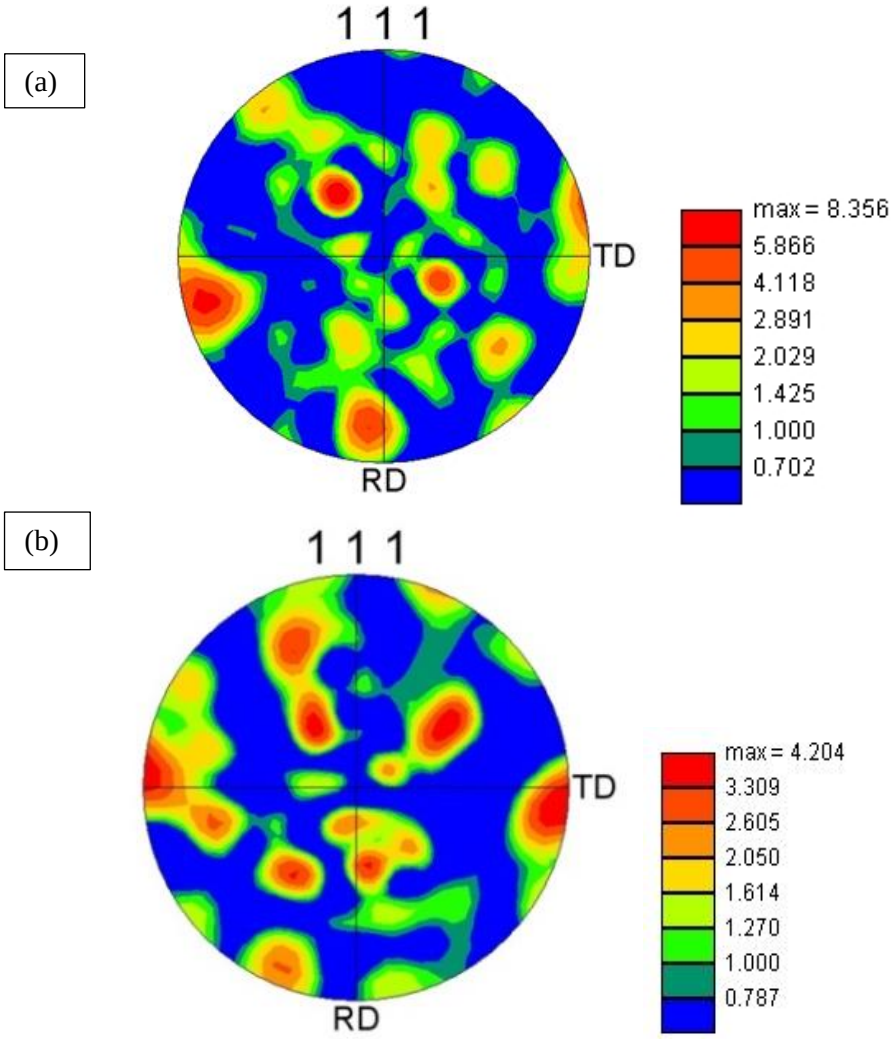

Figure 59. 3C-SiC pole figures for a) Dref, and b) Eref.

Misorientation angle distributions appear to be statistically similar for both Dref and Eref as illustrated in Figure 60. Slight differences are observed in initial low misorientation angles and 60˚ angle misorientations, associated with Σ1 and Σ3 CSL boundaries, respectively. These differences may not be as insignificant as they might appear to be when considering the very different of behavior of the materials when exposed to heat treatment as demonstrated in the previous sections.

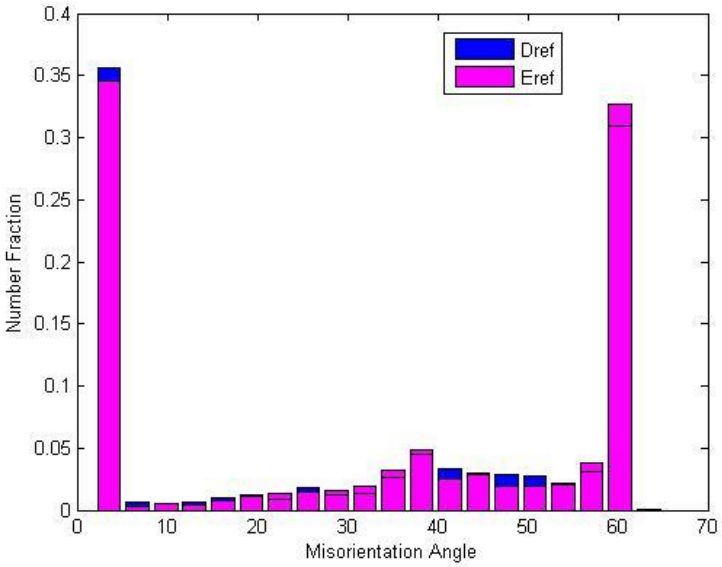

Figure 60. 3C-SiC Misorientation angle comparison of samples Dref and Eref.

Grain boundary maps presented in Sections 4.A.1 and 4.A.2 are placed side by side for visual comparison in Figure 61 without the corresponding legends t hat have already been presented in Figures 36 and 52 for samples Dref and Eref, respectively. Figure 62 illustrates the difference in GBCD of the two samples.

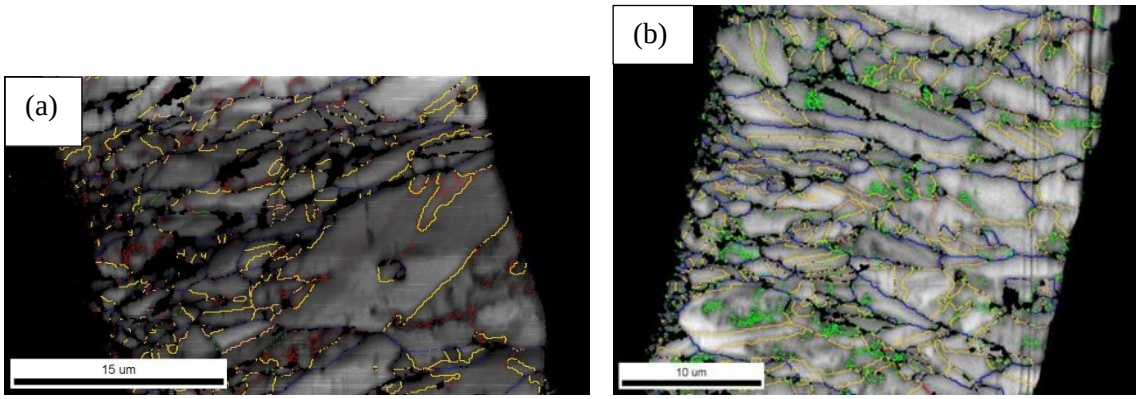

Figure 61. 3C-SiC grain boundary maps for a) Dref, and b) Eref.

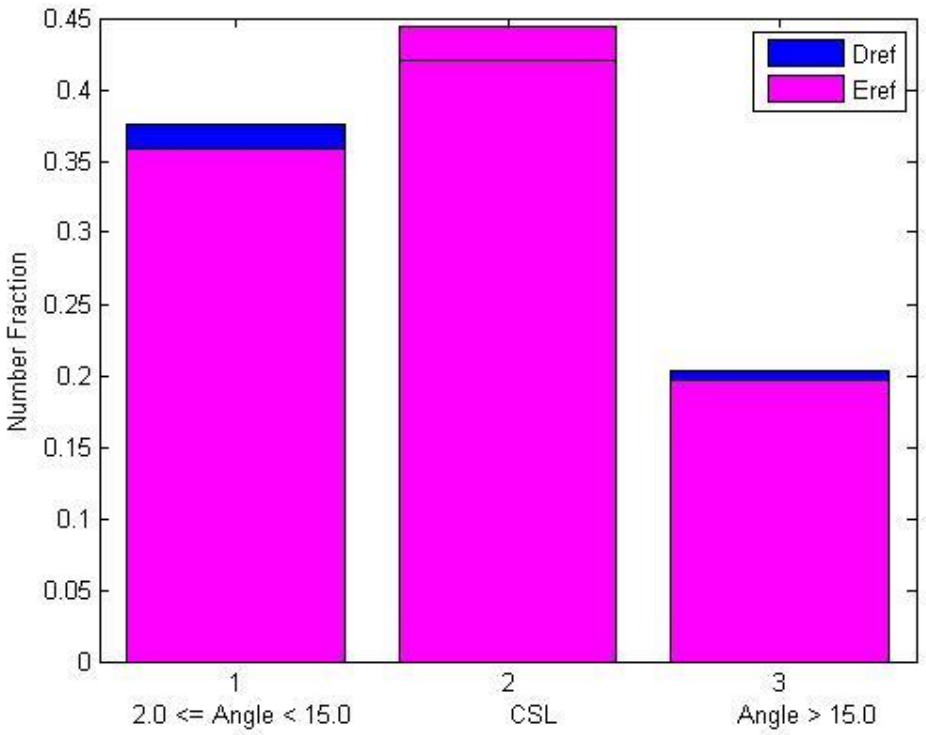

Figure 62. 3C-SiC GBCD comparison of samples Dref and Eref.

Eref has a slightly higher CSL concentration, about 2%, than Dref. This difference may be due in part to the better image quality of the Eref sample scan, yet it is suspected that the higher deposition temperature plays a key role in the observed result Overall, the grain boundary character distribution appears to be very similar for the reference samples. A closer look at CSL boundary differences can be taken from Figure 63. Most of the apparent differences in CSL boundary fractions seem to be in the special Σ3 and Σ9 boundaries.

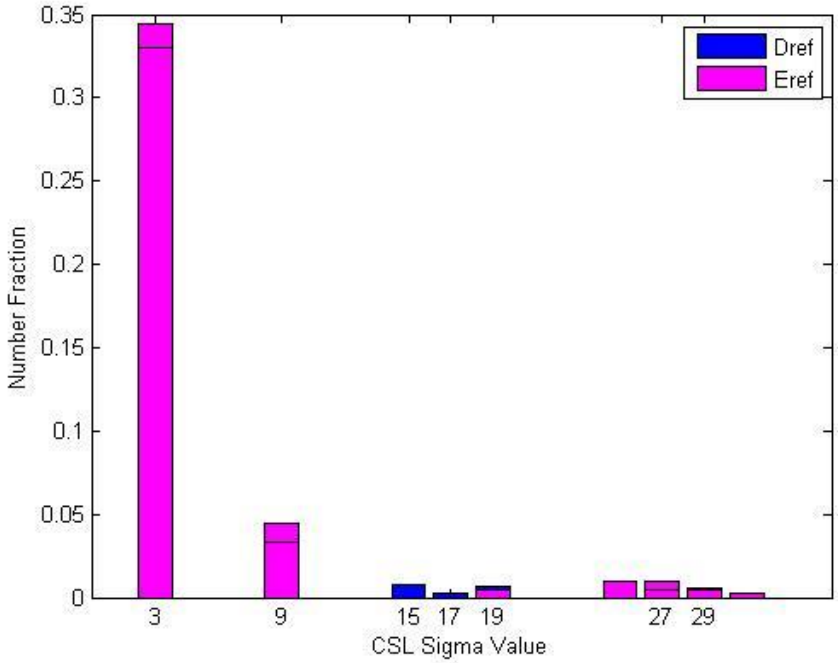

Figure 63. 3C- SiC CSL boundary comparison of samples Dref and Eref.

Figures 64 and 65 illustrate the grain size vs. area fraction and grain size vs. number fraction distibutions, respectively, for the reference samples. Other than the two larger grain categories displayed in Dref, both samples appear to have a similar range of grain size categories. The number fraction distribution for each sample has a similar pattern of starting high for the small grain categories and exponentially tapering off as the grain size categories increase, although the smaller grain size category number fractions remain elevated for Dref. It appears that the higher deposition temperature results in a more continuous distribution of grain sizes which would significantly affect the grain boundary characteristics of the material.

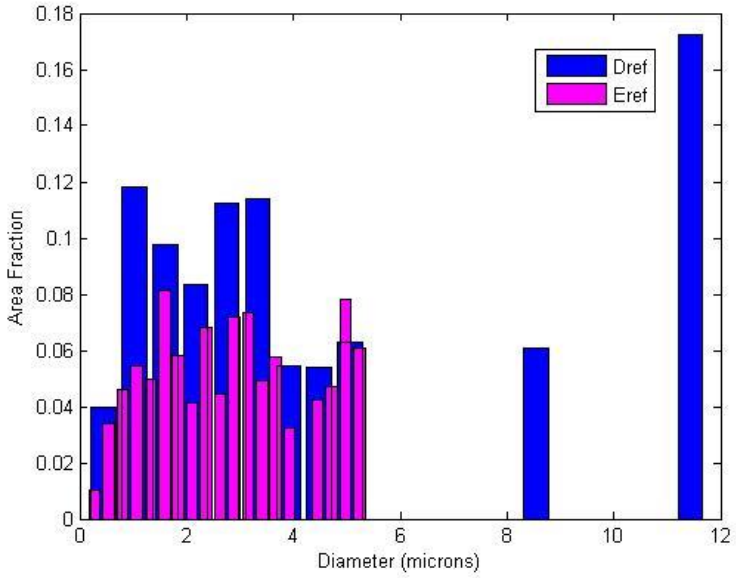

Figure 64. 3C-SiC grain size distribution comparison, diameter vs. area fraction, of samples Dref and Eref.

.

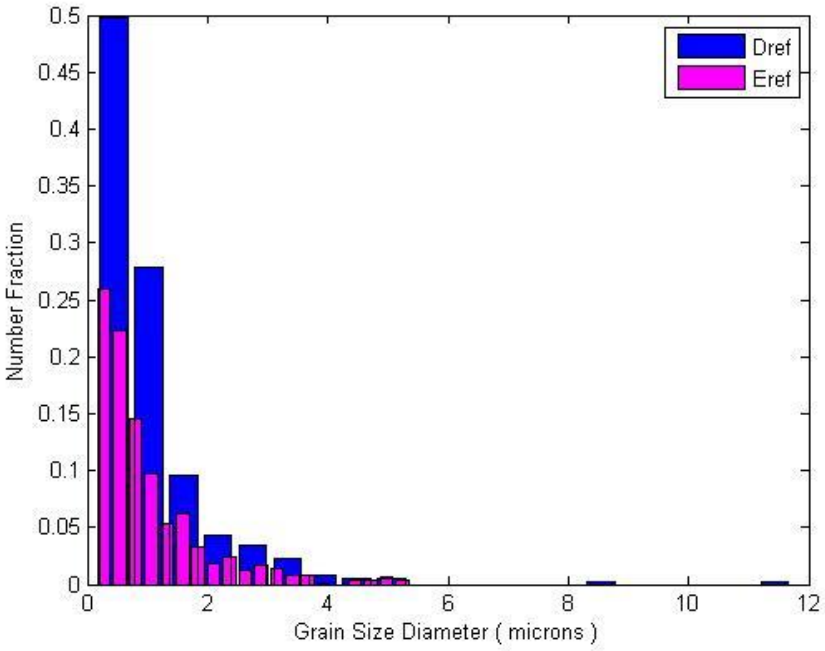

Figure 65. 3C-SiC grain size distribution comparison, diameter vs. number fraction, of samples Dref and Eref.

Table 10 summarizes the characteristic data for the two reference samples and displays the results side by side. The misorientation angles of interest differ by approximately one to two percent. This difference is relatively small; however, after annealing the two samples had significantly different misorientation angle distributions. The average grain diameters of the two samples are nearly the same; however, the distribution of grain sizes is much different as seen in the grain size charts displayed in Figures 64 and 65. The Eref sample appears to have more uniform grain sizes (i.e. a smaller distribution), with a much smaller quantity of very small grains. Unfortunately, the comparison is a bit skewed due to the random aquistion of a very large grain in some samples and not in others. For example, the Dref and Eref grain size range maximum values appear to be much different, yet without the very large grain, the maxima are very similar (as shown in Figure 64). Eref seems to have a higher number of grain boundaries before annealy, yet this difference might change to a lower quantity excluding the Dref larger grain from the comparison.

Table 10. 3C-SiC Grain and Grain Boundary Data Comparison Chart for D-ref and E-ref.

Characteristic	Dref			Eref		
Grain Size Distribution	Range		Average	Range		Average
	Min.	Max.	Diameter	Min.	Max.	Diameter
	(µm)	(µm)	(µm)	(µm)	(µm)	(µm)
	0.497093	11.4321	1.03	0.278855	5.23223	1.02
Grain Orientation	Density	Number		Density	Number	
	Maximum	Max. Regions		Maximum	Max. Regions	
	8.356	6		4.204	13	
Misorientation	Low Angle	60 ˚ Angle		Low Angle	60 ˚ Angle	
	# Fraction	# Fraction		# Fraction	# Fraction	
	0.356227	0.309701		0.345373	0.326722	
CSL	Σ3	Total		Σ3	Total	
	number fraction	number fraction		number fraction	number fraction	
	0.33	0.421		0.344	0.445	
Grain Boundary Character	Low (2˚-15˚)	CSL	High (15˚-180˚)	Low (2˚-15˚)	CSL	High (15˚-180˚)
	0.376246	0.420953	0.202801	0.358885	0.444637	0.196479
Total Length /Sample Area	0.01008 µm/point			0.014964 µm/point		

The results of EBSD 6H-SiC scans on the Dref and Eref samples, including previously discussed partitioning criteria are in part illustrated in Figure 66.

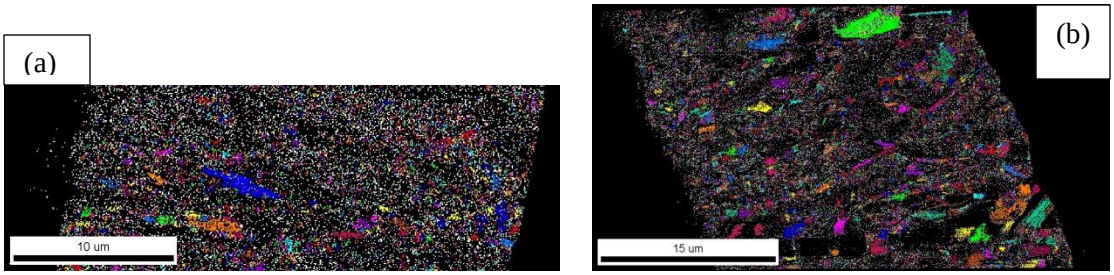

Figure 66. 6H-SiC scan grain maps for a) Dref, and b) Eref.

Eref was necessarily cropped to a smaller area for reasons discussed in Section 3.C.3. The sample surfaces are dotted with colorful points indicating that they have been identified by OIM as 6H-SiC. A few small areas of solid color indicate the possibility of 6H-SiC grains. These areas are not consistant with the dark spots in the 3C-SiC scans. The areas of solid color can not be both 3C-SiC and 6H-SiC. It may be that upon higher resolution, these points would be revealed as more loosely spread within large grains of 3C-SiC. The average CI for the 3C-SiC scan was much higher than the average CI values of 0.08 or less for the 6H-SiC scans, which casts doubt on the validity of the data inidicating the presence of 6H-SiC grains.

Figure 67 shows a grain size vs. area fraction distribution comparison between Dref and Eref 6H-SiC scans. The distribution shown in Figure 67 has a similar pattern to the number fraction distributions for the 3C-SiC scans at a reduced size. The average grain size appears to be slightly larger for the Eref sample, indicating the possibility that the higher deposition temperature is somewhat more favorable to the creation of 6H-SiC.

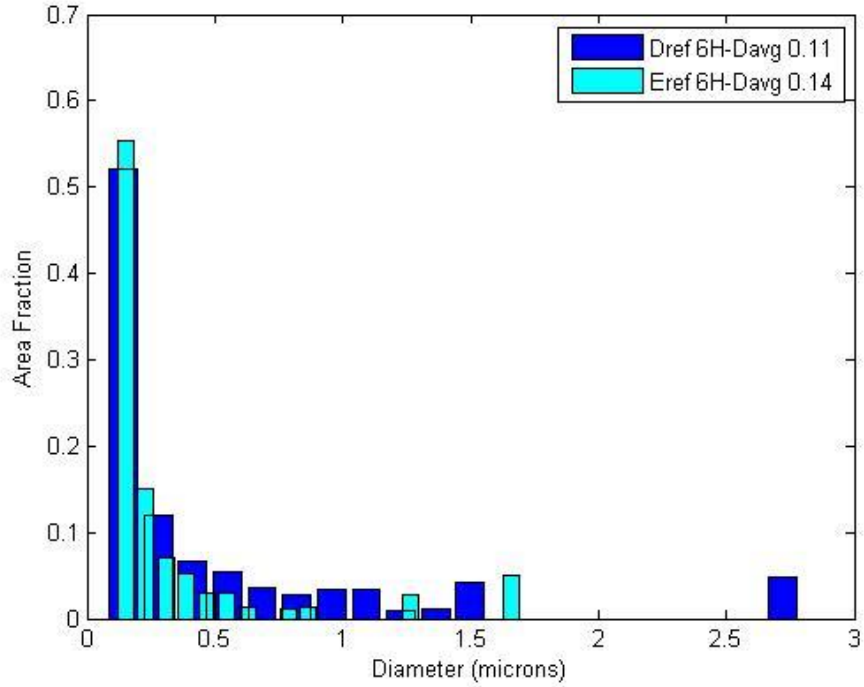

Figure 67. 6H-SiC scan grain size comparison, diameter vs. area fraction, of samples Dref and Eref.

The pole figures (see Figure 68) for both reference samples show a variety of grain orientations with what appears to be a orientations preferences perpendicular to the sample surface. This preferred orientation might indicate an aspect of deposition. Differences in the annealed samples strongly suggest a move towards more randomness of grain orientation as a result of heat treatment.

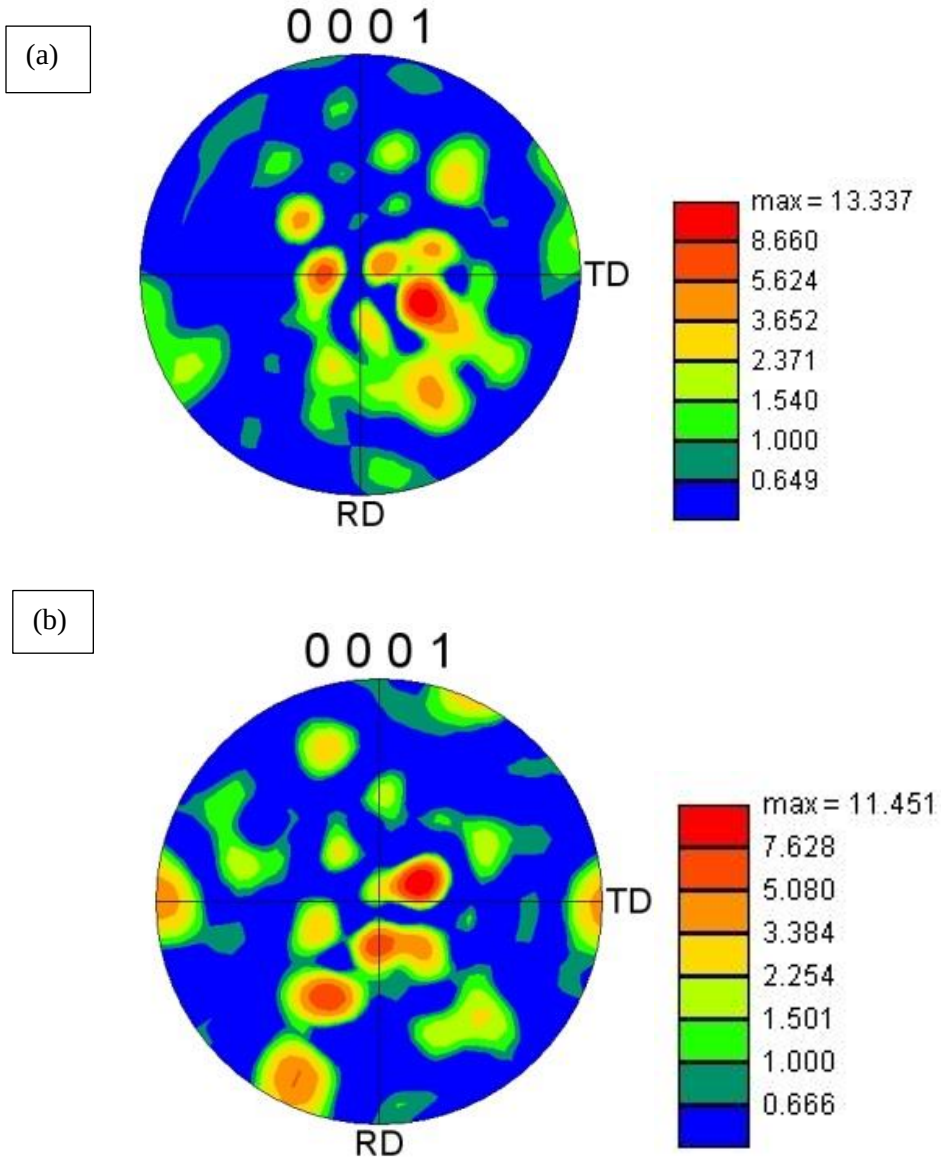

Figure 68. 6H-SiC pole figures for a) Dref , and b) Eref.

Table 6 in Section 4.A.2 lists the partition parameters and corresponding data statistics for Eref data collection. The point fractions remaining for the CI > 0.1 partition for 3C-SiC and 6H-SiC scans of Eref, are 0.697 and 0.24, respectively. These fractions are similar to the breakdown measurements of 0.654 and 0.228 found for Dref. See Table 4 in Sect 4.A.1. This difference in number fraction would indicate a small fraction

increase (about 1.2 %) in α-SiC formation at the higher deposition temperature. The image quality difference between the scans for Dref and Eref may also contribute to the noted difference in phase indexing percentages.

Table 11 presents selected grain and grain boundary data for comparison of all samples analysed in this study. Comparing equivilant area data for the Dref sample between samples gives a 6H-SiC to 3C-SiC area ratio of approximately 0.12%. The total grain boundary length divided by the number of indexed points was calculated as a way to normalize the data as all of the samples were of different size.

Table 11. Grain Size and Grain Boundary Data

Sample Grain Data	**D-ref SiC-3C**	**D-ref SiC-6H**	**D2000 SiC-3C**	**D2000 SiC-6H**	**Eref SiC-3C**	**Eref SiC-6H**	**E2000 SiC-3C**
Average Grain Diameter (μm)	1.03	0.11	0.95	0.09	1.02	0.14	0.79
Grain Diameter Std. Dev.(μm)	1.12	0.08	0.88	0.034	0.95	0.07	0.83
Equivalent Area (μm^2)	0.83	0.01	0.71	0.01	0.82	0.02	0.49
Equivalent ASTM number	17.2	23.8	17.5	24.3	17.3	23	18
Minimum Grain Size (μm)	0.437825	0.142	0.302	0.089	0.28	0.151	0.372
Maximum Grain Size (μm)	11.4321	2.719	6.14	0.663	5.23	1.66	8.87
Grain Boundary Length(μm)							
Rotational Angle 2˚-5˚	259.92	*	800.32	*	438.15	*	214.31
Rotational Angle 5˚-15˚	14.61	*	10.51	*	17.32	*	12.7
Rotational Angle 15˚-180˚	455.13	*	572.15	*	813.66	*	646.63
Total Length (μm)	729.66	*	1382.98	*	1269.13	*	873.64
Data Set Size (# of points)	72394	82986	74647	57115	84815	17893	50917
Total Length (μm)/Data Set Size	0.01007901	*	0.018527	*	0.014964	*	0.017158

Chapter 5.0 Conclusions

This study, conducted by analyzing one sample each of TRISO particle SiC layers with different production parameters, is very limited in statistical significance regarding the entirety of the SiC layer. The microstructure characterization per sample, on the other hand, is statistically sufficient. Tens of thousands of points contribute to the analysis, and determined parameters fall within statistical range of previous studies. The filtered data CI is high, indicating that approximately 95% of the evaluation points were indexed correctly. Evidence to support possible trends may be rightfully claimed; however, conclusion about the overall behavior of the materials can only be statistically sound after the evaluation of many more sample analyses. Analysis conducted in this study is intended to add to the overall data collection for further study.

CVD-coated SiC tends to produce a grain size distribution of two type; a relatively continuous range smaller grain sizes, and a small number of larger grain sizes sparsely populating the material. It is possible to take a small sample from the SiC layer and not catch the larger grains in the sample area. It is likely that in this study the larger grains were caught in the D-ref and E2000 samples, but not in the D2000 and E-ref samples, somewhat complicating analysis. Conclusions regarding the 6H-SiC phase are unaffected by the presence of the large particles. Careful consideration of the impact this inconsistency might have on differences in data regarding the 3C-SiC phase was needed.

Evidence has been found in this study to support the following:

- B1600 surface sample extraction method failure to produce a clear signal for EBSD analysis due to high energy ion beam damage (amorphization) that

might be fixed by adding an additional step of removing damaged thickness via high energy beam at an angle that would eliminate back sputter and subsequently polishing at low energy with descending currents

- B1600 grains, which are relatively small, rounded and form a netlike boundary structure compared to the elongated oval shaped grains identified in Batches D and E may correlate with higher strength

- Annealing treatments for both Batches D (SiC layer deposition temperature of 1450 ˚C), and E (SiC layer deposition temperature of 1510 ˚C) result in the increase of grain boundaries, a trend towards uniformity in grain size, and a more compact elongated columnar grain shaped structure, which increases the proportion of radial grain boundary pathways between pyrolytic carbon layers

- Annealing treatment for Batch D increases low angle boundaries in the OPyC region, that may work to improve resistance to fission product migration, at the expense of CSL boundaries, which may correlate with characteristic strength

- Annealing treatment for Batch E increases high angle boundaries that may not be desirable regarding fission product migration, yet does not significantly decrease the quantity of CSL boundaries that are believed to enhance macroscopic properties such as characteristic strength and resistance to irradiation damage

- Higher deposition temperature forms a microstructure more resistant to change upon exposure to high temperatures such as that expected in reactor operation conditions, preserving the preferential ∑3 CSL boundaries formed by CVD fabrication

- Σ1 CSL boundaries correlate with hardness and Σ3 CSL correlate with greater characteristic strength

- Presence of 6H-SiC is negligible and randomly scattered within the SiC matrix
- 6H-SiC presence reduced through annealing
- slightly increased 6H-SiC presence for higher deposition temperature

Further analysis on B1600 may reveal a better candidate material for limiting fission product grain boundary migration; however, B1600 has demonstrated a loss of characteristic strength upon heat treatment in a prior study. (See Figure 24) The loss may or may not be significant regarding the ability to maintain structural integrity of the SiC layer pressure vessel in high temperature accident conditions. If the loss is not significant, then the potential enhancement of reduction in fission product migration is appealing and worth investigation. Batches D and E annealed samples reveal several radial pathways not considered desirable for curtailing fission product migration.

It appears that the CVD SiC fabrication method is favorable to ∑3 CSL boundary production. The more grain boundaries formed during fabrication, the higher the concentration of ∑3 boundaries found in the material. What could be discerned from the B1600 scan was a collection of rounder, smaller grains. The significantly lower strength of the annealed sample produced under similar conditions to that of B1600 shown in Figure 24 may indicate that the heated grains easily assume more random orientations with respect to each other resulting in a significant reduction in ∑3 boundaries thought to be correlated with characteristic strength. The material similar to B1600 remains stronger than most batches after annealing at 1600℃, which is another factor in favor of further investigation into Batch B SiC material.

The annealing treatment on Batch D resulting in a high concentration of low angle boundaries in the outer region of the SiC layer may prove beneficial. The low angle boundaries may form a bottleneck in that region significantly slowing fission product movement. This phenomenon is also worth further investigation.

The RCF coater, in which Batch B samples were prepared, appears to produce material with higher strength and more desirable grain, and grain boundary structure. This is likely due to the smaller capacity and geometrical configuration of the fluidized bed chamber, and rate of deposition compared to that of the ACF coater, in which Batches D and E were prepared. It is also suspected that RCF is using an additional inert flow gas in the fabrication process to improve fluidization of the particles.

EBSD analysis is highly useful in characterizing microstructure when the difficulties of ceramic surface preparation are overcome. FIB/SEM extraction and polishing methods are also highly useful when done carefully. Further studies would be needed to be conducted to determine the reason the proposed extraction method did not result in a good EBSD signal for the B1600 sample, but did for other samples analyzed.

References

Calister, W.D. (2007). *Materials Science and Engineering: An Introduction.* New York, NY: John Wiley and Sons, Inc.

Chen, Y., Zhang, X. "Focused Ion Beam Technology and Application in Failure Analysis", 11th International Conference on Electronic Packaging Technology & High Density Packaging, Tianhe District, Guangzhou, Guangdon, P.R. China, 2010, Paper No. 110, 978-1-4244-8142/10.

Dingley, D. J., & Wright, S. I. (2009). Determination of crystal phase from an electron backscatter diffraction pattern. *Journal of Applied Crystallography,* 42, 234-241.

Field, D. P. (1997). Recent advances in the application of orientation imaging. *Ultra microscopy, 67, 1-9.*

Fuchs, E., Oppolzer, H., & Rehme, H. (1990). *Particle Beam Microanalysis; Fundamentals, Methods, and Applications.* Weinheim (Federal Republic of Germany): VCH

Giannuzzi, L. A. & Stevie, F. A. (Eds.). (2005). *Introduction to Focused Ion Beams: Instruments, Theory, Technique, and Practice.* New York, NY: Springer

Goela, J.S., Burns, L.E, & Taylor, R.L. (1994). Transparent chemical vapor deposited SiC. *Applied Physics Letters,* 64, 131-133.

Gourgues-Lorenzon, A. F. (2009). Application of electron backscatter diffraction to the study of phase transformations: present and possible future. *Journal of Microscopy,* 233, 460-473.

Helary, D., Dugne, O., Bourrat, X., Jouneau, P.H., & Cellier, F. (2006). EBSD investigation of SiC for HTR fuel particles. *Journal of Nuclear Materials,* 350, 332-335.

Ishitani et al. (2007). *U. S. Patent No. 7,235,798 B2.* Washington, DC: U.S.

King, A. H., & Shekhar, S. (2006). What does it mean to be special? The significance and application of the Brandon criterion. *Journal of Materials Science, 41, 7675-7682.*

Kirchhofer, R., Hunn J.D., Demkowicz, P.A., Cole, J.I., & Gorman, B.P. (2013). Microstructure of TRISO coated particles from the AGR-1 experiment: SiC grain size and grain boundary character. *Journal of Nuclear Materials,* 432, 127-134.

Kunze, K., Wright, S.I., Adams, B.L., & Dingley, D.J. (1993). Advances in Automatic EBSP Single Orientation Measurements. *Textures and Measurements,* 20, 41-54.

Lassen, N. C. K. (1998). Automatic high-precision measurements of the location and width of Kikuchi bands in electron backscatter diffraction patterns. *Journal of Microscopy,* 190, 375-391.

Lefevre, R. L. R., & Price, M.S.T. (1977) Coated Nuclear Fuel Particles: The Coating Process and Its Model. *Nuclear Technology, 35, 263-278.*

Lopez-Honorato, E., Tan, J. Meadows, P.J., Marsh, G., & Xiao, P. (2009). TRISO coated fuel particles with enhanced SiC properties. *Journal of Nuclear Materials, 392, 219-224.*

Lopez-Honorato, E., Zhang, H., & Xiao, P. (2011). Silver diffusion in silicon carbide coatings. *J. Am. Ceram. Soc*., 94[9], 3064-3071. DOI: 10.111/j-1551-2916.2011.04544.x

Loretto, M. H. (1984). *Electron Beam Analysis of Materials.* New York, NY: Chapman and Hall

McPhail, D.S., Chater, R.J., and Li, L. (2008). Applications of focused ion beam SIMS in materials science. *Microchim Acta*, 161, 387–397. DOI:10.1007/s00604-007-0913-x

Nicholls, D.R. (2002). The pebble bed modular reactor. *South African Journal of Science.* 98, 31-35.

OIM Analysis Manuel. (2007) TexSEM Laboratories, Inc.

Orloff, Jon. (1993). High resolution focused ion beams. *Rev. Sci. Instrum.*, 64(5), 1105-1130.

Pensl, G., Ciobanu, F., Frank, T., Krieger, M., Reshanov, S., Schmid, F., & Weidner, M. (2005). SiC Material Properties. *International Journal of High Speed Electronics and Systems*, 15(4), 705-745.

Petti, D., et. al. (2010). The DOE Advanced Gas Reactor Fuel Development and Qualification Program. *The Journal of The Minerals, Metals, & Materials Society*, 62(9), 62-66.

Randle, V. (2006). Advances in Electron Backscatter Diffraction for the Characterisation of Interfaces. *Microchim Acta*, 155, 31-37. doi:10.1007/s00604-006-0503-3

Randle, V. & Engler, O. (2000). *Introduction to Texture Analysis: Macrotexture, Microtexture, & Orientation Mapping.* Singapore: OPA (Overseas Publishers Association)

Sakata, T., Ogiwara, T., Takahshi, H., & Sekine, T. (1999). Investigation of Ga Contamination due to Analysis by Dual Beam FIB, *IEEE*, O-7695-0315-2/99, 389-393.

Sahu, T., Ghosh, B., Pradhan, S.K., & Ganguly, T. (2012). Diverse role of Silicon Carbide in the domain of nanomaterials. *International Journal of Electrochemistry*, 2012, Article ID 271285, 7 pages. doi:10.1155/2012/271285.

Schmidt, C. (2006, March). The next generation of nuclear power? *Environmental Science & Technology*, 1382-1383.

Sedov, A.A., & Frolov, A.A. (2011). Computational Study of the Influence of Some Systematic Factors on the Fuel Temperature in a Very High Temperature Gas-Cooled Reactor with Prismatic Fuel Assemblies. *Physics of Atomic Nuclei,* 3, 80-90.

Shih, S., Park, M., & Cockayne D. J. H. (2007). The interpretation of indexing of high Σ CSL boundaries from ceramics. *Journal of Microscopy, 227, 309-314.*

Snead, L.L., Nozawa, T., Katoh, Y., Byun, T-S., Kondo, S., & Petti, D. (2007). Handbook of SiC properties for fuel performance modeling. *Journal of Nuclear Materials,* 371, 329-377.

Steckl, A. J., & Chyr, I. (1998). Focused ion beam micro milling of GaN and related substrate materials (sapphire, SiC, and Si). *J. Vac.Sci. Technol B,* 17(2), 362-365.

TexSEM Laboratories, Inc. (2007). OIM Analysis 5.3 Manuel: Author

Tan, L., Allen, T.R., Hunn, J.D., & Miller, J.H. (2008). EBSD for microstructure and property characterization of the SiC-coating in TRISO fuel particles. *Journal of Nuclear Materials,* 372, 400-404.

van Rooyen, I.J. (2011). Effects of Phosphorus Doping and Very High Temperatures on the Nanostructures of Silicon Carbide and TRISO Coated Particles (Doctoral dissertation)

van Rooyen, I.J., Neethling, J. H., van Rooyen, P.M. (2010). The influence of annealing temperature on the strength of TRISO coated particles. *Journal of Nuclear Materials.* 402, 136/146.

van Rooyen, I.J., Dunzik-Gougar, M.L. & van Rooyen, P.M. (2012, November). *Silver (Ag) Transport Mechanisms in TRISO Coated Particles: A Critical Review.* Paper presented at the Proceedings of the HTR 2012, Tokyo, Japan.

van Rooyen, I.J., Dunzik-Gougar, M.L., van Rooyen, & P.M., Trowbridge, T., (2012, October). *On Techniques to Characterize and Correlate Grain Size, Grain Boundary Orientation and the Strength of the SiC Layer of TRISO Coated Particles: A Preliminary Study*, Paper presented at the Proceedings of the HTR 2012, Tokyo, Japan.

van Rooyen, I.J., et al. (2011). Effects of phosphorous-doping and high temperature annealing on CVD grown 3C-SiC. *Nuclear Engineering and Design*, doi:10.1016/j.nucengdes.2011.09.066.

Watanabe, T. (2011). Grain boundary engineering: historical perspective and future prospects. *Journal of Materials Science,* 46, 4095-4115.

Wright, S.I. (2006). Random thought on non-random misorientation distributions. *Materials Science and Technology,* 22(11), 1287-1296.

Young, R., & Carleson, P. (2004). A Tool for Advanced Failure Analysis. *Evaluation Engineering*, September, 60-63.

Zanbergen H.W., et al. (2004).Application of The Dual-Beam FIB/SEM to Metals Research. *Journal of Microscopy*, 214.3, 237-245.

Appendix 1
CSL Boundary Specifications

Table 12. CSL Boundary Specifications

CSL Sigma Values and Corresponding Chrystal Rotations		
Sigma Value	Angle (degrees)	< u, v, w>
3	60	<1 1 1>
5	36.9	<1 0 0>
7	38.2	<1 1 1>
9	38.9	<1 1 0>
11	50.5	<1 1 0>
13a	22.6	<1 0 0>
13b	27.8	<1 1 1>
15	48.2	<2 1 0>
17a	28.1	<1 1 0>
17b	61.9	<2 2 1>
19a	26.5	<1 1 0>
19b	46.8	<1 1 1>
21a	21.8	<1 1 1>
21b	44.4	<2 1 1>
23	40.5	<3 1 1>
25a	16.3	<1 0 0>
25b	51.7	<3 3 1>
27a	31.6	<1 1 0>
27b	35.4	<2 1 0>
29a	43.6	<1 0 0>
29b	46.4	<2 2 1>
31a	17.9	<1 1 0>
31b	52.2	<3 1 1>
33a	20.0	<1 1 0>
33b	33.6	<3 1 1>
33c	59.0	<1 1 0>
35a	34.0	<2 1 1>
35b	43.2	<3 3 1>
37a	18.9	<1 0 0>
37b	43.1	<3 1 0>
37c	50.6	<1 1 1>
39a	32.2	<1 1 1>
39b	50.1	<3 2 1>
41a	12.7	<1 0 0>
41b	40.9	<2 1 0>
41c	55.9	<1 1 0>
43a	15.2	<1 1 1>
43b	27.9	<2 1 0>
43c	60.8	<3 3 2>
45a	28.6	<3 1 1>
45b	36.9	<2 2 1>
45c	53.1	<2 2 1>
47a	37.1	<3 3 1>
47b	43.7	<3 2 0>
49a	43.6	<1 1 1>
49b	43.6	<5 1 1>
49c	49.2	<3 2 2>

Appendix 2
D-ref 3C-SiC OIM Data

Table 13. D-ref 3C-SiC Scan OIM Clean Up Data Statistics

Dref_scan2 cropped cleaned-NOC cleaned-NOC cleaned-NOC cleaned-NOC cleaned-NOC cleaned-NOC cleaned-NOC cleaned-NOC cleaned-NOC cleaned-NOC cleaned-NOC cleaned-NOC cleaned-NOC cleaned-NOC cleane NOC cleaned-NOC cleaned-NOC cleaned-NOC cleaned-NOC cleaned-NOC cleaned-NOC cleaned-CIS cleaned-FitS
Operator: Support
Calibration: 0.554300 0.905900 0.651900
Working Distance: 10.000000

Number of points: 110748
Number of good points: 103223

Dimensions:
X Min: 0.00 microns
X Max: 41.90 microns
Y Min: 0.00 microns
Y Max: 22.78 microns
Step: 0.10 microns

Average Confidence Index: 0.40
Average Image Quality: 1127.73
Average Fit [degrees]: 1.24

Phases:
Silicon Carbide 3C

Cropped
Cleanup - Neighbor Orientation Correlation: 6990 points changed (level 3, tolerance 5.0, min CI 0.00)
Cleanup - Neighbor Orientation Correlation: 1669 points changed (level 3, tolerance 5.0, min CI 0.00)
Cleanup - Neighbor Orientation Correlation: 590 points changed (level 3, tolerance 5.0, min CI 0.00)
Cleanup - Neighbor Orientation Correlation: 284 points changed (level 3, tolerance 5.0, min CI 0.00)
Cleanup - Neighbor Orientation Correlation: 169 points changed (level 3, tolerance 5.0, min CI 0.00)
Cleanup - Neighbor Orientation Correlation: 91 points changed (level 3, tolerance 5.0, min CI 0.00)
Cleanup - Neighbor Orientation Correlation: 51 points changed (level 3, tolerance 5.0, min CI 0.00)
Cleanup - Neighbor Orientation Correlation: 31 points changed (level 3, tolerance 5.0, min CI 0.00)
Cleanup - Neighbor Orientation Correlation: 20 points changed (level 3, tolerance 5.0, min CI 0.00)
Cleanup - Neighbor Orientation Correlation: 9 points changed (level 3, tolerance 5.0, min CI 0.00)
Cleanup - Neighbor Orientation Correlation: 7 points changed (level 3, tolerance 5.0, min CI 0.00)
Cleanup - Neighbor Orientation Correlation: 6 points changed (level 3, tolerance 5.0, min CI 0.00)
Cleanup - Neighbor Orientation Correlation: 5 points changed (level 3, tolerance 5.0, min CI 0.00)
Cleanup - Neighbor Orientation Correlation: 5 points changed (level 3, tolerance 5.0, min CI 0.00)
Cleanup - Neighbor Orientation Correlation: 2 points changed (level 3, tolerance 5.0, min CI 0.00)
Cleanup - Neighbor Orientation Correlation: 1 points changed (level 3, tolerance 5.0, min CI 0.00)
Cleanup - Neighbor Orientation Correlation: 1 points changed (level 3, tolerance 5.0, min CI 0.00)
Cleanup - Neighbor Orientation Correlation: 1 points changed (level 3, tolerance 5.0, min CI 0.00)
Cleanup - Neighbor Orientation Correlation: 1 points changed (level 3, tolerance 5.0, min CI 0.00)
Cleanup - Neighbor Orientation Correlation: 0 points changed (level 3, tolerance 5.0, min CI 0.00)
Cleanup - Grain CI Standardization (tolerance 5.0, min size 3, Multi Row 0)
Cleanup - Grain Fit Standardization (tolerance 5.0, min size 3, Multi Row 0)

ame:New Partition
Formula:PCI[&]>0.100 AND PIQ[&]>500.0
Number of points in partition: 72394
Fraction of points in partition: 0.654
Number of indexed points: 72394

Average Confidence Index: 0.56
Average Image Quality: 1350.59
Average Fit [degrees]: 0.94

Phases:
Silicon Carbide 3C

Grain Size (Excluding Edge Grains):
Averages are number averages
Number of Grains: 344
Number of Edge Grains: 27
Average Diameter: 1.03 (0.97) microns
  Equivalent Area: 0.83 (0.74) square microns
  Equivalent ASTM No.: 17.2 (17.4)

Average Grain Shape (Excluding Edge Grains):
Calculated by enforcing the average area and
aspect ratio and then using a fitting approach
to determine the angle.
Major Axis: 1.17 (1.10) microns
Minor Axis: 0.49 (0.47) microns
Angle to the Horizontal: 338.40 (157.48) degrees

Shape ellipses only scaled relative to one another.

Name:New Partition
Formula:PIQ[&]>500.0
Number of points in partition: 88368
Fraction of points in partition: 0.798
Number of indexed points: 88247

Average Confidence Index: 0.46
Average Image Quality: 1261.71
Average Fit [degrees]: 1.12

Phases:
Silicon Carbide 3C

Grain Size (Excluding Edge Grains):
Averages are number averages
Number of Grains: 2195
Number of Edge Grains: 63
Average Diameter: 0.34 (0.32) microns
  Equivalent Area: 0.09 (0.08) square microns
  Equivalent ASTM No.: 20.5 (20.6)
Dref

Operator: Support
Calibration: 0.554300 0.905900 0.651900
Working Distance: 10.000000

Number of points: 278240
Number of previously highlighted points 202145
Number of good points: 200688

Dimensions:
X Min: 0.00 microns
X Max: 54.40 microns
Y Min: 0.00 microns
Y Max: 44.17 microns
Step: 0.10 microns

Average Confidence Index: 0.11
Average Image Quality: 3337.91
Average Fit [degrees]: 1.78

Phases:
Silicon Carbide 3C

Dref_scan2

Operator: Support
Calibration: 0.554300 0.905900 0.651900

Table 14. Dref 3C-SiC Scan Overall CSL Boundary Number Fractions

Overall fraction of CSL boundaries: 0.421

Sigma	Number Fraction
3	0.330036
5	0.000633012
7	0.00181991
9	0.0330749
11	0.00324418
13a	0.00379807
13b	0.000474759
15	0.00767526
17a	0.000237379
17b	0.0030068
19a	0.00680487
19b	7.91264e-005
21a	0.000316506
21b	0.000237379
23	0.00110777
25a	0.00134515
25b	0.000553885
27a	0.00490584
27b	0.00134515
29a	0.00609274
29b	7.91264e-005
31a	0.00158253
31b	0.00189903
33a	0.000870391
33b	0
33c	0.000316506
35a	0.000553885
35b	0.000237379
37a	0
37b	0
37c	0.000474759
39a	0
39b	0
41a	7.91264e-005
41b	0.000474759
41c	0.000870391
43a	0.000712138
43b	0.000395632
43c	0.000949517
45a	0.000237379
45b	0
45c	0
47a	0
47b	7.91264e-005
49a	0
49b	0.00181991
49c	0.00253205

Table 15. D-ref 3C-SiC Scan ASTM and Misorientation Data

Chart: Grain Size (ASTM)

Edge grains included in analysis

ASTM Number	Number Fraction
10.5396	0.00290698
11.1699	0.00290698
11.8002	0
12.4305	0.00290698
13.0608	0.0116279
13.6912	0.0232558
14.3215	0.0348837
14.9518	0.0319767
15.5821	0.0494186
16.2125	0.0552326
16.8428	0.104651
17.4731	0.0988372
18.1034	0.0959302
18.7337	0.0959302
19.3641	0.0843023
19.9944	0.0959302
20.6247	0.0436046
21.255	0.0901163
21.8853	0.0203488
22.5157	0.0552326
Average Number	18.2919
Standard Deviation	2.4013
Area	13.8394

Chart: Misorientation Angle

Angle [degrees]	Number Fraction
3.575	0.356227
6.725	0.006884
9.875	0.00522235
13.025	0.00680487
16.175	0.0100491
19.325	0.0115525
22.475	0.00894129
25.625	0.0178826
28.775	0.0120272
31.925	0.0130559
35.075	0.0264282
38.225	0.0453395
41.375	0.0335496
44.525	0.0286438
47.675	0.028802
50.825	0.0272195
53.975	0.0201772
57.125	0.0314923
60.275	0.309701
63.425	0
Average Number	32.4636

Table 16. D-ref 3C-SiC Scan Grain Size Data

Chart: Grain Size (diameter)

Edge grains included in analysis

Diameter [microns]	Number Fraction
0.437825	0.497093
1.01647	0.27907
1.59511	0.0959302
2.17376	0.0436046
2.7524	0.0348837
3.33105	0.0232558
3.90969	0.00872093
4.48834	0.00581395
5.06698	0.00581395
5.64563	0
6.22427	0
6.80292	0
7.38156	0
7.96021	0
8.53885	0.00290698
9.1175	0
9.69614	0
10.2748	0
10.8534	0
11.4321	0.00290698
Average	
Number	1.03062
Standard Deviation	1.12285
Area	4.73693

Chart: Grain Size (diameter)

Edge grains included in analysis

Diameter [microns]	Area Fraction
0.437825	0.0396512
1.01647	0.118415
1.59511	0.0973934
2.17376	0.0832827
2.7524	0.112237
3.33105	0.114172
3.90969	0.0546879
4.48834	0.0541213
5.06698	0.0628559
5.64563	0
6.22427	0
6.80292	0
7.38156	0
7.96021	0
8.53885	0.0909807
9.1175	0
9.69614	0
10.2748	0
10.8534	0
11.4321	0.172204
Average	
Number	1.03062
Standard Deviation	1.12285
Area	4.73693

Table 17. D-ref 3C-SiC Scan Comprehensive Boundary Data

Boundaries: Rotation Angle

	Min	Max	Fraction	Number	Length
——	2°	5°	0,356	4502	259,92 microns
——	5°	15°	0,020	253	14,61 microns
——	15°	180°	0,624	7883	455,13 microns

Boundaries: CSL

	Sigma	Tolerance	Fraction	Volume	MDF Value	Number	Length
	3	8,66	0,330	0,0176	18,79	4171	240,813 microns
	5	6,71	0,001	0,0123	0,05	0	0,46188 microns
	7	5,67	0,002	0,0099	0,18	23	1,3279 microns
	9	5,00	0,033	0,0102	3,26	418	24,1332 microns
	11	4,52	0,003	0,0075	0,43	41	2,36714 microns
	13a	4,16	0,004	0,0029	1,30	48	2,77128 microns
	13b	4,16	0,000	0,0039	0,12	6	0,34641 microns
	15	3,87	0,008	0,0094	0,81	97	5,6003 microns
	17a	3,64	0,000	0,0020	0,12	3	0,173205 microns
	17b	3,64	0,003	0,0039	0,77	38	2,19393 microns
	19a	3,44	0,007	0,0033	2,06	86	4,96521 microns
	19b	3,44	0,000	0,0022	0,04	1	0,057735 microns
	21a	3,27	0,000	0,0019	0,17	4	0,23094 microns
	21b	3,27	0,000	0,0057	0,04	3	0,173205 microns
	23	3,13	0,001	0,0050	0,22	14	0,80829 microns
	25a	3,00	0,001	0,0011	1,23	17	0,981495 microns
	25b	3,00	0,001	0,0044	0,13	7	0,404145 microns
	27a	2,89	0,005	0,0020	2,51	62	3,57957 microns
	27b	2,89	0,001	0,0039	0,34	17	0,981495 microns
	29a	2,79	0,006	0,0009	6,94	77	4,44559 microns
	29b	2,79	0,000	0,0035	0,02	1	0,057735 microns
	31a	2,69	0,002	0,0011	1,49	20	1,1547 microns
	31b	2,69	0,002	0,0032	0,60	24	1,38564 microns
	33a	2,61	0,001	0,0014	0,60	11	0,635085 microns
	33b	2,61	0,000	0,0029	0,00	0	0 microns
	33c	2,61	0,000	0,0014	0,22	4	0,23094 microns
	35a	2,54	0,001	0,0026	0,21	7	0,404145 microns
	35b	2,54	0,000	0,0026	0,09	3	0,173205 microns
	37a	2,47	0,000	0,0008	0,00	0	0 microns
	37b	2,47	0,000	0,0024	0,00	0	0 microns
	37c	2,47	0,001	0,0009	0,68	7	0,404145 microns
	39a	2,40	0,000	0,0008	0,00	0	0 microns
	39b	2,40	0,000	0,0045	0,00	0	0 microns
	41a	2,34	0,000	0,0005	0,15	1	0,057735 microns
	41b	2,34	0,000	0,0021	0,23	6	0,34641 microns
	41c	2,34	0,001	0,0010	0,83	11	0,635085 microns
	43a	2,29	0,001	0,0005	1,10	9	0,519615 microns
	43b	2,29	0,000	0,0019	0,20	5	0,288675 microns
	43c	2,29	0,001	0,0010	1,14	14	0,80829 microns
	45a	2,24	0,000	0,0018	0,13	3	0,173205 microns
	45b	2,24	0,000	0,0018	0,00	0	0 microns
	45c	2,24	0,000	0,0016	0,00	0	0 microns
	47a	2,19	0,000	0,0017	0,00	0	0 microns
	47b	2,19	0,000	0,0017	0,05	1	0,057735 microns
	49a	2,14	0,000	0,0005	0,00	0	0 microns
	49b	2,14	0,002	0,0016	1,14	23	1,3279 microns
	49c	2,14	0,003	0,0016	1,58	32	1,84752 microns
	summary	-	0,421	0,1575	2,67		

*For statistics - any point pair with misorientation exceeding 2° is considered a boundary

Appendix 3
D2000 3C-SiC OIM Data

Table 18. D2000 3C-SiC Clean Up Data and Sample Statistics

Average Confidence Index: 0.39
Average Image Quality: 961.87
Average Fit [degrees]: 1.79

Phases:
Silicon Carbide 3C

Name:New Partition
Formula:PCI[&]>0.100 AND PIQ[&]>400.0
Number of points in partition: 74647
Fraction of points in partition: 0.690
Number of indexed points: 74647

Average Confidence Index: 0.53
Average Image Quality: 1190.71
Average Fit [degrees]: 1.05

Phases:
Silicon Carbide 3C

Grain Size (Excluding Edge Grains):
Averages are number averages
Number of Grains: 489
Number of Edge Grains: 42
Average Diameter: 0.95 (0.93) microns
Equivalent Area: 0.71 (0.68) square microns
Equivalent ASTM No.: 17.5 (17.5)

Average Grain Shape (Excluding Edge Grains):
Calculated by enforcing the average area and aspect ratio and then using a fitting approach to determine the angle.
Major Axis: 0.99 (0.95) microns
Minor Axis: 0.42 (0.41) microns
Angle to the Horizontal: 351.44 (171.91) degrees

Shape ellipses only scaled relative to one another.

Name:New Partition
Formula:PIQ[&]>400.0
Number of points in partition: 75985
Fraction of points in partition: 0.792
Number of indexed points: 75797

Average Confidence Index: 0.45
Average Image Quality: 1139.95
Average Fit [degrees]: 1.18

Phases:
Silicon Carbide 3C

Grain Size (Excluding Edge Grains):
Averages are number averages
Number of Grains: 1379
Number of Edge Grains: 64
Average Diameter: 0.43 (0.41) microns
Equivalent Area: 0.14 (0.13) square microns
Equivalent ASTM No.: 19.8 (19.9)

Average Grain Shape (Excluding Edge Grains):
Calculated by enforcing the average area and aspect ratio and then using a fitting approach to determine the angle.
Major Axis: 0.51 (0.49) microns
Minor Axis: 0.27 (0.26) microns
Angle to the Horizontal: 352.04 (172.22) degrees

Shape ellipses only scaled relative to one another.

July26

Operator: Support
Calibration: 0.548600 0.915000 0.684100
Working Distance: 10.000000

Number of points: 164625
Number of good points: 135328

Dimensions:
X Min: 0.00 microns
X Max: 48.80 microns
Y Min: 0.00 microns
Y Max: 29.10 microns
Step: 0.10 microns

.

Table 19. D2000 3C-SiC Overall CSL Boundary Number Fractions

Chart: CSL Boundaries

Overall fraction of CSL boundaries: 0.289

Sigma	Number Fraction
3	0.225557
5	0.0018786
7	0.0044669
9	0.0226267
11	0.0037572
13a	0.00146113
13b	0.00025048
15	0.000709694
17a	4.17467e-005
17b	0.00108541
19a	0.00204559
19b	4.17467e-005
21a	0.00100192
21b	0.00116891
23	8.34934e-005
25a	0.00154463
25b	0.00012524
27a	0.00367371
27b	0.00171161
29a	0.00388244
29b	0.00037572
31a	0
31b	0.00175336
33a	0.00237956
33b	0.00025048
33c	0.000208733
35a	8.34934e-005
35b	0
37a	4.17467e-005
37b	0.000709694
37c	0
39a	0.000208733
39b	0.000208733
41a	0.00141939
41b	0
41c	0.00171161
43a	0
43b	4.17467e-005
43c	0.000333973
45a	0.00037572
45b	0.000459213
45c	0
47a	0.00050096
47b	4.17467e-005
49a	0
49b	0.00087688
49c	0.00012524

Table 20. D2000 3C-SiC Scan ASTM and Misorientation Data

Chart: Grain Size (ASTM)

Edge grains included in analysis

ASTM Number	Number Fraction
12.2878	0.00408998
12.8284	0.00613497
13.3691	0.0122699
13.9098	0.00817996
14.4505	0.0224949
14.9911	0.0449898
15.5318	0.0470348
16.0725	0.0756646
16.6131	0.0695297
17.1538	0.0470348
17.6945	0.0552147
18.2351	0.0695297
18.7758	0.0961145
19.3165	0.114519
19.8571	0.0736196
20.3978	0.0858896
20.9385	0.0184049
21.4792	0.0490798
22.0198	0.0593047
22.5605	0.0408998
Average	
Number	18.4615
Standard Deviation	2.37995
Area	14.9497

Chart: Misorientation Angle

Angle [degrees]	Number Fraction
4.45	0.0290105
9.35	0.00696247
14.25	0.004632
19.15	0.00589929
24.05	0.00690459
28.95	0.0139539
33.85	0.0305642
38.75	0.025955
43.65	0.0213002
48.55	0.0201593
53.45	0.02132
58.35	0.039851
63.25	0.0447694
68.15	0.373742
73.05	0.239248
77.95	0.0309602
82.85	0.0290258
87.75	0.0324179
92.65	0.0233245
97.55	0
Average	
Number	64.2605

Table 21. D2000 3C-SiC Scan Grain Size Data

Chart: Grain Size (diameter)

Edge grains included in analysis

Diameter [microns]	Area Fraction
0.302214	0.0181477
0.609637	0.0554215
0.917059	0.0427691
1.22448	0.077684
1.5319	0.114395
1.83933	0.0892106
2.14675	0.0911406
2.45417	0.0764107
2.76159	0.0566948
3.06902	0.0439083
3.37644	0.0417638
3.68386	0.034486
3.99128	0.0590806
4.2987	0.0218871
4.60613	0.0260287
4.91355	0.0571371
5.22097	0
5.52839	0
5.83582	0
6.14324	0.0938346
Average	
Number	0.951239
Standard Deviation	0.882687
Area	2.76961

Chart: Grain Size (area)

Edge grains included in analysis

Area [square microns]	Number Fraction
0.795444	0.781186
2.35169	0.114519
3.90794	0.0490798
5.46419	0.0163599
7.02043	0.00817996
8.57668	0.00613497
10.1329	0.00408998
11.6892	0.00408998
13.2454	0.00408998
14.8017	0.00204499
16.3579	0.00204499
17.9142	0.00408998
19.4704	0
21.0267	0
22.5829	0
24.1392	0
25.6954	0
27.2517	0
28.8079	0.00204499
30.3641	0.00204499
Average	
Number	1.32135
Standard Deviation	2.99512
Area	8.09653

Table 22. D2000 3C-SiC Comprehensive Boundary Data

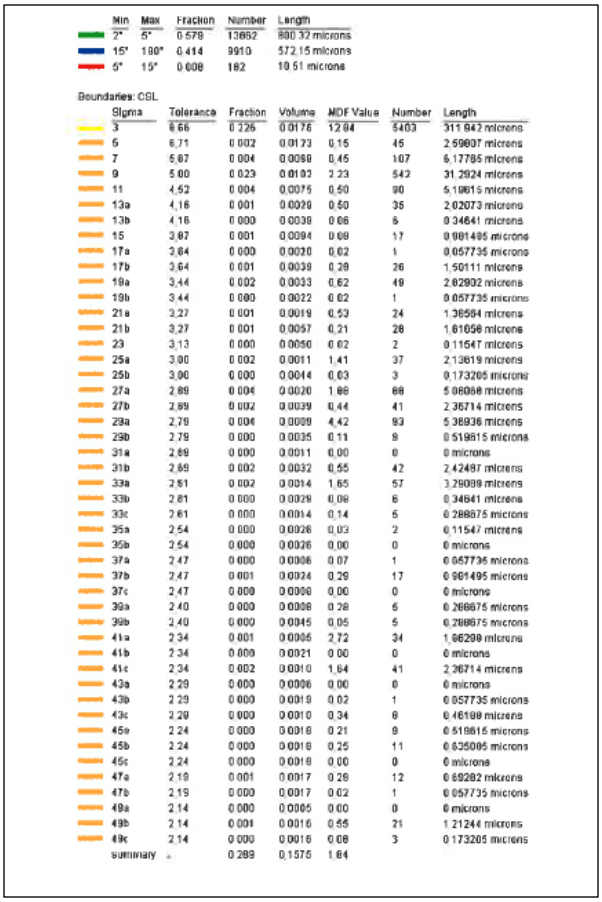

Min	Max	Fraction	Number	Length
2°	5°	0.578	13862	800.32 microns
15°	180°	0.414	9910	572.15 microns
5°	15°	0.008	182	10.51 microns

Boundaries: CSL

	Sigma	Tolerance	Fraction	Volume	MDF Value	Number	Length
	3	8.66	0.226	0.0176	12.84	5403	311.842 microns
	5	6.71	0.002	0.0123	0.15	45	2.59807 microns
	7	5.87	0.004	0.0068	0.45	107	6.17785 microns
	9	5.00	0.023	0.0183	2.23	542	31.2924 microns
	11	4.52	0.004	0.0075	0.50	90	5.19615 microns
	13a	4.16	0.001	0.0029	0.50	35	2.02073 microns
	13b	4.16	0.000	0.0038	0.06	6	0.34641 microns
	15	3.87	0.001	0.0094	0.09	17	0.981495 microns
	17a	3.64	0.000	0.0020	0.02	1	0.057735 microns
	17b	3.64	0.001	0.0039	0.28	26	1.50111 microns
	19a	3.44	0.002	0.0033	0.62	49	2.82902 microns
	19b	3.44	0.000	0.0022	0.02	1	0.057735 microns
	21a	3.27	0.001	0.0019	0.53	24	1.38564 microns
	21b	3.27	0.001	0.0057	0.21	28	1.61658 microns
	23	3.13	0.000	0.0050	0.02	2	0.11547 microns
	25a	3.00	0.002	0.0011	1.41	37	2.13819 microns
	25b	3.00	0.000	0.0044	0.03	3	0.173205 microns
	27a	2.89	0.004	0.0020	1.88	88	5.08068 microns
	27b	2.89	0.002	0.0039	0.44	41	2.36714 microns
	29a	2.79	0.004	0.0009	4.42	93	5.36936 microns
	29b	2.79	0.000	0.0035	0.11	9	0.519615 microns
	31a	2.69	0.000	0.0011	0.00	0	0 microns
	31b	2.69	0.002	0.0032	0.55	42	2.42487 microns
	33a	2.61	0.002	0.0014	1.65	57	3.29089 microns
	33b	2.61	0.000	0.0029	0.06	6	0.34641 microns
	33c	2.61	0.000	0.0014	0.14	5	0.288675 microns
	35a	2.54	0.000	0.0026	0.03	2	0.11547 microns
	35b	2.54	0.000	0.0026	0.00	0	0 microns
	37a	2.47	0.000	0.0006	0.07	1	0.057735 microns
	37b	2.47	0.001	0.0024	0.29	17	0.981495 microns
	37c	2.47	0.000	0.0000	0.00	0	0 microns
	39a	2.40	0.000	0.0008	0.28	6	0.288675 microns
	39b	2.40	0.000	0.0045	0.05	5	0.288675 microns
	41a	2.34	0.001	0.0005	2.72	34	1.96299 microns
	41b	2.34	0.000	0.0021	0.00	0	0 microns
	41c	2.34	0.002	0.0010	1.84	41	2.36714 microns
	43a	2.29	0.000	0.0006	0.00	0	0 microns
	43b	2.29	0.000	0.0019	0.02	1	0.057735 microns
	43c	2.29	0.000	0.0010	0.34	8	0.46188 microns
	45a	2.24	0.000	0.0018	0.21	9	0.519615 microns
	45b	2.24	0.000	0.0019	0.25	11	0.635085 microns
	45c	2.24	0.000	0.0018	0.00	0	0 microns
	47a	2.19	0.001	0.0017	0.28	12	0.69282 microns
	47b	2.19	0.000	0.0017	0.02	1	0.057735 microns
	49a	2.14	0.000	0.0005	0.00	0	0 microns
	49b	2.14	0.001	0.0016	0.55	21	1.21244 microns
	49c	2.14	0.000	0.0018	0.08	3	0.173205 microns
	summary	-	0.289	0.1575	1.84		

Appendix 4
E-ref 3C-SiC OIM Data

Table 23. E-ref 3C-SiC Scan OIM Clean Up Data Statistics

Eref09182012 cropped cleaned-NOC cleaned-CIS cleaned-FitS

Operator: Support
Calibration: 0.563000 0.918700 0.643900
Working Distance: 10.000000

Number of points: 121662
Number of good points: 108974

Dimensions:
X Min: 0.00 microns
X Max: 37.50 microns
Y Min: 0.00 microns
Y Max: 27.97 microns
Step: 0.10 microns

Average Confidence Index: 0.51
Average Image Quality: 1880.33
Average Fit [degrees]: 1.08

Phases:
Silicon Carbide 3C

Cropped
Cleanup - Neighbor Orientation Correlation: 7764 points changed (level 3, tolerance 5.0, min CI 0.00)
Cleanup - Neighbor Orientation Correlation: 1193 points changed (level 3, tolerance 5.0, min CI 0.00)
Cleanup - Neighbor Orientation Correlation: 314 points changed (level 3, tolerance 5.0, min CI 0.00)
Cleanup - Neighbor Orientation Correlation: 138 points changed (level 3, tolerance 5.0, min CI 0.00)
Cleanup - Neighbor Orientation Correlation: 81 points changed (level 3, tolerance 5.0, min CI 0.00)
Cleanup - Neighbor Orientation Correlation: 48 points changed (level 3, tolerance 5.0, min CI 0.00)
Cleanup - Neighbor Orientation Correlation: 35 points changed (level 3, tolerance 5.0, min CI 0.00)
Cleanup - Neighbor Orientation Correlation: 28 points changed (level 3, tolerance 5.0, min CI 0.00)
Cleanup - Neighbor Orientation Correlation: 19 points changed (level 3, tolerance 5.0, min CI 0.00)
Cleanup - Neighbor Orientation Correlation: 18 points changed (level 3, tolerance 5.0, min CI 0.00)
Cleanup - Neighbor Orientation Correlation: 17 points changed (level 3, tolerance 5.0, min CI 0.00)
Cleanup - Neighbor Orientation Correlation: 14 points changed (level 3, tolerance 5.0, min CI 0.00)
Cleanup - Neighbor Orientation Correlation: 10 points changed (level 3, tolerance 5.0, min CI 0.00)
Cleanup - Neighbor Orientation Correlation: 7 points changed (level 3, tolerance 5.0, min CI 0.00)
Cleanup - Neighbor Orientation Correlation: 5 points changed (level 3, tolerance 5.0, min CI 0.00)
Cleanup - Neighbor Orientation Correlation: 4 points changed (level 3, tolerance 5.0, min CI 0.00)
Cleanup - Neighbor Orientation Correlation: 5 points changed (level 3, tolerance 5.0, min CI 0.00)
Cleanup - Neighbor Orientation Correlation: 5 points changed (level 3, tolerance 5.0, min CI 0.00)
Cleanup - Neighbor Orientation Correlation: 6 points changed (level 3, tolerance 5.0, min CI 0.00)
Cleanup - Neighbor Orientation Correlation: 4 points changed (level 3, tolerance 5.0, min CI 0.00)
Cleanup - Neighbor Orientation Correlation: 3 points changed (level 3, tolerance 5.0, min CI 0.00)
Cleanup - Neighbor Orientation Correlation: 2 points changed (level 3, tolerance 5.0, min CI 0.00)
Cleanup - Neighbor Orientation Correlation: 2 points changed (level 3, tolerance 5.0, min CI 0.00)
Cleanup - Neighbor Orientation Correlation: 1 points changed (level 3, tolerance 5.0, min CI 0.00)
Cleanup - Neighbor Orientation Correlation: 1 points changed (level 3, tolerance 5.0, min CI 0.00)
Cleanup - Neighbor Orientation Correlation: 1 points changed (level 3, tolerance 5.0, min CI 0.00)
Cleanup - Neighbor Orientation Correlation: 0 points changed (level 3, tolerance 5.0, min CI 0.00)
Cleanup - Grain CI Standardization (tolerance 5.0, min size 3, Multi Row 0)
Cleanup - Grain Fit Standardization (tolerance 5.0, min size 3, Multi Row 0)

Name:All data
Formula:
Number of points in partition: 168311
Fraction of points in partition: 1.000
Number of indexed points: 167156

Average Confidence Index: 0.17
Average Image Quality: 1768.95
Average Fit [degrees]: 1.67

Phases:
Silicon Carbide 3C

Grain Size (Excluding Edge Grains):
Averages are number averages
Number of Grains: 3347
Number of Edge Grains: 3
Average Diameter: 0.33 (0.33) microns
  Equivalent Area: 0.08 (0.08) square microns
  Equivalent ASTM No.: 20.5 (20.5)

Name:New Partition
Formula:PIQ[&]>500.0 AND PCI[&]>0.100
Number of points in partition: 84815
Fraction of points in partition: 0.697
Number of indexed points: 84815

Average Confidence Index: 0.65
Average Image Quality: 2208.57
Average Fit [degrees]: 0.79

Phases:
Silicon Carbide 3C

Grain Size (Excluding Edge Grains):
Averages are number averages
Number of Grains: 483
Number of Edge Grains: 27
Average Diameter: 1.02 (1.00) microns
  Equivalent Area: 0.82 (0.78) square microns
  Equivalent ASTM No.: 17.3 (17.3)

Average Grain Shape (Excluding Edge Grains):
Calculated by enforcing the average area and aspect ratio and then using a fitting approach to determine the angle.
Major Axis: 1.04 (1.02) microns
Minor Axis: 0.46 (0.46) microns
Angle to the Horizontal: 8.60 (9.18) degrees

Shape ellipses only scaled relative to one another.

Table 24. E-ref 3C-SiC Scan Overall CSL Boundary Number Fractions

Chart: CSL Boundaries

Overall fraction of CSL boundaries: 0.445

Sigma	Number Fraction
3	0.344191
5	0.00122828
7	0.00291147
9	0.0449459
11	0.0022291
13a	0.000409428
13b	0.00104631
15	0.00100082
17a	0
17b	0.00204713
19a	0.00509508
19b	0.00127377
21a	0.000545901
21b	0.00204713
23	4.54918e-005
25a	0.00350287
25b	0.000636885
27a	0.00932581
27b	0.00313893
29a	0.00486762
29b	0.000909835
31a	0.00295696
31b	0.000591393
33a	0.000727868
33b	0.000136475
33c	4.54918e-005
35a	0.000864344
35b	0.000500409
37a	0.000136475
37b	9.09835e-005
37c	9.09835e-005
39a	0.000318442
39b	0.00177418
41a	4.54918e-005
41b	0.000181967
41c	0.000500409
43a	0.000727868
43b	0.000272951
43c	0.00145574
45a	9.09835e-005
45b	9.09835e-005
45c	0.000227459
47a	0
47b	0.000227459
49a	0
49b	0.000864344
49c	0.000318442

Table 25. E-ref 3C-SiC Scan ASTM and Misorientation Data

Chart: Grain Size (ASTM)

Edge grains included in analysis

ASTM Number	Number Fraction
12.7397	0.0165631
13.2572	0.00828157
13.7747	0.0248447
14.2922	0.0269151
14.8097	0.0331263
15.3272	0.0351967
15.8447	0.0559006
16.3622	0.0621118
16.8796	0.0517598
17.3971	0.0662526
17.9146	0.0786749
18.4321	0.0869565
18.9496	0.10766
19.4671	0.0496894
19.9846	0.0703934
20.5021	0.0621118
21.0196	0.0455487
21.5371	0.0248447
22.0546	0.0559006
22.5721	0.0372671
Average	
Number	18.275
Standard Deviation	2.41086
Area	14.7932

Chart: Misorientation Angle

Angle [degrees]	Number Fraction
3.575	0.345373
6.725	0.0033209
9.875	0.00509508
13.025	0.0044127
16.175	0.0077336
19.325	0.0121008
22.475	0.0129652
25.625	0.0146483
28.775	0.0159221
31.925	0.0196524
35.075	0.0319807
38.225	0.0485397
41.375	0.0251115
44.525	0.0294787
47.675	0.0188791
50.825	0.0191975
53.975	0.0208807
57.125	0.0379401
60.275	0.326722
63.425	4.54918e-005
Average	
Number	33.1932

Table 26. E-ref 3C-SiC Scan Grain Size Data

Chart: Grain Size (diameter)

Edge grains included in analysis

Diameter [microns]	Number Fraction
0.278855	0.258799
0.539559	0.223602
0.800263	0.144928
1.06097	0.0973085
1.32167	0.0538302
1.58238	0.0621118
1.84308	0.0331263
2.10378	0.0186335
2.36449	0.0248447
2.62519	0.0124224
2.8859	0.0165631
3.1466	0.0144928
3.4073	0.00828157
3.66801	0.00828157
3.92871	0.00414079
4.18942	0
4.45012	0.00414079
4.71082	0.00414079
4.97153	0.00621118
5.23223	0.00414079
Average	
Number	1.02156
Standard Deviation	0.945363
Area	2.83917

Chart: Grain Size (diameter)

Edge grains included in analysis

Diameter [microns]	Area Fraction
0.278855	0.0103445
0.539559	0.0339471
0.800263	0.0461199
1.06097	0.054648
1.32167	0.0495524
1.58238	0.0812111
1.84308	0.0580096
2.10378	0.0411659
2.36449	0.0680593
2.62519	0.0446573
2.8859	0.0716667
3.1466	0.0734734
3.4073	0.0489862
3.66801	0.0573727
3.92871	0.0324727
4.18942	0
4.45012	0.0421567
4.71082	0.0468748
4.97153	0.0782823
5.23223	0.0610175
Average	
Number	1.02156
Standard Deviation	0.945363
Area	2.83917

Table 27. E-ref 3C-SiC Scan Comprehensive Boundary Data

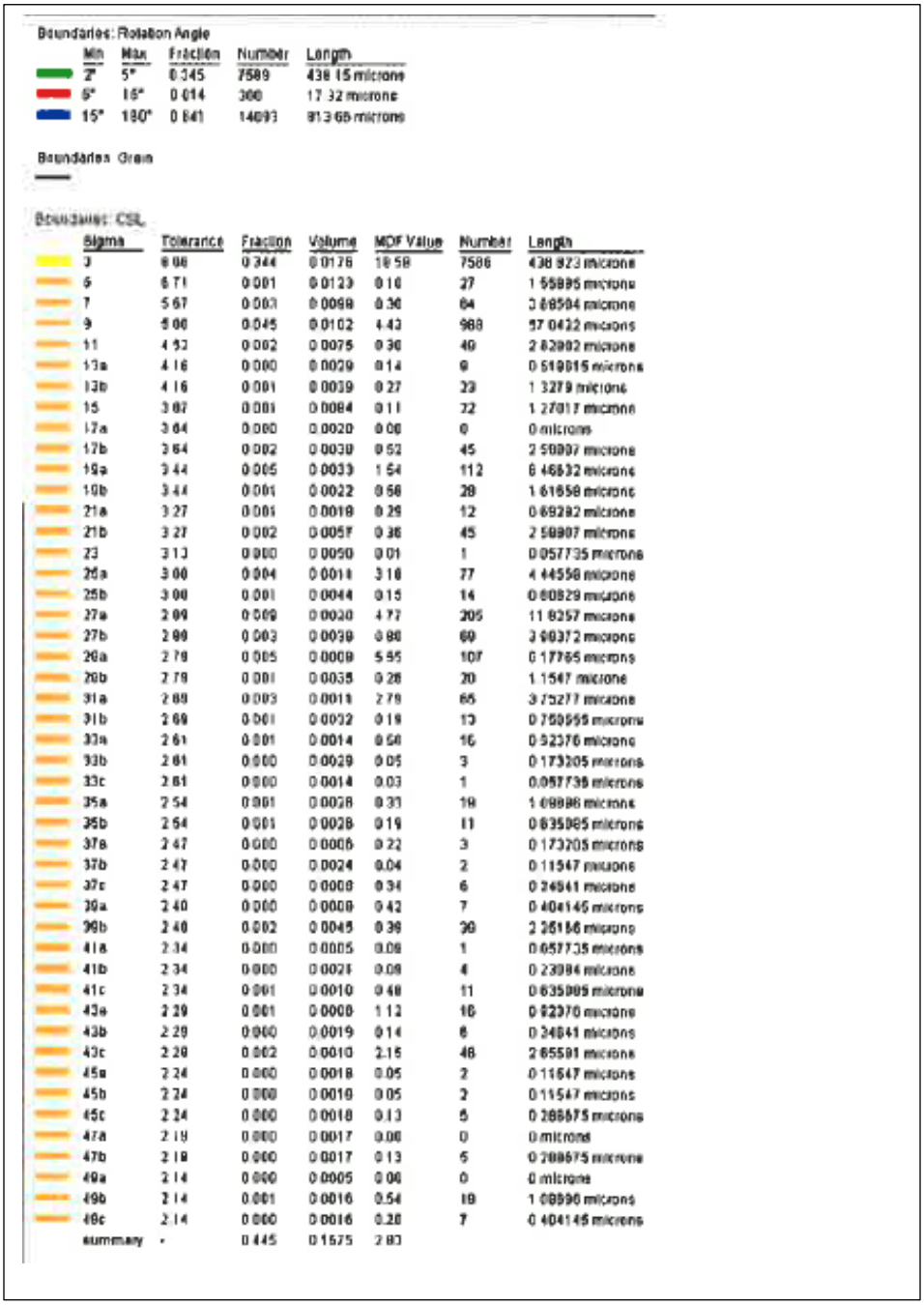

Boundaries: Rotation Angle

Min	Max	Fraction	Number	Length
2°	5°	0.345	7589	438.15 microns
5°	15°	0.014	300	17.32 microns
15°	180°	0.641	14093	813.65 microns

Boundaries: Grain

Boundaries: CSL

Sigma	Tolerance	Fraction	Volume	MDF Value	Number	Length
3	8.66	0.344	0.0176	10.58	7586	438.923 microns
5	6.71	0.001	0.0123	0.16	27	1.55895 microns
7	5.67	0.003	0.0068	0.36	64	3.68504 microns
9	5.00	0.045	0.0102	4.43	988	57.0422 microns
11	4.52	0.002	0.0075	0.36	49	2.82982 microns
13a	4.16	0.000	0.0029	0.14	9	0.519015 microns
13b	4.16	0.001	0.0039	0.27	23	1.3279 microns
15	3.87	0.001	0.0084	0.11	22	1.27017 microns
17a	3.64	0.000	0.0020	0.00	0	0 microns
17b	3.64	0.002	0.0039	0.52	45	2.59807 microns
19a	3.44	0.005	0.0033	1.54	112	6.46832 microns
19b	3.44	0.001	0.0022	0.58	28	1.61658 microns
21a	3.27	0.001	0.0019	0.29	12	0.69282 microns
21b	3.27	0.002	0.0057	0.36	45	2.59807 microns
23	3.13	0.000	0.0050	0.01	1	0.057735 microns
25a	3.00	0.004	0.0018	3.16	77	4.44558 microns
25b	3.00	0.001	0.0044	0.15	14	0.80829 microns
27a	2.89	0.009	0.0020	4.77	205	11.8357 microns
27b	2.89	0.003	0.0039	0.88	69	3.98372 microns
29a	2.79	0.005	0.0009	5.95	107	6.17765 microns
29b	2.79	0.001	0.0035	0.28	20	1.1547 microns
31a	2.69	0.003	0.0011	2.79	65	3.75277 microns
31b	2.69	0.001	0.0032	0.19	13	0.750555 microns
33a	2.61	0.001	0.0014	0.58	16	0.92376 microns
33b	2.61	0.000	0.0029	0.05	3	0.173205 microns
33c	2.61	0.000	0.0014	0.03	1	0.057735 microns
35a	2.54	0.001	0.0028	0.31	19	1.09886 microns
35b	2.54	0.001	0.0028	0.19	11	0.635085 microns
37a	2.47	0.000	0.0006	0.22	3	0.173205 microns
37b	2.47	0.000	0.0024	0.04	2	0.11547 microns
37c	2.47	0.000	0.0008	0.34	6	0.34641 microns
39a	2.40	0.000	0.0009	0.42	7	0.404145 microns
39b	2.40	0.002	0.0045	0.39	39	2.25166 microns
41a	2.34	0.000	0.0005	0.09	1	0.057735 microns
41b	2.34	0.000	0.0021	0.09	4	0.23094 microns
41c	2.34	0.001	0.0010	0.48	11	0.635085 microns
43a	2.29	0.001	0.0008	1.12	16	0.92376 microns
43b	2.29	0.000	0.0019	0.14	6	0.34641 microns
43c	2.29	0.002	0.0010	2.15	46	2.65591 microns
45a	2.24	0.000	0.0018	0.05	2	0.11547 microns
45b	2.24	0.000	0.0010	0.05	2	0.11547 microns
45c	2.24	0.000	0.0018	0.13	5	0.288675 microns
47a	2.19	0.000	0.0017	0.00	0	0 microns
47b	2.19	0.000	0.0017	0.13	5	0.288675 microns
49a	2.14	0.000	0.0005	0.00	0	0 microns
49b	2.14	0.001	0.0016	0.54	19	1.09886 microns
49c	2.14	0.000	0.0016	0.20	7	0.404145 microns
summary	-	0.445	0.1575	2.80		

Appendix 5
E2000 3C-SiC OIM Data

Table 28. E2000 3C-SiC Scan OIM Clean Up Data Statistics

E2000 Data Pull

E2000_Aug142012_scan1 cropped cleaned-NOC cleaned-NOC cleaned-NOC cleaned-NOC cleaned-NOC cleaned-NOC cleaned-NOC cleaned-NOC cleaned-NOC cleaned-NOC cleaned-NOC cleaned-NOC cleaned-NOC cleaned-NOC cleaned-CIS cleaned-FitS

Operator: Support
Calibration: 0.548600 0.915000 0.684100
Working Distance: 10.000000

Number of points: 59613
Number of good points: 59190

Dimensions:
X Min: 0.00 microns
X Max: 32.00 microns
Y Min: 0.00 microns
Y Max: 16.02 microns
Step: 0.10 microns

Average Confidence Index: 0.60
Average Image Quality: 1716.58
Average Fit [degrees]: 1.08

Phases:
Silicon Carbide 3C

Cropped
Cleanup - Neighbor Orientation Correlation: 2324 points changed (level 3, tolerance 5.0, min CI 0.00)
Cleanup - Neighbor Orientation Correlation: 408 points changed (level 3, tolerance 5.0, min CI 0.00)
Cleanup - Neighbor Orientation Correlation: 165 points changed (level 3, tolerance 5.0, min CI 0.00)
Cleanup - Neighbor Orientation Correlation: 77 points changed (level 3, tolerance 5.0, min CI 0.00)
Cleanup - Neighbor Orientation Correlation: 43 points changed (level 3, tolerance 5.0, min CI 0.00)
Cleanup - Neighbor Orientation Correlation: 33 points changed (level 3, tolerance 5.0, min CI 0.00)
Cleanup - Neighbor Orientation Correlation: 23 points changed (level 3, tolerance 5.0, min CI 0.00)
Cleanup - Neighbor Orientation Correlation: 20 points changed (level 3, tolerance 5.0, min CI 0.00)
Cleanup - Neighbor Orientation Correlation: 17 points changed (level 3, tolerance 5.0, min CI 0.00)
Cleanup - Neighbor Orientation Correlation: 16 points changed (level 3, tolerance 5.0, min CI 0.00)
Cleanup - Neighbor Orientation Correlation: 14 points changed (level 3, tolerance 5.0, min CI 0.00)
Cleanup - Neighbor Orientation Correlation: 8 points changed (level 3, tolerance 5.0, min CI 0.00)
Cleanup - Neighbor Orientation Correlation: 5 points changed (level 3, tolerance 5.0, min CI 0.00)
Cleanup - Neighbor Orientation Correlation: 2 points changed (level 3, tolerance 5.0, min CI 0.00)
Cleanup - Neighbor Orientation Correlation: 1 points changed (level 3, tolerance 5.0, min CI 0.00)
Cleanup - Neighbor Orientation Correlation: 1 points changed (level 3, tolerance 5.0, min CI 0.00)
Cleanup - Grain CI Standardization (tolerance 5.0, min size 3, Multi Row 0)
Cleanup - Grain Fit Standardization (tolerance 5.0, min size 3, Multi Row 0)

E2000 Data Pull

Name:New Partition
Formula:PCI[&]>0.100 AND PIQ[&]>45
Number of points in partition: 50917
Fraction of points in partition: 0.854
Number of indexed points: 50917

Average Confidence Index: 0.69
Average Image Quality: 1861.80
Average Fit [degrees]: 0.93

Phases:
Silicon Carbide 3C

Grain Size (Excluding Edge Grains):
Averages are number averages
Number of Grains: 431
Number of Edge Grains: 25
Average Diameter: 0.79 (0.77) microns
Equivalent Area: 0.49 (0.47) square
Equivalent ASTM No.: 18.0 (18.1)

Average Grain Shape (Excluding Edge
Calculated by enforcing the average a
aspect ratio and then using a fitting ap
to determine the angle.
Major Axis: 0.89 (0.83) microns
Minor Axis: 0.36 (0.34) microns
Angle to the Horizontal: 354.88 (174.0

Shape ellipses only scaled relative to o

E2000_Aug142012_scan1

Operator: Support
Calibration: 0.548600 0.915000 0.6841
Working Distance: 10.000000

Number of points: 87509
Number of previously highlighted poin
Number of good points: 81693

Dimensions:
X Min: 0.00 microns
X Max: 34.00 microns

Y Min: 0.00 microns
Y Max: 22.17 microns
Step: 0.10 microns

Average Confidence Index: 0.19
Average Image Quality: 1509.64
Average Fit [degrees]: 1.65

Phases:
Silicon Carbide 3C

Table 29. E2000 3C-SiC Scan Overall CSL Boundary Number Fractions

Chart: CSL Boundaries

Overall fraction of CSL boundaries: 0.440

Sigma	Number Fraction
3	0.331285
5	0.00819455
7	0.000793021
9	0.0509516
11	0.00330426
13a	0.000991277
13b	0.00125562
15	0.00535289
17a	0
17b	0.00257732
19a	0.00171821
19b	0.000660851
21a	0
21b	0.000859107
23	0.00165213
25a	0.000396511
25b	0.00237906
27a	0.00403119
27b	0.00687285
29a	0.000991277
29b	0.00244515
31a	0
31b	0.00013217
33a	0.00118953
33b	0.000594766
33c	0.000198255
35a	0.00105736
35b	0.00257732
37a	0
37b	0.00026434
37c	0
39a	0.000198255
39b	0.00323817
41a	0
41b	6.60851e-005
41c	6.60851e-005
43a	0.000660851
43b	0.000660851
43c	0.00026434
45a	0.00026434
45b	0.000396511
45c	0.00013217
47a	0.00026434
47b	0.00013217
49a	0
49b	0.000396511
49c	0.000462596

Table 30. E2000 3C-SiC Scan ASTM and Misorientation Data

Chart: Grain Size (ASTM)

Edge grains included in analysis

ASTM Number	Number Fraction
11.2535	0.00232019
11.8472	0
12.4409	0.00232019
13.0346	0.00232019
13.6283	0.00928074
14.222	0.0185615
14.8157	0.025522
15.4095	0.0348028
16.0032	0.0324826
16.5969	0.0464037
17.1906	0.0881671
17.7843	0.0881671
18.378	0.0672854
18.9717	0.0812065
19.5654	0.111369
20.1591	0.0858469
20.7528	0.106729
21.3466	0.0788863
21.9403	0.0394432
22.534	0.0788863

Average Number	19.0021
Standard Deviation	2.28347
Area	14.812

Chart: Misorientation Angle

Angle [degrees]	Number Fraction
3.575	0.245308
6.725	0.0035586
9.875	0.00555115
13.025	0.00462596
16.175	0.00422945
19.325	0.00819455
22.475	0.0115649
25.625	0.017843
28.775	0.0247819
31.925	0.0242532
35.075	0.0346286
38.225	0.0664016
41.375	0.0506873
44.525	0.0352895
47.675	0.0414354
50.825	0.0290775
53.975	0.0375363
57.125	0.0441449
60.275	0.310798
63.425	0

Average Number	37.2782

Table 31. E200 3C-SiC Scan Grain Size Data

Chart: Grain Size (diameter)

Edge grains included in analysis

Diameter [microns]	Number Fraction
0.372154	0.568446
0.819455	0.218097
1.26676	0.0974478
1.71406	0.0440835
2.16136	0.0232019
2.60866	0.0185615
3.05596	0.0139211
3.50326	0.00696056
3.95056	0.00464037
4.39786	0
4.84516	0
5.29246	0
5.73977	0.00232019
6.18707	0
6.63437	0
7.08167	0
7.52897	0
7.97627	0
8.42357	0
8.87087	0.00232019

Average Number	0.788013
Standard Deviation	0.82632
Area	3.32843

Chart: Grain Size (diameter)

Edge grains included in analysis

Diameter [microns]	Area Fraction
0.372154	0.0575453
0.819455	0.11511
1.26676	0.118116
1.71406	0.103696
2.16136	0.0834987
2.60866	0.0956797
3.05596	0.0965048
3.50326	0.0655023
3.95056	0.055561
4.39786	0
4.84516	0
5.29246	0
5.73977	0.0614157
6.18707	0
6.63437	0
7.08167	0
7.52897	0
7.97627	0
8.42357	0
8.87087	0.14737

Average Number	0.788013
Standard Deviation	0.82632
Area	3.32843

Table 32. E2000 3C-SiC Scan Comprehensive Boundary Data

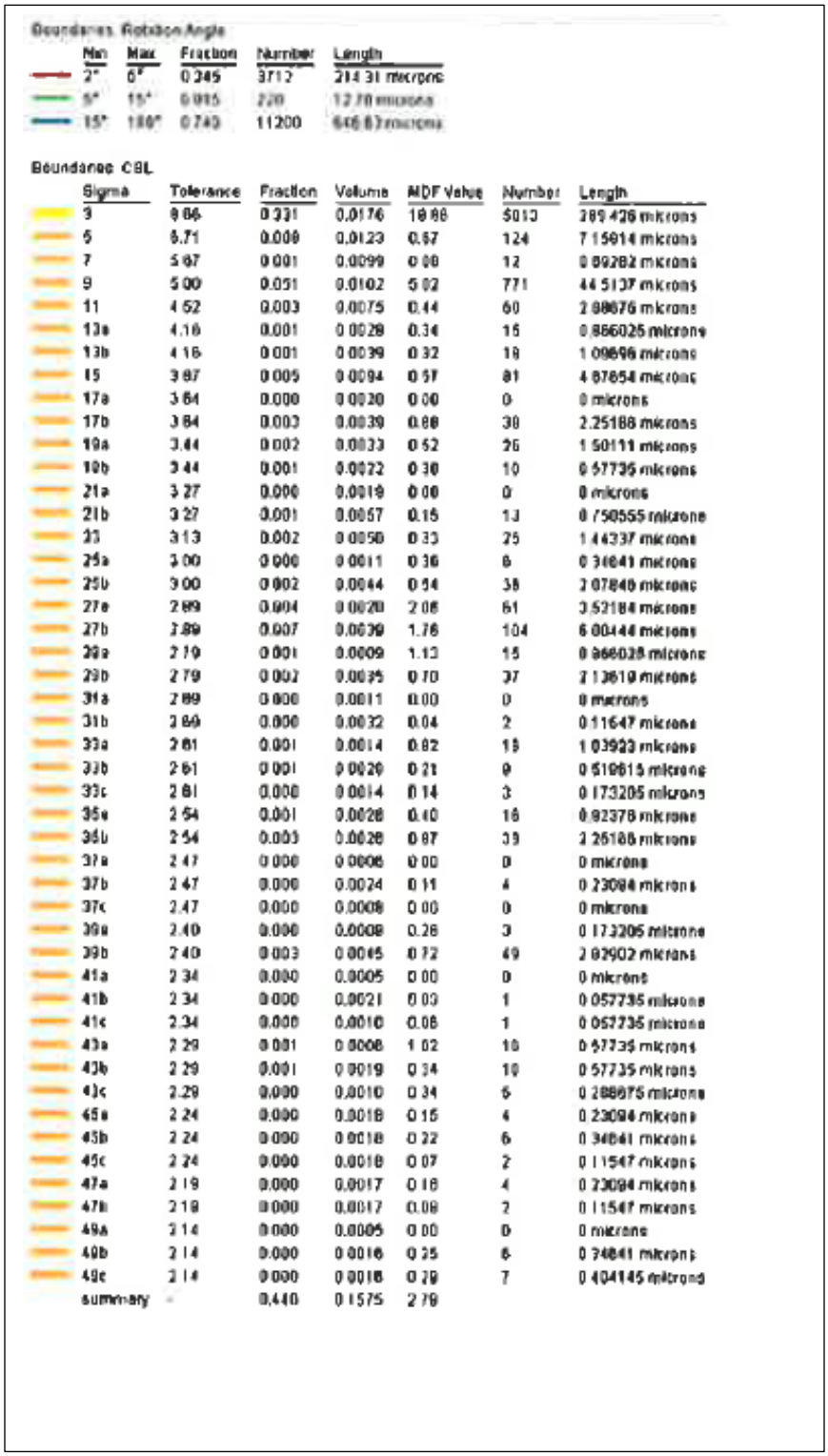

Boundaries Rotation Angle

	Min	Max	Fraction	Number	Length
	2°	5°	0.245	3712	214.31 microns
	5°	15°	0.015	220	12.78 microns
	15°	180°	0.740	11200	646.83 microns

Boundaries CSL

	Sigma	Tolerance	Fraction	Volume	MDF Value	Number	Length
	3	9.86	0.031	0.0176	10.88	5013	289.426 microns
	5	8.71	0.009	0.0123	0.67	124	7.15914 microns
	7	5.87	0.001	0.0099	0.00	12	0.692820 microns
	9	5.00	0.051	0.0102	5.02	771	44.5137 microns
	11	4.52	0.003	0.0075	0.44	60	2.98676 microns
	13a	4.16	0.001	0.0028	0.34	15	0.866025 microns
	13b	4.16	0.001	0.0039	0.32	18	1.09696 microns
	15	3.87	0.005	0.0094	0.57	81	4.67654 microns
	17a	3.64	0.000	0.0020	0.00	0	0 microns
	17b	3.64	0.003	0.0039	0.88	30	2.25188 microns
	19a	3.44	0.002	0.0033	0.52	26	1.50111 microns
	19b	3.44	0.001	0.0022	0.30	10	0.577350 microns
	21a	3.27	0.000	0.0019	0.00	0	0 microns
	21b	3.27	0.001	0.0057	0.15	13	0.750555 microns
	23	3.13	0.002	0.0050	0.33	25	1.44337 microns
	25a	3.00	0.000	0.0011	0.36	6	0.34641 microns
	25b	3.00	0.002	0.0044	0.54	38	2.07846 microns
	27a	2.89	0.004	0.0020	2.08	61	3.52184 microns
	27b	2.89	0.007	0.0039	1.76	104	6.00444 microns
	29a	2.79	0.001	0.0009	1.13	15	0.866025 microns
	29b	2.79	0.002	0.0035	0.70	37	2.13619 microns
	31a	2.89	0.000	0.0011	0.00	0	0 microns
	31b	2.89	0.000	0.0032	0.04	2	0.11547 microns
	33a	2.81	0.001	0.0014	0.82	15	1.03923 microns
	33b	2.81	0.001	0.0020	0.21	9	0.519615 microns
	33c	2.81	0.000	0.0014	0.14	3	0.173205 microns
	35a	2.54	0.001	0.0028	0.40	16	0.92378 microns
	35b	2.54	0.003	0.0028	0.87	39	2.25166 microns
	37a	2.47	0.000	0.0006	0.00	0	0 microns
	37b	2.47	0.000	0.0024	0.11	4	0.23094 microns
	37c	2.47	0.000	0.0008	0.00	0	0 microns
	39a	2.40	0.000	0.0009	0.26	3	0.173205 microns
	39b	2.40	0.003	0.0045	0.72	49	2.82902 microns
	41a	2.34	0.000	0.0005	0.00	0	0 microns
	41b	2.34	0.000	0.0021	0.03	1	0.057735 microns
	41c	2.34	0.000	0.0010	0.08	1	0.057735 microns
	43a	2.29	0.001	0.0008	1.02	10	0.577350 microns
	43b	2.29	0.001	0.0019	0.34	10	0.577350 microns
	43c	2.29	0.000	0.0010	0.34	5	0.288675 microns
	45a	2.24	0.000	0.0018	0.15	4	0.23094 microns
	45b	2.24	0.000	0.0018	0.22	6	0.34641 microns
	45c	2.24	0.000	0.0018	0.07	2	0.11547 microns
	47a	2.19	0.000	0.0017	0.16	4	0.23094 microns
	47b	2.19	0.000	0.0017	0.08	2	0.11547 microns
	49a	2.14	0.000	0.0005	0.00	0	0 microns
	49b	2.14	0.000	0.0016	0.25	6	0.34641 microns
	49c	2.14	0.000	0.0018	0.29	7	0.404145 microns
	summary		0.440	0.1575	2.79		

Appendix 6
6H-SiC OIM Data

Table 33. D-ref 6H-SiC Scan OIM Data Statistics

Dref_6Hphase_Aug092013

Operator: Support
Calibration: 0.540700 0.915000 0.684100
Working Distance: 10.000000

Number of points: 469128
Number of previously highlighted points 363381
Number of good points: 362494

Dimensions:
X Min: 0.00 microns
X Max: 44.40 microns
Y Min: 0.00 microns
Y Max: 22.82 microns
Step: 50.00 nm

Average Confidence Index: 0.08
Average Image Quality: 1480.87
Average Fit [degrees]: 1.21

Phases:
Silicon Carbide 6H

Name:New Partition
Formula:PCI[&]>0.100 AND PIQ[&]>500.0
Number of points in partition: 82986

Fraction of points in partition: 0.228
Number of indexed points: 82986

Average Confidence Index: 0.23
Average Image Quality: 1647.56
Average Fit [degrees]: 1.09

Phases:
Silicon Carbide 6H

Grain Size (Excluding Edge Grains):
Averages are number averages
Number of Grains: 9356
Number of Edge Grains: 0
Average Diameter: 0.11 (0.11) microns
Equivalent Area: 0.01 (0.01) square microns
Equivalent ASTM No.: 23.8 (23.8)

Table 34. D-ref 6H-SiC Scan Grain Size Chart

Chart: Grain Size (diameter)

Edge grains included in analysis

Diameter [microns]	Area Fraction
0.142074	0.520777
0.277719	0.120183
0.413364	0.0662992
0.549009	0.0532395
0.684654	0.0351255
0.8203	0.0280699
0.955945	0.0328189
1.09159	0.034057
1.22723	0.00831072
1.36288	0.0116859
1.49853	0.0416384
1.63417	0
1.76982	0
1.90546	0
2.04111	0
2.17675	0
2.3124	0
2.44804	0
2.58369	0
2.71933	0.0477951
Average	
Number	0.105384
Standard Deviation	0.0791651
Area	0.481734

Table 35. D2000 6H-SiC Scan OIM Data Statistics

D2000_6Hphase_Aug092013

Operator: Support
Calibration: 0.540700 0.915000 0.684100
Working Distance: 10.000000

Number of points: 397245
Number of previously highlighted points 326797
Number of good points: 326561

Dimensions:
X Min: 0.00 microns
X Max: 46.60 microns
Y Min: 0.00 microns
Y Max: 18.40 microns
Step: 50.00 nm

Average Confidence Index: 0.07
Average Image Quality: 642.07
Average Fit [degrees]: 1.52

Phases:
Silicon Carbide 6H

Name:New Partition
Formula:PIQ[&]>350.0 AND PCI[&]>0.100
Number of points in partition: 57115
Fraction of points in partition: 0.181
Number of indexed points: 57115

Average Confidence Index: 0.23
Average Image Quality: 749.78
Average Fit [degrees]: 1.32

Phases:
Silicon Carbide 6H

Grain Size (Excluding Edge Grains):
Averages are number averages
Number of Grains: 6705
Number of Edge Grains: 58
Average Diameter: 0.09 (0.09) microns
  Equivalent Area: 0.01 (0.01) square microns
  Equivalent ASTM No.: 24.3 (24.3)

Table 36. D2000 6H-SiC Grain Size Data

Chart: Grain Size (diameter)

Edge grains included in analysis

Diameter [microns]	Area Fraction
0.140549	0.640013
0.273144	0.105986
0.405739	0.0656267
0.538334	0.0297983
0.670929	0.0255818
0.803525	0.024726
0.93612	0.0198283
1.06871	0.017347
1.20131	0.0109534
1.3339	0.00483389
1.4665	0.00535082
1.5991	0.0132188
1.73169	0
1.86429	0
1.99689	0
2.12948	0
2.26207	0
2.39467	0
2.52726	0.0172879
2.65986	0.0193895
Average	
Number	0.0984156
Standard Deviation	0.0514023
Area	0.357716

Table 37. E-ref 6H-SiC Scan Data Statistics

Eref_Aug16_2013

Operator: Support
Calibration: 0.540700 0.915000 0.684100
Working Distance: 10.000000

Number of points: 163702
Number of good points: 126147

Dimensions:
X Min: 0.00 microns
X Max: 39.83 microns
Y Min: 0.00 microns
Y Max: 19.94 microns
Step: 75.00 nm

Average Confidence Index: 0.08
Average Image Quality: 796.07
Average Fit [degrees]: 1.47
Minimum boundary misorientation: 2.0 degrees (see Settings>Preferences)
Number of boundary segments: 307015
Length of boundary segments: 1.32941 cm

Phases:
Silicon Carbide 6H

Name:New Partition
Formula:PIQ[&]>350.0 AND PCI[&]>0.100
Number of points in partition: 17893
Fraction of points in partition: 0.241
Number of indexed points: 17893

Average Confidence Index: 0.23
Average Image Quality: 1065.04
Average Fit [degrees]: 1.21

Phases:
Silicon Carbide 6H

Grain Size (Excluding Edge Grains):
Averages are number averages
Number of Grains: 2334
Number of Edge Grains: 49
Average Diameter: 0.14 (0.14) microns
Equivalent Area: 0.02 (0.02) square microns
Equivalent ASTM No.: 23.0 (23.0)

Table 38. E-ref 6H-SiC Scan Grain Boundary Data

Chart: Grain Size (diameter)

Edge grains included in analysis

Diameter [microns]	Area Fraction
0.151095	0.553182
0.230532	0.151406
0.309968	0.0699937
0.389404	0.0519137
0.46884	0.030239
0.548276	0.0301332
0.627712	0.0134278
0.707149	0
0.786585	0.0105731
0.866021	0.0124762
0.945457	0
1.02489	0
1.10433	0
1.18377	0
1.2632	0.0273842
1.34264	0
1.42207	0
1.50151	0
1.58095	0
1.66038	0.0492705
Average	
Number	0.14182
Standard Deviation	0.0708765
Area	0.322634